2023-04-19

A Large-Scale Survey of Brown Dwarf Atmospheres

Savanah Kay Turner
Brigham Young University

A Large-Scale Survey of Brown Dwarf Atmospheres

Savanah Kay Turner

A thesis submitted to the faculty of
Brigham Young University
in partial fulfillment of the requirements for the degree of

Master of Science

Denise Stephens, Chair
Benjamin Boizelle
Eric Hintz

Department of Physics and Astronomy

Brigham Young University

ABSTRACT

A Large-Scale Survey of Brown Dwarf Atmospheres

Savanah Kay Turner
Department of Physics and Astronomy, BYU
Master of Science

Brown dwarfs are substellar objects that fall in-between the smallest stars and largest planets in size and temperature. Due to their relatively cool temperatures, the atmospheres of these “failed stars” have been shown to exhibit interesting properties such as iron, silicate, and salt clouds. Theoretical atmospheric models based on known physics and chemistry can be used as tools to interpret and understand our observations of brown dwarfs. I have fit archival and new infrared spectra of over 300 brown dwarfs with atmospheric models. Using the parameters of the best-fit models as estimates for the physical properties of the brown dwarfs in my sample, I have performed a survey of how brown dwarfs evolve with spectral type and temperature. I present my fit results and observed trends. I use these fit results to note where current atmospheric models are able to well-replicate the data and where the models and data conflict.

Keywords: brown dwarfs, atmospheric models, low-mass stars, exoplanet atmospheres, infrared spectroscopy

ACKNOWLEDGMENTS

I thank my advisor, Denise Stephens, for the many hours she has spent mentoring me over the past three years. She has gone above and beyond the expectations of a research advisor in every way and become someone that I will look up to for the rest of my life. I look forward to continuing to learn from her as I begin my PHD work under her tutelage.

I thank Conner Scoresby for remaining calm all those times when TSPEC crashed and Candace started screaming, for entertaining us with lessons on sports statistics during cloudy half-nights, and for the many hours he spent reducing spectral data.

Lastly, I thank my family. Many thanks to my parents for encouraging me to chase my dreams. Thanks to our unborn baby for being along for the ride this year, for kicking me awake during class and late-night research sessions, and for waiting until after my thesis defense to make an appearance. Dad and I can't wait to meet you in a few weeks. Most of all, I thank my sweet husband Austin for being my rock, my best friend, and the love of my life (and for always being willing to make a late-night ice cream run).

TABLE OF CONTENTS

LIST OF FIGURES

LIST OF TABLES

Chapter 1

Introduction

Brown dwarf research is a relatively young area of astronomy due to the cool temperatures and dim luminosities of these substellar objects. The difficulty of observing such faint objects through a telescope meant that brown dwarfs were predicted theoretically decades before the first observational discoveries. In the years that have followed since those initial discoveries, many individuals have contributed to the efforts to better characterize and understand these substellar bodies.

In this section, I first outline some of the key events of the history of brown dwarf research. Next, I provide a brief summary of the general characteristics of brown dwarfs. I then explain how brown dwarfs can be useful as exoplanet analogs and, by extension, how brown dwarf research is furthering the goals of the NASA Astrophysics Division. Finally, I give an overview of the goals of this project and structure of the paper as a whole.

1.1 History of Brown Dwarf Research

Every introductory astronomy course teaches that stars are formed when a giant molecular cloud collapses in on itself. The cloud fragments into multiple centers of collapse of various masses, each of which will become a new stellar object. Each protostar continues to gravitationally contract, converting the original gravitational potential energy of the material into thermal energy, until its core reaches great enough temperatures and pressures for hydrogen

fusion to ignite. This fusion pushes back against the inward gravitational pressure and halts the collapse of the star.

In 1963, an astrophysicist named Shiv Kumar [1] analyzed convective models of stars of mass $M < 0.1\ M_{\odot}$[1]. Kumar found that there was a point during the formation of these low-mass objects at which further contraction resulted in a *decrease* in temperature rather than the generally expected increase. This drop in temperature was due to the input energy needed to overcome electron degeneracy pressure. He calculated that, eventually, electron degeneracy pressure would halt the gravitational collapse of these small objects without their ever reaching the temperatures and pressures needed to ignite hydrogen fusion. Kumar explained: [1]

Thus all stars having a mass less than a certain limiting mass ultimately become completely degenerate objects or "black" dwarfs without ever going through the normal stellar evolution.

Kumar is credited with the first prediction of the existence of what he dubbed "black dwarfs." Twelve years later, the name for these objects was changed to "brown dwarfs" by Jill Tarter to avoid confusion with perpetually-cooling white dwarf remnants, also called "black dwarfs" [2].

It wasn't until 1995 that the first brown dwarf candidates were observed. Two different teams published papers that same year announcing their independent brown dwarf discoveries.

The team led by R. Rebolo published their paper in September 1995, entitled *Discovery of a Brown Dwarf in the Pleiades Star Cluster* [3]. Pleiades, a nearby open cluster, was chosen as the best site to search for the first brown dwarf due to its young age: brown dwarfs that formed within this cluster would be more likely to be young and warm enough to still be detectable in

[1] This symbol means "solar mass".

the near infrared. The discovery of their brown dwarf, Teide 1, occurred after they had surveyed only 0.3% of the area of the Pleiades cluster, leading them to conclude that the cluster could likely house somewhere around 175 brown dwarfs in total.

They first detected the object in photometric data, and then performed follow-up optical spectroscopy. The similarities between the optical spectrum of Teide 1 and LHS 2065, a known M9 dwarf, were immediately apparent and showed that Teide 1 was indeed a cool dwarf of some type (Figure 1). Using the bolometric luminosity of Teide 1 and estimates for the luminosity-mass relationship of cool stars, the team estimated the mass of their brown dwarf candidate to be less than 70 times the mass of Jupiter, right in the predicted range of brown dwarf masses.

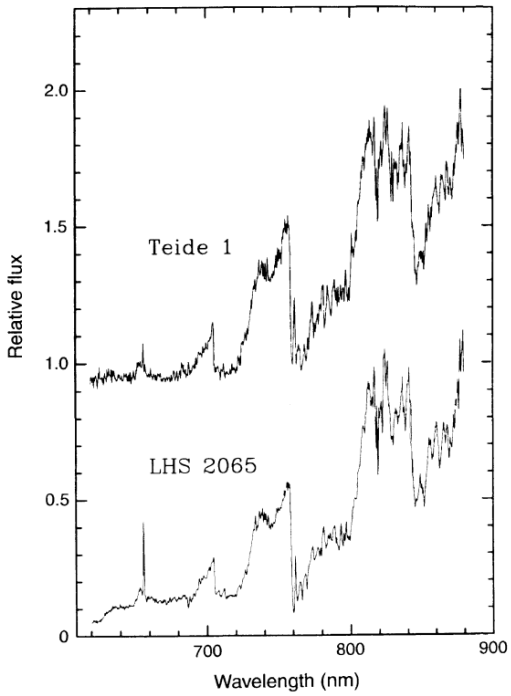

Figure 1: Taken from Figure 1 of Rebolo et al. [3]. A comparison of the optical spectrum of brown dwarf Teide 1 to that of the M9 star LHS 2065. The similarities between the spectra showed that Teide 1 was a cool, low-mass object. It wasn't until the discovery of lithium in the atmosphere of Teide 1 [4] that it was accepted as the first brown dwarf discovery.

The final step was to look for lithium in the spectrum of the object. Lithium is depleted in low mass stars due to convective mixing and lithium burning, but was expected to still be abundant in brown dwarf atmospheres because all but the largest of these objects lack the mass needed to burn lithium[2]. Follow-up observations using the low-resolution imaging spectrograph on the Keck Observatory 10-meter telescope discovered lithium in the atmosphere of Teide 1 (Figure 2), confirming its status as a brown dwarf [4].

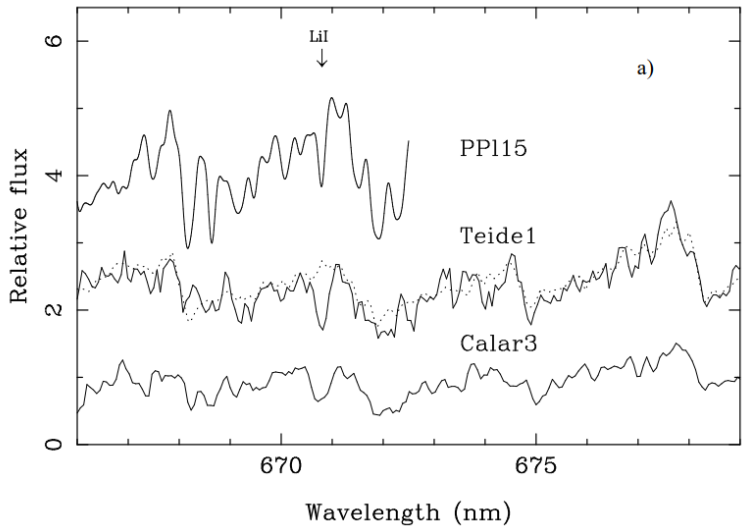

Figure 2: Taken from Figure 2a of Rebolo et al. [4]. The spectrum of Teide 1 is compared to the spectra of Calar 3 (another brown dwarf candidate [5]) and PPl 15 (a known brown dwarf [6]). The lithium 1 feature at 670.8 nm is visible in all three spectra, confirming that all three objects are brown dwarfs.

Two months after the Rebolo 1995 paper, Nakajima et al. [7] observed a companion object orbiting the M-type red dwarf star Gl229. Broadband spectroscopy in the optical and infrared (Figure 3) allowed the team to calculate a bolometric luminosity for the companion object, which was found to be orders of magnitude fainter than the luminosity of the dimmest

[2] Brown dwarfs with masses of about 60-75 times the mass of Jupiter are able to fuse lithium at the beginning of their lives. Brown dwarfs with masses less than 60 times that of Jupiter never have this ability, however. Thus, discovering lithium in the atmosphere of a substellar object can confirm that it is a brown dwarf if the object is old enough to have burned all of its lithium, but the lack of lithium does not necessarily mean that it is *not* a brown dwarf. [26]

known star. Furthermore, the broadband spectrum of the companion peaked in the infrared J-filter, suggesting the presence of strong H_2O and CH_4 absorption. These absorption features matched the theoretical brown dwarf models of the time. They named this companion Gl229B and declared with confidence that "Gl229B is certainly a brown dwarf."

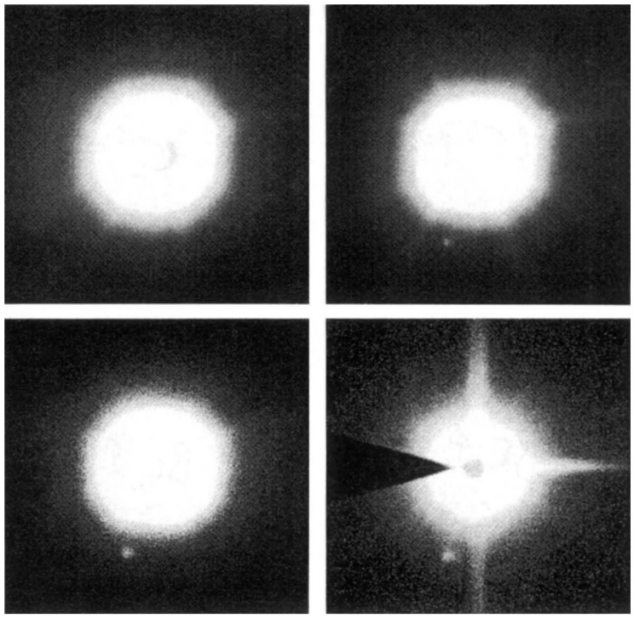

Figure 3: Taken from Figure 1 of Nakajima et al. [7]. Photometry of the M-type red dwarf star Gl229 and brown dwarf companion Gl229B. Images were taken in r-band (top left), i-band (top right), z-band (bottom left), and ks-band (bottom right) using the Palomar 60-inch telescope (r-, i-, and z-band images) and the Hale 200-inch telescope (ks-band image).

These first two discoveries were just the beginning. By the end of 1998, 26 brown dwarfs had been discovered. Kirkpatrick et al. [8] began the process of classifying these objects into spectral types, defining the "L" spectral type and suggesting the future need for a cooler spectral type, "T."

The onset of near-infrared all-sky surveys resulted in a rapid increase of brown dwarf discoveries. By early 2001, the number of known brown dwarfs was approaching 100. Many of these and future discoveries were due to the Two Micron All Sky Survey (2MASS [9]), Deep

Near-Infrared Survey (DENIS [10]), and Sloan Digital Sky Survey (SDSS [11]). Burgasser et al. [12] analyzed these new data and outlined an official definition of the spectral type "T" in 2001.

Brown dwarf discoveries continued and ten years later, data provided by the Wide-Field Infrared Survey Explorer (WISE [13]) revealed the existence of brown dwarfs even cooler than Burgasser's T dwarfs. Cushing et al. [14] published a paper defining spectral type "Y" in 2011. This remains the coolest brown dwarf spectral type that has been observed and defined to date.

As of 2015, there had been nearly 3000 confirmed brown dwarf discoveries [15], and that number continues to grow. Brown dwarf research remains an active area of study as we seek to understand how these objects form, how they evolve over time, what molecules can be found in their atmospheres, how many exist in our galaxy, and more. Looking forward, the era of the James Webb Space Telescope (JWST) promises to bring exciting new discoveries that will shape the future of brown dwarf research.

1.2 General Characteristics of Brown Dwarfs

Smaller than the smallest stars but more massive than the largest planets, brown dwarfs exhibit characteristics of both stellar and planetary bodies.

One nickname often given to brown dwarfs is "failed stars" [16]. When a molecular cloud is perturbed and begins to collapse, it will fragment into pieces. The initial mass of each fragment determines the type of star that it will become: the largest fragments will form the hottest, largest, brightest stars while smaller fragments form cooler, smaller, dimmer stars. Even smaller fragments, below a mass of about 80 times the mass of Jupiter [17], will fail to achieve the temperatures and pressures needed to ignite hydrogen fusion, and thus will produce brown dwarfs rather than stars. Many brown dwarfs do have masses above the deuterium fusion limit and thus are initially able to burn deuterium [18], but they quickly run out of fuel and fizzle out.

Because brown dwarfs form like stars but are unable to maintain fusion in their cores, they indeed could be considered the "failures" of the stellar class.

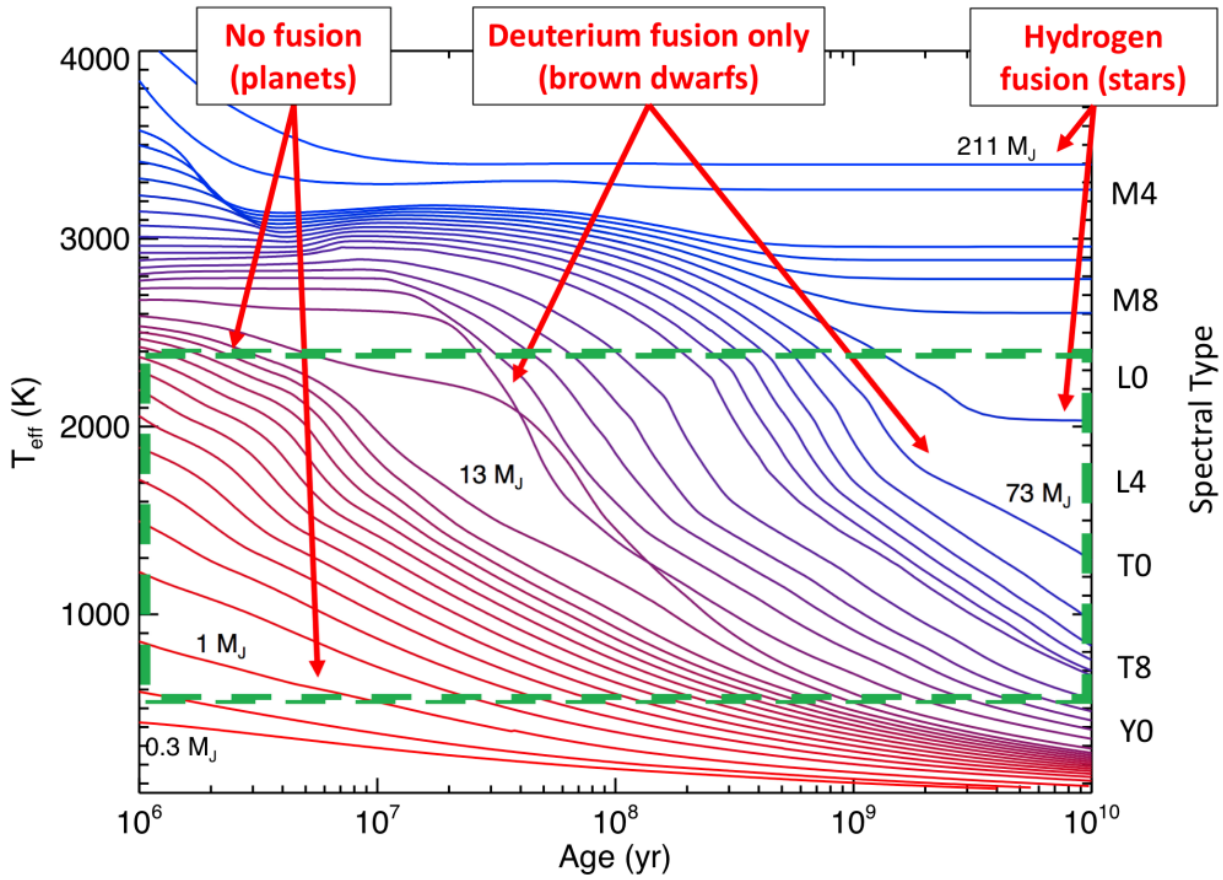

Figure 4: Taken from Figure 1 of Muirhead et al. [21], who adapted a plot from Burrows et al [22]. This plot shows evolutionary curves of objects of different initial masses. Planetary, stellar, and brown-dwarf regimes are labeled.

On the other hand, some prefer to think of brown dwarfs as "super Jupiters" [16] due to the characteristics they share with large planets. For one thing, the smallest deuterium-fusing brown dwarfs are only about 13 times the mass of Jupiter [18], and sub-brown dwarfs [3]are expected to be able to form with initial masses as small as 1 Jupiter mass [27]. All brown dwarfs,

[3] The nomenclature for objects that form like stars but are below the deuterium fusion limit is a source of debate. One common name for these cool objects is "sub-brown dwarfs," although many astronomers including Shiv Kumar [27] believe that all objects below the hydrogen fusion limit that form like stars should simply be called "brown dwarfs."

regardless of mass, are expected to have about the same radius as Jupiter [19]. There is also a large overlap in the temperatures of brown dwarfs and large planets, resulting in a similar atmospheric makeup [20].

Furthermore, while stars are able to maintain a fairly constant temperature for the majority of their lifetimes due to the energy generated during the fusion process, both brown dwarfs—after a possible initial period of deuterium burning—and planets lack this internal furnace. Brown dwarfs and planets thus must cool over time as they lose energy via blackbody radiation. The thermal evolution of brown dwarfs compared to planets and very low-mass stars is depicted in Figure 4. Each curve in the figure represents the evolutionary track of an object with a different initial mass. Note that the initial mass determines the starting effective temperature and spectral type of the object, and that a brown dwarf will evolve through later and later spectral types as it cools.

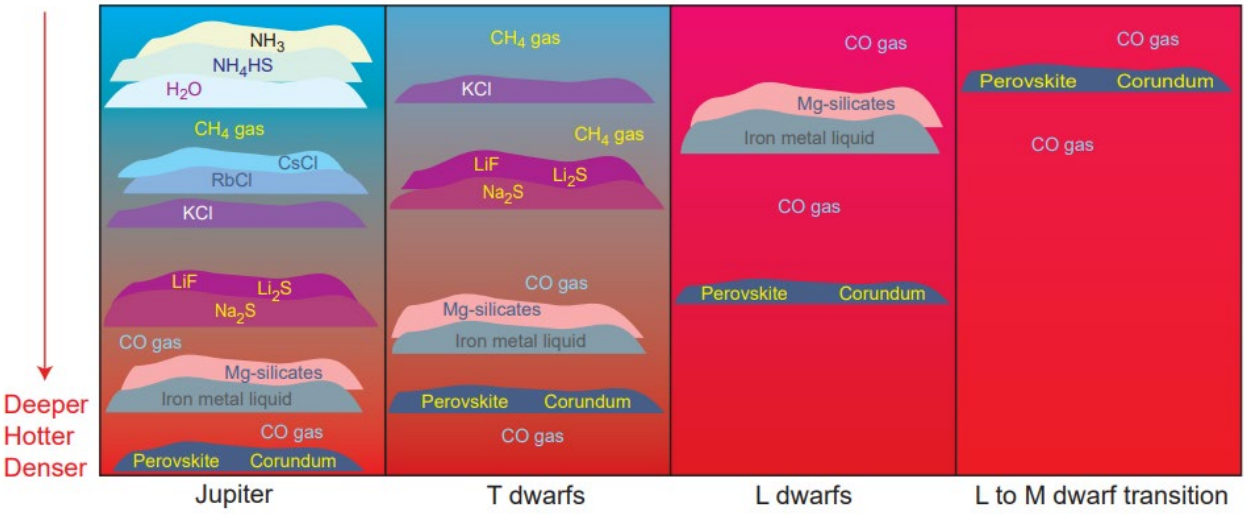

Figure 5: Taken from Lodders [25]. A diagram showing different cloud layers that are expected to exist in L and T brown dwarfs compared to the cloud layers in Jupiter and objects on the brown dwarf-stellar boundary (L to M dwarf transition).

Brown dwarfs have also been observed to exhibit complex cloud structures like those seen in planetary atmospheres. Molecules, dust grains, and clouds that would be unstable in the

much hotter atmospheres of stars appear to be prevalent in brown dwarfs. Because the temperature and pressure of a brown dwarf atmosphere increases with depth, different cloud species are stable at different altitudes, resulting in cloud layers similar to those observed in the planet Jupiter (Figure 5). The number and composition of these cloud layers depends on the effective temperature/spectral type of the brown dwarf. Specifics regarding the chemistry of brown dwarf atmospheres will be further explored in Chapter 2.

1.3 Brown Dwarfs as Analogs of Exoplanets

I have thus far presented a brief overview of the history of brown dwarf research, as well as a small glimpse into the general characteristics of these substellar objects. While many might see the search for understanding alone as a goal worthy of any effort, I acknowledge that, more often than not, the general public prefers an answer to the question "so, why should we care?" Thus, before proceeding to the more technical parts of this thesis, I pause to address this often-expensive question.

The characterization of exoplanets and the search for Earth-like planets has recently become a major focus of astrophysics. Indeed, the search for habitable worlds around other stars is listed as one of the three main goals of the NASA Astrophysics Division [23].

However, there are many challenges when it comes to exoplanet characterization. One major complication is the dimness of exoplanets compared to their host stars. The difficulty of observing an exoplanet has been compared to "looking for a firefly with a spotlight shining in your face" [24]. Creative observational techniques are in use and more are under development, but the fact remains that direct exoplanet observation can be a chore.

Brown dwarfs, on the other hand, are often found in single systems far from brighter stars. Their cool temperatures and cloudy atmospheres make brown dwarfs effective analogs for

exoplanets. In fact, many of the same research groups that develop atmospheric models for brown dwarfs also develop models for large exoplanets because of the overlap in temperatures [20].

As brown dwarf researchers work to refine understanding of the characteristics and evolution of brown dwarf atmospheres, our results can be used to further the efforts of exoplanet characterization. As brown dwarf and exoplanet atmosphere modeling techniques improve together, the quest to answer the question "could other planets harbor life?" becomes less a topic of science fiction and more an attainable goal of science.

1.4 Project Overview

The main goal of this project was to fit a large sample of archival and new brown dwarf spectra to atmospheric models. The purpose of this model fitting is two-fold:

First, the parameters of the best-fit models (described in detail in Chapter 4) can be used to estimate the physical properties of the brown dwarfs. I know of no other project where physical properties such as temperature, cloudiness, cloud composition, etc. have been estimated for such a large sample of brown dwarfs. Analysis of these physical properties across the brown dwarf evolutionary sequence has provided insight into how brown dwarf atmospheres change as they cool. The model-fitting results also allow for a discussion of the correlation between pairs of attributes such as temperature and spectral type, optical and infrared type, cloudiness and temperature, etc.

Second, fitting such an extensive sample of brown dwarfs with atmospheric models highlights where the models and data match well and where the models need to be adjusted. Atmospheric modeling is an ongoing, iterative process. It is necessary to carry out projects such

as this in order to reveal physics and chemistry that might be missing from current models so that modeling techniques can continue to improve.

Chapters 2-4 of this paper provide necessary background regarding infrared astronomy, brown dwarf spectral types, and theoretical models. Chapter 5 describes the code used for the spectral fitting, and Chapter 6 explains where the data were obtained. In Chapters 7 and 8, I give analysis of the fits and observed trends. Conclusions and ideas for future work are described in Chapter 9.

Chapter 2

Infrared Astronomy: Observational Terms

2.1 Magnitudes

When observing objects through a telescope, one of the main properties one might wish to quantify is the brightness of the object. Historically, ancient astronomers such as Hipparchus assigned brightness measures to stars by eye. These measures were called "magnitudes," and smaller magnitudes corresponded to brighter objects. Because the human eye perceives brightness on a logarithmic scale rather than a linear scale, Hipparchus' original magnitude scale was similarly non-linear [28].

As technology has developed, methods for quantifying brightness have become more clearly defined and consistent than the original by-eye measurements. However, the logarithmic magnitude system has remained because astronomers love tradition nearly as much as we love horrible acronyms[4].

Various magnitude systems have been developed over the years with different zero-points. The system used in this paper is the Vega system, where a magnitude of zero corresponds to the observed magnitude of Vega, the brightest star in the summer constellation Lyra. Negative

[4] I refer readers to the following website for a demonstration of just how much astronomers love our horrible acronyms: https://lweb.cfa.harvard.edu/~gpetitpas/Links/Astroacro.html.

magnitudes correspond to objects that are brighter than Vega, while objects with positive magnitudes are fainter.

The magnitude that is measured from a telescope is called an "apparent magnitude." However, flux—the amount of light passing through a square area per unit time—falls off with distance squared. This means that comparing apparent magnitudes of objects that are different distances from earth is not truly a method of comparing the intrinsic brightness of the objects.

In order to calculate the true or "absolute magnitude" of an object, one must know its distance from Earth. Then, the distance modulus equation given in Equation 1 can be used to convert from apparent to absolute magnitude. In this equation, M and m are absolute and apparent magnitudes, respectively, and d is the distance to the object in parsecs.

$$\boldsymbol{M = m - 5\log_{10}\left(\frac{d}{10}\right)} \qquad \textbf{Equation 1}$$

2.2 Filters and Colors

In Hipparchus' day, magnitudes were based on the wavelengths of light that were visible to the human eye. Today, magnitudes are measured in different passbands of light. Filters with different transmission profiles are used to limit the range of wavelengths that are able to reach the detector of the telescope, and then a magnitude can be calculated for that passband/filter.

Comparing the magnitudes of an object measured in different filters can provide insight into the physical properties of that object. For example, an object that is brighter in an ultraviolet filter than in a green optical filter is likely a young, hot star with a blackbody peak in the ultraviolet. On the other hand, cooler stars like our Sun would be brighter in the green filter than in the ultraviolet filter because the Sun's blackbody curve peaks in the optical part of the spectrum.

"Colors" of objects are calculated by subtracting magnitudes in two different filters. One of the most common colors used in infrared astronomy is the J-K color. The J filter is centered around 1.2 μm while the K filter is centered at 2.1 μm. Even though both filter magnitudes measure infrared light, the J filter measures shorter, more energetic infrared wavelengths and is therefore considered to be a "bluer" filter than the "redder" K filter. Thus, brown dwarfs with negative J-K colors are called "blue" brown dwarfs while brown dwarfs with larger, positive J-K colors are called "red" brown dwarfs (recall that smaller magnitudes are brighter, so a negative J-K color means that the object is brighter in the J filter). The J-K color is especially useful for estimating the cloudiness of a brown dwarf atmosphere. This will be discussed more in later chapters.

2.3 Atmospheric Absorption

One factor that needs to be taken into consideration when performing observational astronomy from the ground is the effect of the Earth's atmosphere on the light that we observe. Molecules in the atmosphere absorb and scatter light before it reaches our telescopes. These effects are dependent upon the wavelength of light, so failing to take them into account can drastically impact our observations.

As seen in Figure 6, the visible part of the spectrum is mostly free of atmospheric absorbers. Rayleigh scattering is important here, but can easily be accounted for because the amount of scattering versus wavelength is well-defined.

In the infrared, the effects of the atmosphere become far more important. The near-infrared (from about 0.7 – 2.5 μm) is dominated by absorption from water vapor, carbon dioxide, and methane. Not only do these molecules absorb large wavelength regions or "bands" of light, but their effects are constantly fluctuating: the amount of water vapor absorption in particular

depends on weather, location, humidity, and altitude and can change quickly over the course of a night.

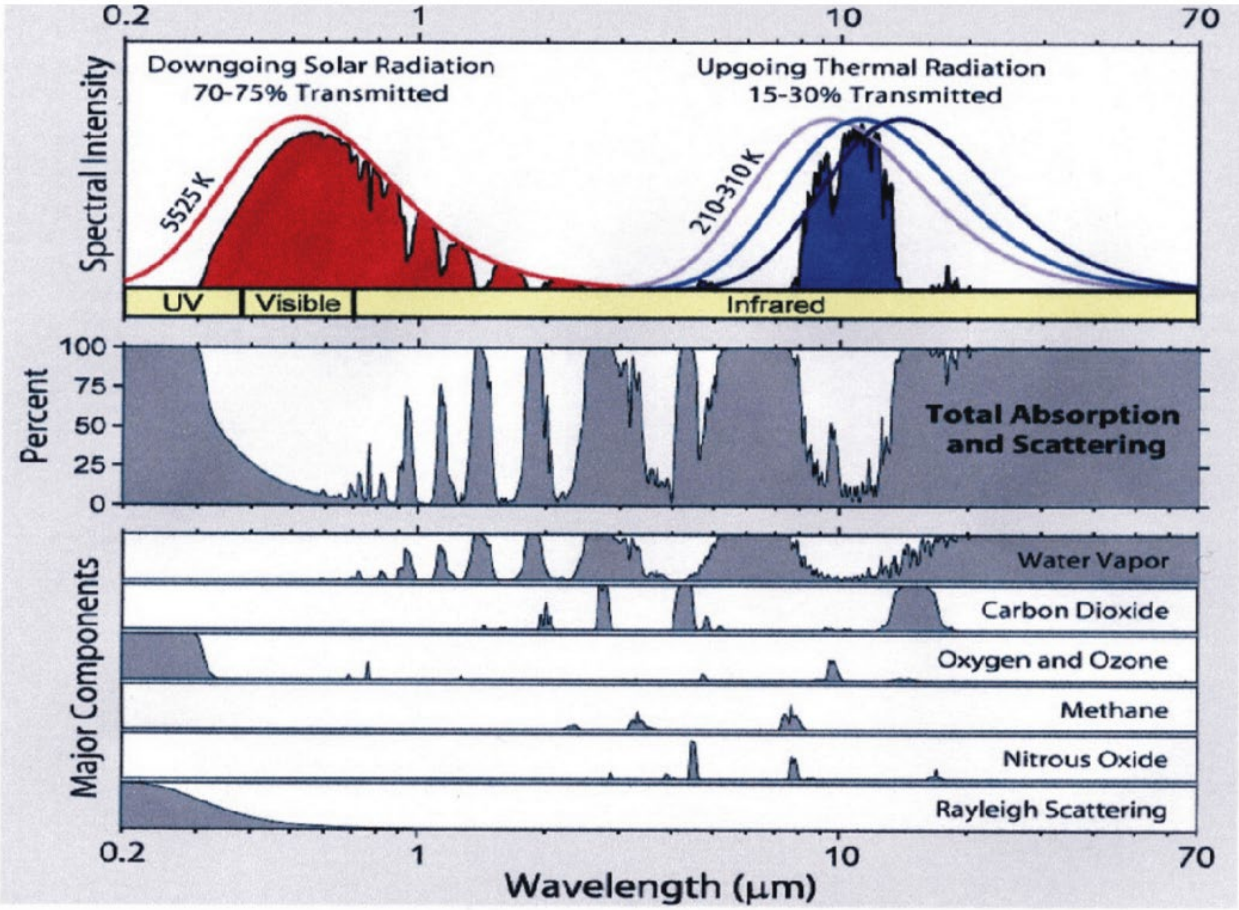

Figure 6: Taken from Figure 7 of Alimonti [29]. The top diagram shows the transmission spectrum of solar radiation (red) and thermal/infrared radiation (blue) through the atmosphere of the earth. The second panel gives the percent of light that is absorbed/scattered at each wavelength. The bottom panels show how components such as water vapor, other atmospheric molecules, and Rayleigh scattering contribute to this removal of light at each wavelength.

Near-infrared filters are carefully designed to fit in wavelength regimes that fall in-between major bands of atmospheric absorption. The three main infrared filters are J, H, and K. Various filter systems use slightly different versions of these three filters. The filter systems discussed in this paper are the 2MASS and MKO systems. Transmission profiles for some common filter systems, including 2MASS and MKO, are given in Figure 7. Because the filters of

different profiles are not identical, magnitudes obtained for the same object using different filter systems will not be identical and should be compared with caution [30].

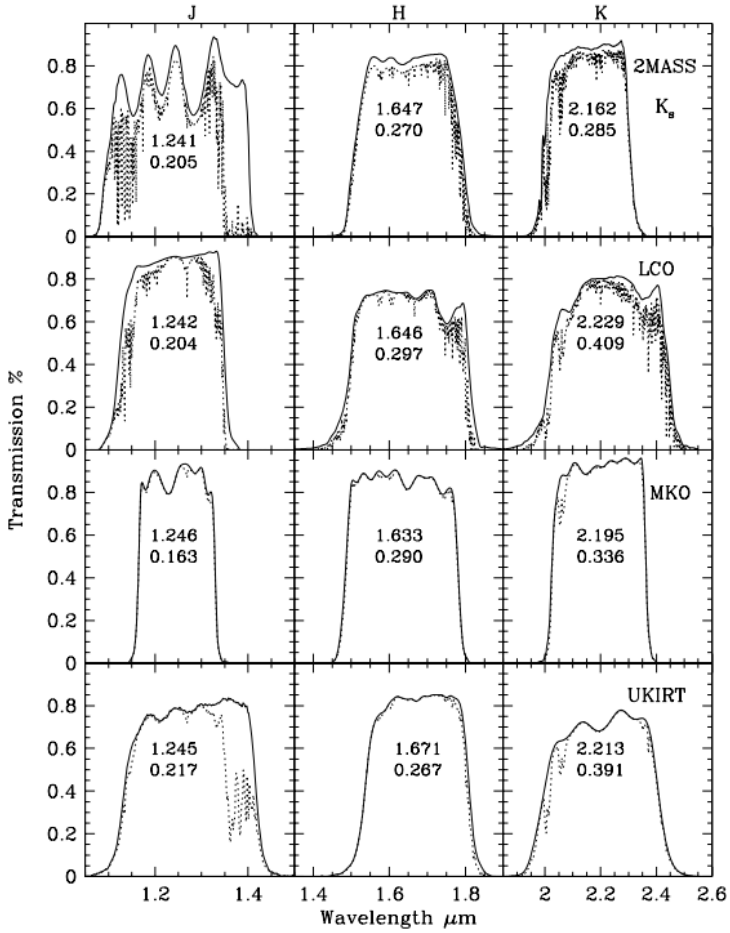

Figure 7: Taken from Figure 1 of Leggett et al. [30]. Transmission profiles of J, H, and K filters from various filter systems. This project mainly uses 2MASS magnitudes, but a small discussion of MKO magnitudes is included in the analysis of Best's gap later in this paper. The different transmission profiles mean that measured magnitudes and colors are system-dependent.

Nearly all light in the mid-infrared (from about 2.5-15 μm) is absorbed by atmospheric water vapor before it reaches ground-based telescopes. Thus, observations in the mid-infrared require time on space telescopes such as the James Webb Space Telescope. Previous missions such as the Spitzer Space Telescope and the Japanese observatory AKARI had mid-infrared

detectors, but neither mission is operational today. The archival data used in this project was all obtained from the ground, and therefore only covers wavelengths in the near-infrared.

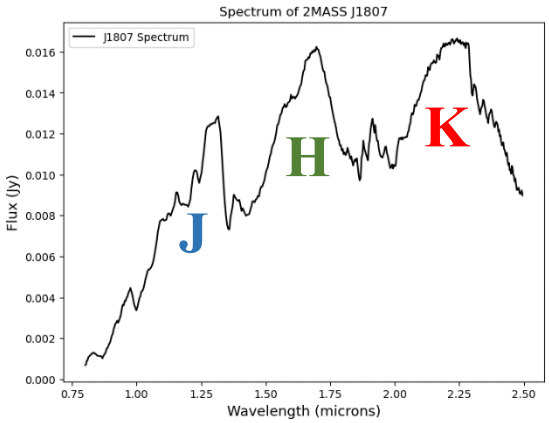

Figure 8: Spectrum of the L1-type brown dwarf 2MASS J1807159+501531. The spectral data was published by Burgasser et al. [31] and obtained from the SpeX Prism Library [32]. J, H, and K bands have been labeled.

Passband filters are not used in spectroscopy. However, it is common practice in brown dwarf astronomy to refer to regions of the spectrum of a brown dwarf by the name of the near-infrared filter in which they would fall. For example, the three regions of the brown dwarf spectrum given in Figure 8 have been labeled with their corresponding filter bands. Note the significant absorption features in the spectrum of the brown dwarf in-between the three bands. These are caused by absorption of light by the atmosphere of the Earth, not by the brown dwarf.

Chapter 3

Brown Dwarf Spectral Types

Spectroscopy is one of the most powerful methods of studying the atmospheres of objects in space. The spectral signature of an object can reveal much about its chemical makeup, temperature, variability, density, etc. Thus, it has long been a tradition in astronomy to classify stars and substellar objects such as brown dwarfs based on similarities in their spectral features.

The three spectral classes used for brown dwarfs are the L, T, and Y types. Each letter is further subdivided into numerical types—given in integer or sometimes half-integer steps—ranging from 0 to 9.5. These spectral classifications roughly correlate to a temperature sequence, where L0 is the hottest spectral type and Y9.5 is the coolest type (although no objects of class Y9.5 have been observed to date).

Occasionally, numerical indices are used to denote the different spectral types for ease of plotting or data analysis. In index notation, the letter is replaced by a 1 (for L-dwarfs), 2 (for T-dwarfs), or 3 (for Y-dwarfs), while the numerical subtype remains the same. For example, the spectral index for an L5 dwarf is 15, while the index for a T3 dwarf is 23.

As it cools, a brown dwarf will evolve through progressively cooler spectral types. For this reason, the hotter spectral types are often referred to as “early types,” while the cooler types are sometimes called “late types.”

With changes in temperature/spectral type come changes in cloud properties and atmospheric chemistry as molecules condense, settle, and mix through different layers of the atmosphere. In this chapter, I outline the main characteristics of each brown dwarf spectral type as well as some of the complexities that arise as a brown dwarf transitions from type L to type T.

3.1 L Type

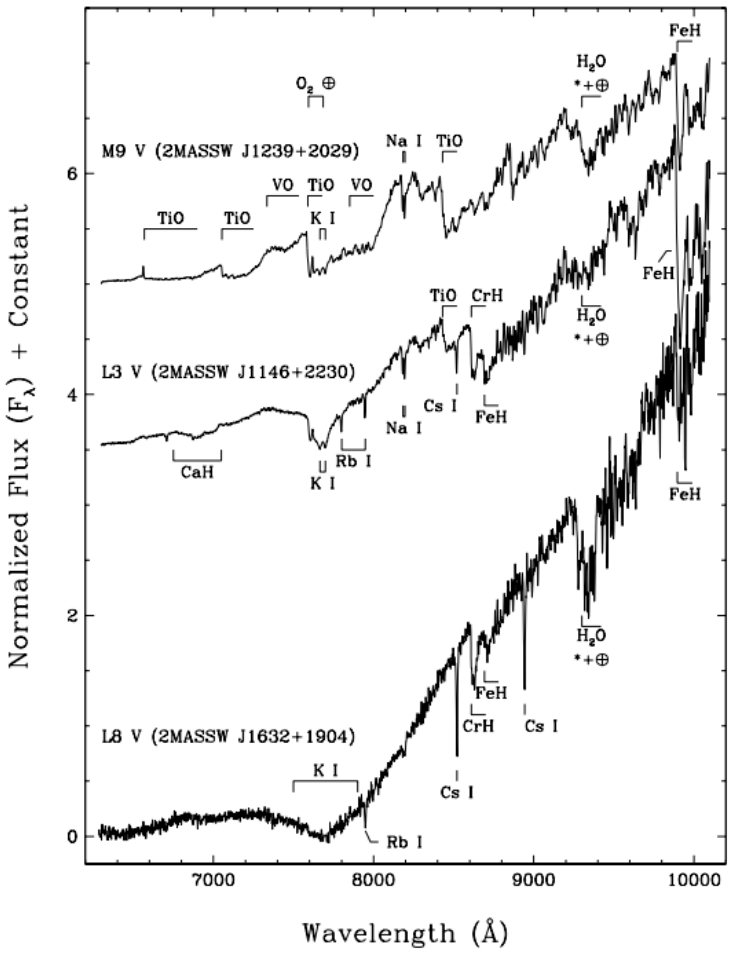

Figure 9: Taken from Figure 4 of Kirkpatrick et al. [8]. Comparison of the spectra of a late-M star, an early-L brown dwarf, and a late-L brown dwarf. The main spectroscopic marker of the L- type versus the M- type is the disappearance of TiO and VO lines and the strengthening of hydride and alkali features. Absorption features denoting the presence of various atoms and molecules have been labeled.

The L-type was classified by Kirkpatrick et al. [8] and denotes the hottest class of brown dwarfs. The general consensus is that L-type brown dwarfs range in temperature from about 2400 K (type L0) down to about 1300 K (type L9.5) [33]. Spectroscopically, L-type brown dwarfs are differentiated from the coolest stars (spectral type M, also called "red dwarfs") by the disappearance of TiO and VO spectral features. Instead of these metal oxides, L-dwarf spectra in the far optical are dominated by metallic hydrides and neutral alkali metals. A comparison of M- and L- type spectra is given in Figure 9.

L-DWARF FEATURE IDENTIFICATIONS IN THE FAR-OPTICAL

Atom/ Molecule (1)	Location (Å) (2)	Transition (3)
Hα[a]	6563	$3d\ ^2D_{5/2}-2p\ ^2P_{3/2}$
Li I[a].....	6708	$2s\ ^2S_{1/2}-2p\ ^2P_{3/2,1/2}$
CaH[a,b]...	Broad trough ~6750–7050	0–0 band of $A\ ^2\Pi–X\ ^2\Sigma$
TiO[a]	7053 head, degraded to red	0–0 band of $A\ ^3\Phi–X\ ^3\Delta$
VO[a].....	Broad trough ~7334–7534	1–0 band of $B\ ^4\Pi–X\ ^4\Sigma^-$
TiO[a]	7589 head, degraded to red	0–1 band of $A\ ^3\Phi–X\ ^3\Delta$
K I[b].....	7665	$4s\ ^2S_{1/2}-4p\ ^2P_{3/2}$
K I.....	7699	$4s\ ^2S_{1/2}-4p\ ^2P_{1/2}$
Rb I.....	7800	$5s\ ^2S_{1/2}-5p\ ^2P_{3/2}$
VO[a].....	Broad trough ~7851–7973	0–0 band of $B\ ^4\Pi–X\ ^4\Sigma^-$
Rb I.....	7948	$5s\ ^2S_{1/2}-5p\ ^2P_{1/2}$
Na I	8183	$3p\ ^2P_{1/2}-3d\ ^2D_{3/2}$
Na I	8195	$3p\ ^2P_{3/2}-3d\ ^2D_{5/2,3/2}$
TiO[a]	8206 head, degraded to red	0–2 band of $A\ ^3\Phi–X\ ^3\Delta$
TiO[a]	8432 head, degraded to red	0–0 band of $E\ ^3\Pi–X\ ^3\Delta$
Cs I	8521	$6s\ ^2S_{1/2}-6p\ ^2P_{3/2}$
CrH	8611 head, degraded to red	0–0 band of $A\ ^6\Sigma^+–X\ ^6\Sigma^+$
FeH	8692 head, degraded to red	1–0 band of $A\ ^4\Delta–X\ ^4\Delta$
Cs I	8943	$6s\ ^2S_{1/2}-6p\ ^2P_{1/2}$
H_2O[b] ...	Broad trough around ~9300	$\nu_1+\nu_3=3$
VO[a,b]	Broad trough ~9540–9630	1–0 band of $A\ ^4\Pi–X\ ^4\Sigma^-$
FeH	9896 head, degraded to red	0–0 band of $A\ ^4\Delta–X\ ^4\Delta$
CrH	9969 head, degraded to red	0–1 band of $A\ ^6\Sigma^+–X\ ^6\Sigma^+$

[a] Feature not seen in all L dwarfs.
[b] Contaminated by telluric absorption bands.

Figure 10: Taken from Table 4 in Kirkpatrick et al. [8]. A list of the major atomic and molecular absorption features Kirkpatrick identified in the spectra of his L-dwarfs. Note that his observations at the time of this paper only included wavelengths from 0.6 – 1 μm.

The spectral observations Kirkpatrick used to develop his classification scheme only covered wavelengths from 0.6 to 1 μm. Even in this small far-optical wavelength range, he was able to detect multiple atomic and molecular species in the spectra of his L-dwarfs. His table of important spectral features is provided in Figure 10.

In his paper, Kirkpatrick provided a "recipe for L-dwarf spectral classification" using optical spectra. This recipe involved calculating spectral ratios to find the strength of the oxide bands, hydride bands, and alkali features as well as a measurement of the redness of the object and amount of broadening seen in the potassium doublet at about 0.77 μm. Once these measurements were obtained, tables from the paper could be used to determine a numerical subtype. [8]

Geballe et al. [34] later developed a classification scheme for L-dwarfs based on infrared observations from 0.6 – 2.5 μm. The "recipe" used by this team involved measurements of water absorption bands at 1.15 and 1.5 μm, methane bands at 1.6 and 2.2 μm, and two color indices. The infrared classifications were designed to be consistent with Kirkpatrick's optical classifications, although the infrared and optical types for the same object do not always agree.

Further observations of L-dwarfs and comparison to theoretical atmospheric models have revealed that L-dwarf atmospheres contain large amounts of CO gas as well as cloud layers of liquid iron, corundum, and dusty silicates such as enstatite and forsterite [25,35,36].

3.2 T Type

The T-type, ranging in temperature from about 1300 K to 700 K [33], was defined by Burgasser et al. [12]. The classification indices used for T-dwarfs rely solely on near-infrared

observations—due to the dimness of T-dwarfs in the optical regime—and are based on the same measurements of water and methane absorption used for L-dwarfs [34].

The main spectral indication of the transition from late-L to early-T type is the appearance of methane. Methane absorption features at 1.6 and 2.2 μm deepen with each T subtype, as seen in Figure 11. The water band near 0.93 μm also becomes deeper as a brown dwarf cools through the T-types [12].

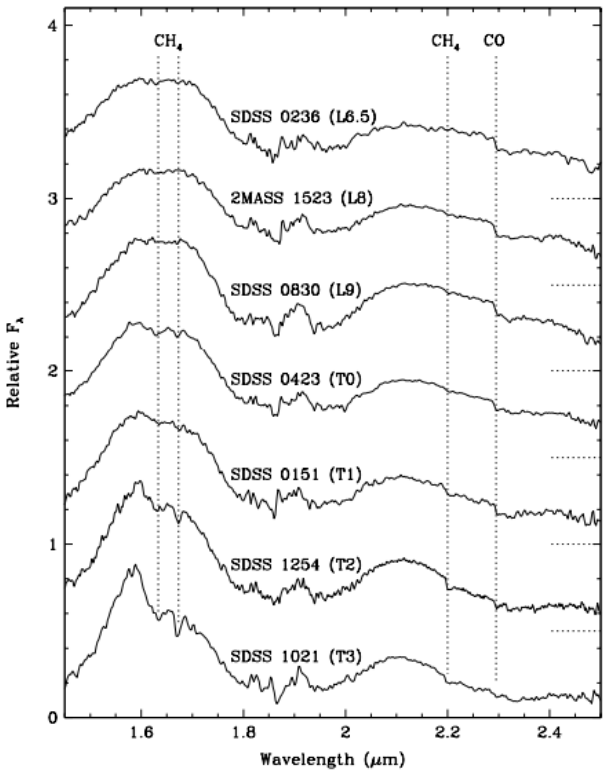

Figure 11: Taken from Figure 3 of Geballe et al. [34]. Comparison of near-infrared spectra of late-L and early-T brown dwarfs. Note the onset of methane absorption at 1.6 and 2.2 μm in the T-dwarfs.

Features denoting silicate and iron clouds are no longer seen in T-dwarf spectra, suggesting that these clouds dissipate at cooler temperatures [37]. Instead, condensation curves such as those shown in Figure 12 predict that salt and sulfide clouds take over [36].

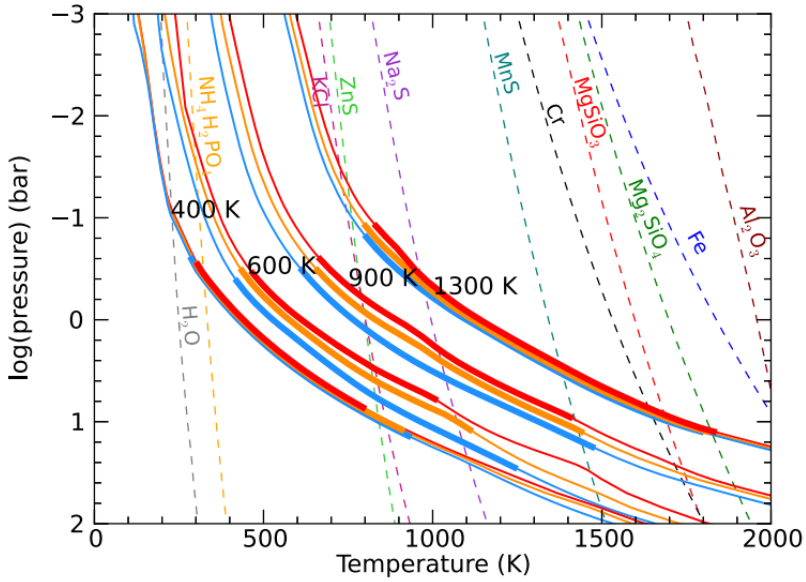

Figure 12: Taken from Figure 3 of Morley et al [36]. The solid-colored lines are condensation curves for brown dwarfs of different effective temperatures. As you move deeper into a brown dwarf, the pressure and temperature both increase. Dotted lines denote stable regions for various condensates. The different condensates are stable at different depths within the atmosphere, resulting in layers of clouds. Note how Na_2S and sulfides such as ZnS and MnS are stable fairly high-up in the atmospheres of T-dwarfs (shown by the 1300K and 900K curves).

3.3 Y Type

Y-dwarfs are the coolest brown dwarfs known to date, ranging from about 700 K down to at least 300 K [14]. The extremely cool temperatures of these objects have made them difficult to observe spectroscopically. Because few spectra of Y-dwarfs have been obtained as of now, the Y-type is not as well defined as the other two types.

Theoretical calculations predict that Y-dwarfs have clouds layers composed of sodium, potassium, water, and ammonia [36]. Cushing et al. [14] present a loose classification scheme based on the appearance of ammonia absorption around 1.5 μm, but suggest that it would be more effective to develop a classification scheme based on spectral features in the mid-infrared where Y-dwarfs shine the brightest. It is expected that the era of the James Webb Telescope will

allow for mid-infrared observation of many more Y-dwarfs and result in a more detailed characterization of the Y spectral type.

3.4 The L/T Transition and Best's Gap

As a brown dwarf transitions from L- to T- type, complicated changes take place in its atmosphere. Much work has been done since the classification of L- and T-dwarfs to develop theories that explain how and when these changes occur. Many questions have been answered, but many remain. Thus, I was particularly interested in using the model fits generated for this project to analyze how well current models are able to replicate the spectra of L/T transition objects. I also wanted to develop a temperature/spectral-type relationship that could shed light on one of the ongoing debates regarding L/T transition objects: whether there is a gap or a pileup of objects in the L/T transition. Our research group refers to this question as "Best's gap," named after William Best's 2021 paper [40].

The initial inspiration for this project came from the observation that some authors present their results in terms of spectral type, others plot in terms of estimated effective temperature, and still others use J-K color. While these three values are expected to be loosely correlated, there is not a defined one-to-one conversion. This can result in some confusion, and we hypothesized that this could be the cause of the "Best's Gap" debate.

For example, the evolutionary models presented by Saumon & Marley [38] predict a pileup of brown dwarfs of temperatures from 1200-1400 K, as shown in Figure 13. Kirkpatrick et al. [39] performed an observational survey of brown dwarfs out to 20 pc and observed this same predicted pileup, as shown in Figure 14. Both papers refer to this temperature range as the "L/T transition."

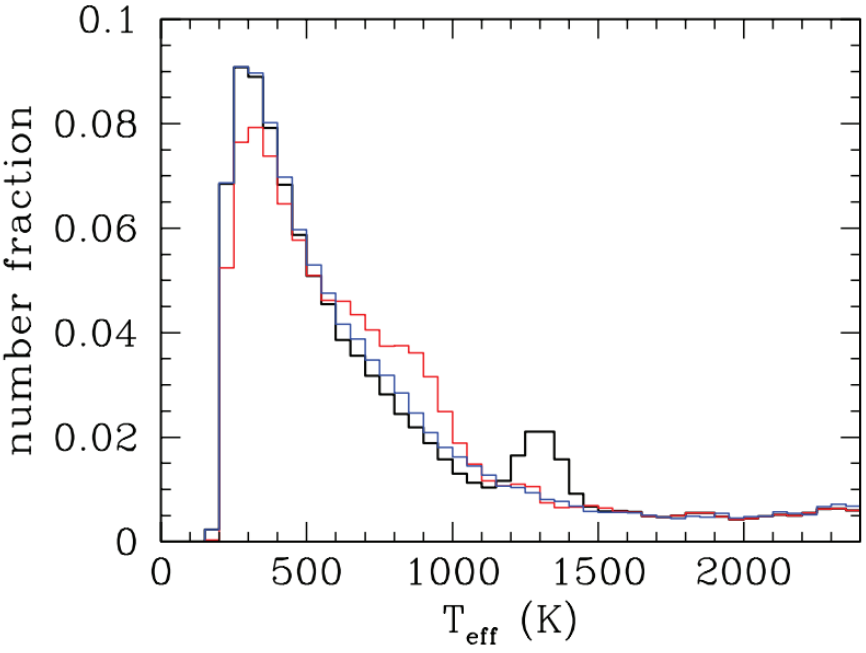

Figure 13: Taken from Figure 13 from Saumon & Marley [38]. A plot of the predicted number fraction of brown dwarfs of different temperatures within the galactic disk, based on the evolutionary atmospheric models presented in their paper. The red curve corresponds to the cloudy model set, the blue curve corresponds to the cloudless model set, and the black curve corresponds to a hybrid model set in which clouds clear away at the L/T transition. The authors of [38] note that the hybrid models predict a pileup of objects around 1200-1400K.

On the other hand, Best et al. [40] performed an observational survey of brown dwarfs out to 25 pc and reported a dearth of objects "in the L/T transition," apparently in direct conflict with previous works. The plot from Best et al. is provided in Figure 15. Note that the results from this paper were presented in terms of J-K color and spectral type rather than temperature.

We speculated that the lack of a clear conversion from spectral type to temperature to color for brown dwarfs could be the cause of these apparently conflicting results. Best et al. observe that the data shown in Figure 15 would no longer be in conflict if either the Saumon & Marley predictions or their own observations were shifted by 0.5 magnitudes in J-K color. Noting that the Saumon & Marley models are generated based on temperature rather than color, this seems

feasible. I sought to more clearly define the correlation between J-K color, temperature, and spectral type in order to explore this possibility.

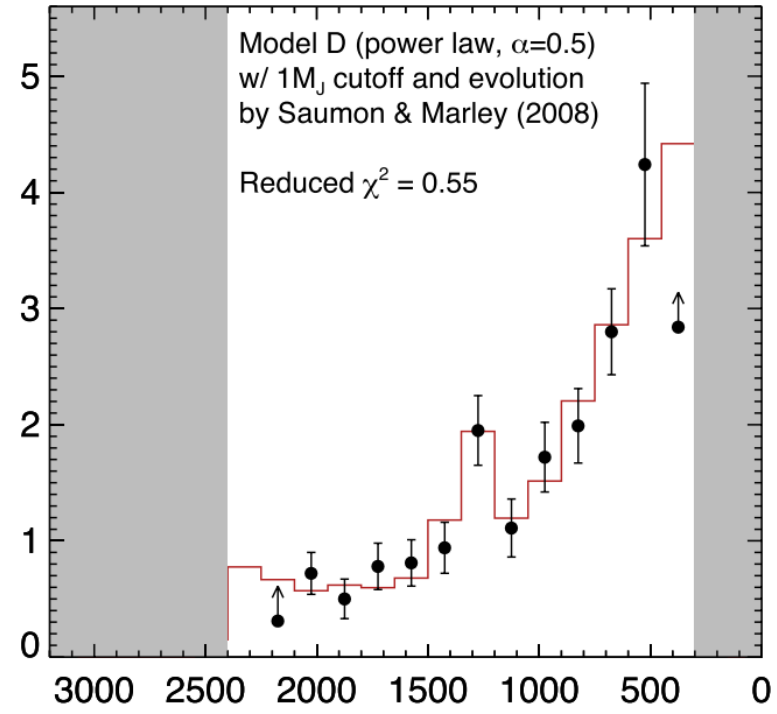

Figure 14: Taken from Figure 28 of Kirkpatrick et al. [39]. The measured space densities resulting from their survey out to 20 pc are given in black. The red curve gives predicted space densities based on one version of the Saumon & Marley [38] evolutionary models. Both the measured and predicted data show a pileup of objects in the bin corresponding to effective temperatures of 1200-1400 K.

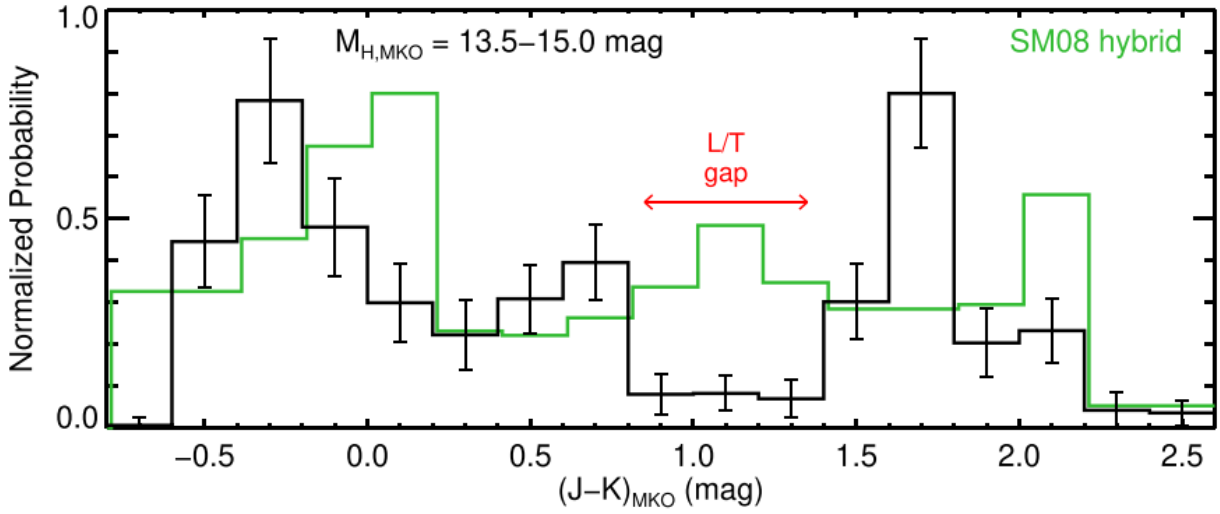

Figure 15: Taken from Figure 15 of Best et al. [40]. This plot shows the measured space densities of brown dwarfs of different $(J-K)_{MKO}$ colors (black) based on an observational survey out to 25pc. Predicted space densities given by the Saumon & Marley hybrid models [38] are shown in green.

Chapter 4

Theoretical Models

Since the first observations of brown dwarfs, multiple groups have been working to develop and refine brown dwarf atmospheric and evolutionary models. These models serve as tools for explaining the physical processes behind the observed spectral features of brown dwarfs. Comparison of real data to theoretical models can also show gaps in our theoretical understanding of the physics and chemistry in brown dwarf atmospheres: where the models and data disagree, there is something lacking from the theory.

Although multiple model sets exist for brown dwarf atmospheres, this project solely uses models originating from the Ackerman, Saumon, and Marley [35, 38] group. Future work could involve the use of other model sets to compare and contrast resulting fits, but that is outside the scope of the current project.

4.1 Main Parameters of the Ackerman, Saumon, and Marley Models

The foundational model grids of this group are generated based on parameters of effective temperature, surface gravity, mixing, and sedimentation. Here, I explain the meaning of each of these parameters.

The effective temperature of a brown dwarf is essentially the temperature of its surface or photosphere. This is not an average or global temperature by any means: the temperature of the

atmosphere will increase with depth. So, a brown dwarf with an effective temperature of 2400 K really is significantly hotter below the surface. However, the light that we observe at our telescopes originates from the surface of the brown dwarf, so the effective temperature is generally what we will measure from this light. The effective temperature grid of the models used in this project ranges from 2400 K down to 200 K and has a varying resolution starting at 100 K for the hottest temperatures and reaching 25 K for the coolest temperatures.

Surface gravity refers to the value of the gravitational acceleration constant at the surface of the brown dwarf. This value depends on both the mass and radius of the object, and thus conveys information about density as well. Surface gravity can be used as an indicator of age: younger brown dwarfs are expected to have lower surface gravities because they are still contracting [42]. This value is usually either given as g in CGS units (cm/s^2) or log g. The surface gravity grid of these models ranges from 10 to 3000 cm/s^2, with varying resolution.

The models also use a parameter called the vertical eddy diffusion coefficient (k_{zz} with units of cm^2/s) that controls the amount of vertical mixing taking place in the atmosphere. This coefficient relates to the vertical mixing time t_{mix} and the scale height H according to Equation 2 from [43]. I have briefly discussed how different cloud species are stable at different atmospheric depths: vertical mixing allows convection to pull molecules from deeper in the atmosphere and deposit them in higher layers where they would usually not be stable. The mixing parameter is given for each model as $\log(k_{zz})$ and can take values of 0, 2, 4, or 6, where larger k_{zz} corresponds to a shorter vertical mixing time/more vertical mixing [41,43,63].

$$t_{mix} = \frac{H^2}{k_{zz}} \qquad \textbf{Equation 2}$$

The sedimentation parameter, f_{sed}, is a measure of how efficiently cloud particles are able to grow. This unitless value is defined by Ackerman & Marley as the "ratio of the mass-weighted sedimentation velocity to the convective velocity scale" [35]. Larger values of f_{sed} correspond to generally larger cloud grains, which then quickly rain out of the upper atmosphere due to their heavy weight. Smaller values of f_{sed} result in smaller cloud grains, which are able to collect in the atmosphere and create thicker clouds. Thus, even though individual particle size grows with increasing f_{sed}, the thickness of the physical clouds in the upper atmosphere is inversely related to f_{sed} [38]. Values for f_{sed} can be 1, 2, 3, 4, or "nc"/ "none" (referring to cloudless model atmospheres).

4.2 Specific Model Subsets Used in This Project

Even within this one modeling group, different iterations of the models exist. In this section, I describe the different model subsets used in this project and their additional parameters. The models from each subset described below were combined into one conglomerate model library that was used to find the best-fit model for each target brown dwarf.

4.2.1 S&M 2008 Models

Approximately half of the models used in this project come from the set presented in Saumon & Marley [38]. The grid includes 1,184 cloudy or hybrid models (cloudless but with vertical mixing still permitted) as well as 157 cloudless models with f_{sed} = "nc" and $k_{zz} = 0$. These models come in temperatures from 300 K to 2400 K and have log g values from 3.5 to 5.5. The grid included k_{zz} values of 0, 2, 4, or 6 and f_{sed} values of "nc," 1, 2, 3, or 4.

A small handful of these models have metallicity [M/H] included as an extra parameter. Metallicity, or the ratio of hydrogen to all other elements, is defined relative to the measured

solar metallicity value. The metallicity options used in this grid are 0, +0.3, and +0.5, where 0 is solar. The models that do not specify a metallicity value all assume a solar metallicity.

The models from this subset will be referred to as the "S&M models" for the duration of this paper.

4.2.2 Morley 2012 Models

I include another 182 models from Morley et al [36]. This subset was an iteration of the S&M models. The same modeling code from Saumon & Marley [38] was used to generate these newer models, but opacity values for some cloud species expected to be found in T- and Y-dwarf atmospheres were added to the line list. These previously "neglected clouds" were Cr, ZnS, KCl, MnS, and Na_2S. Because the focus of this subset was on adding clouds for T- and Y-dwarfs, the temperature grid only ranges from 400 – 1300 K and opacity values for silicate, corundum, and iron clouds were removed from the code. Comparison of the new grid to older models can be seen in Figure 16. Gravity options are 100, 300, 1000, and 3000 cm/s^2. Values for f_{sed} can be 2, 3, 4, or 5. k_{zz} was not incorporated into this model grid, and solar metallicity was assumed for all models.

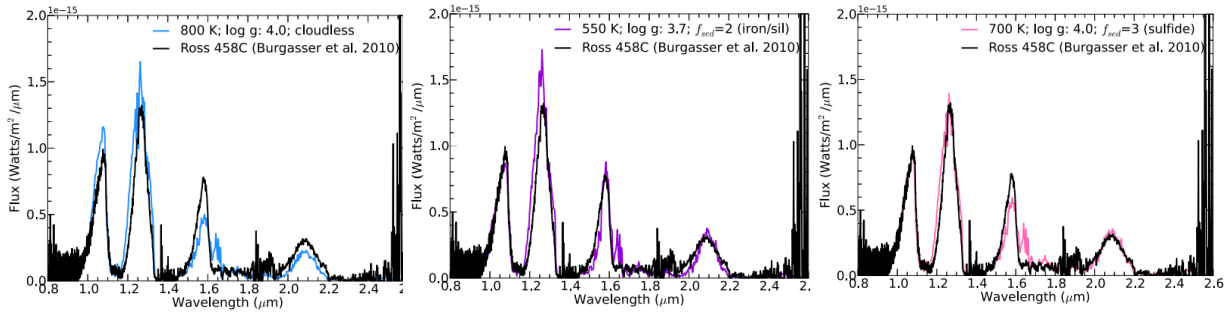

Figure 16: Taken from Figure 11 of Morley et al. [36]. The spectrum of the T8.5 dwarf Ross 458C (black) is compared to its best-fit models from a cloudless grid (blue), a grid including iron and silicate clouds like those seen in L-dwarfs (purple), and a grid including sulfide clouds (pink). The subset of models from Morley et al. [36] includes the sulfide clouds and not the iron/silicate clouds. The sulfide clouds result in the best fit to the peaks around 1, 1.2, and 1.2 µm. The iron/silicate clouds better fit the peak around 1.6 µm. The secondary peak around 1.6 µm that is not fit by any of the modes is due to methane absorption. It is a known problem that the S&M and Morley subsets have outdated methane opacity values.

Note how the model fits in Figure 16 fail to fit the methane feature found around 1.6 μm due to outdated opacity values. This missing methane feature was a recurring problem for this project.

The models from this subset will be referred to as the "Morley 2012" models.

4.2.3 Morley 2014 Models

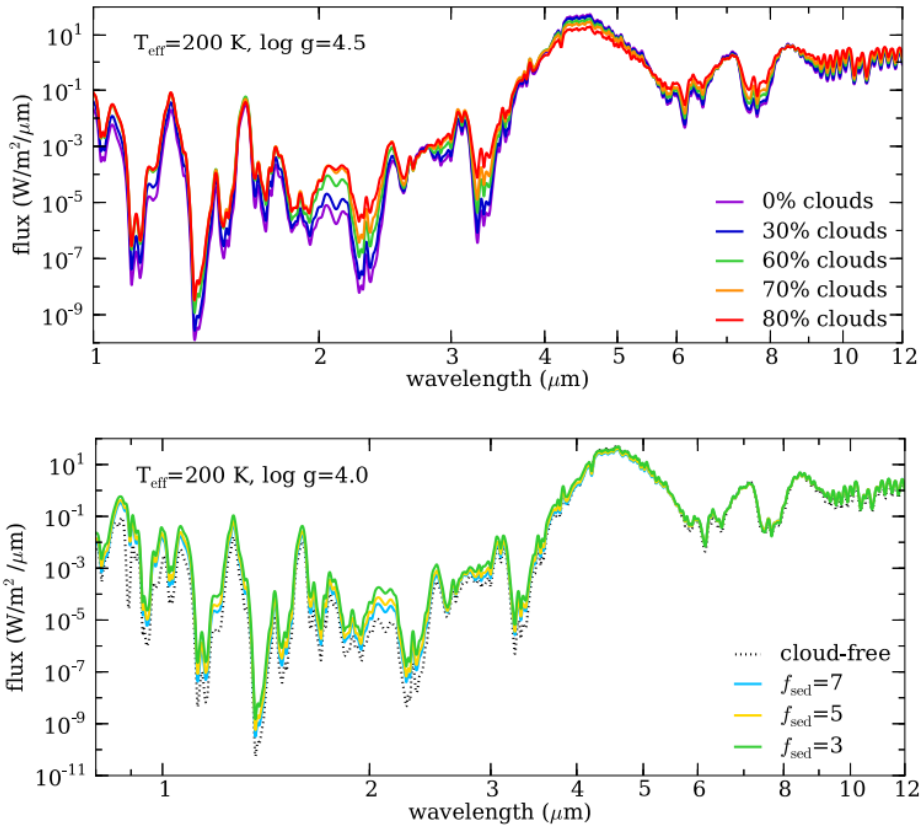

Figure 17: Taken from Figure 11 of Morley et al. [44]. These plots show the effects on the infrared spectrum of a cool Y-dwarf (200K) when the cloud patchiness parameter *h* and sedimentation efficiency parameter f_{sed} are varied.

An additional 76 models come from Morley et al. [44] This subset is another iteration of the S&M models and focuses on incorporating water clouds in order to better model Y-dwarfs. The temperature grid ranges from 200 – 450 K and gravity options are 10, 30, 100, and 300

cm/s^2. Most of these models have $f_{sed} = 5$, although options for $f_{sed} = 3$ and 7 were included only for the models with a surface gravity of 100 cm/s^2.

An additional parameter was included in these models in order to account for possible cloud patchiness. This parameter is called *h* for "cloud holes" and gives the fraction of the surface area of the atmosphere that is made up of holes in the clouds. Most of the models in the grid assumed $h = 0.5$, although the models with a surface gravity of 300 cm/s^2 were given *h* values ranging from 0.2 to 0.8 (in increments of 0.1). The effects of varying *h* and f_{sed} are illustrated in Figure 17.

Models from this subset did not often appear in the model fits to L- and T- dwarfs performed as a part of this project; the cool temperatures of these models are meant to match the atmospheres of Y-dwarfs. However, there was a possibility that the L- and T- dwarfs could be binary systems with a dim Y-dwarf, so it was worth including these models especially when performing binary fits.

The models from this subset will be referred to as the "Morley 2014" models.

4.2.4 Sonora Bobcat Models

The other large subset of 1,209 models comes from the Sonora Bobcat grid presented in Marley et al. [41]. The main advantage of this subset compared to the other three was the inclusion of updated methane opacity values that better fit the methane features found in L/T transition objects and T-dwarfs.

The models in this grid have temperatures ranging from 200 – 2400 K. Surface gravity options are 10, 17, 31, 56, 100, 178, 316, 562, 1000, 1780, and 3160 cm/s^2. The drawback to this subset—and the reason that the S&M models were still included even with the outdated methane

values—is that clouds were not included in the modeling code. Thus, f_{sed} is "nc" for the entire grid and k_{zz} was not used.

Metallicity is included as an additional parameter and can be [M/H] = 0, +0.5, or -0.5 (again with 0 corresponding to solar metallicity). The final parameter used for these models is an assumed C/O ratio. Most of the models assume a solar C/O ratio, although the solar-metallicity models with a surface gravity value of 1000 cm/s^2 give the option for C/O = 0.5 or 1.5 (corresponding to either 0.5 or 1.5 times the solar value). The impact of these two parameters as well as surface gravity and temperature on the Bobcat models is illustrated in Figure 18.

Models from this subset will be referred to as the "bobcat" models.

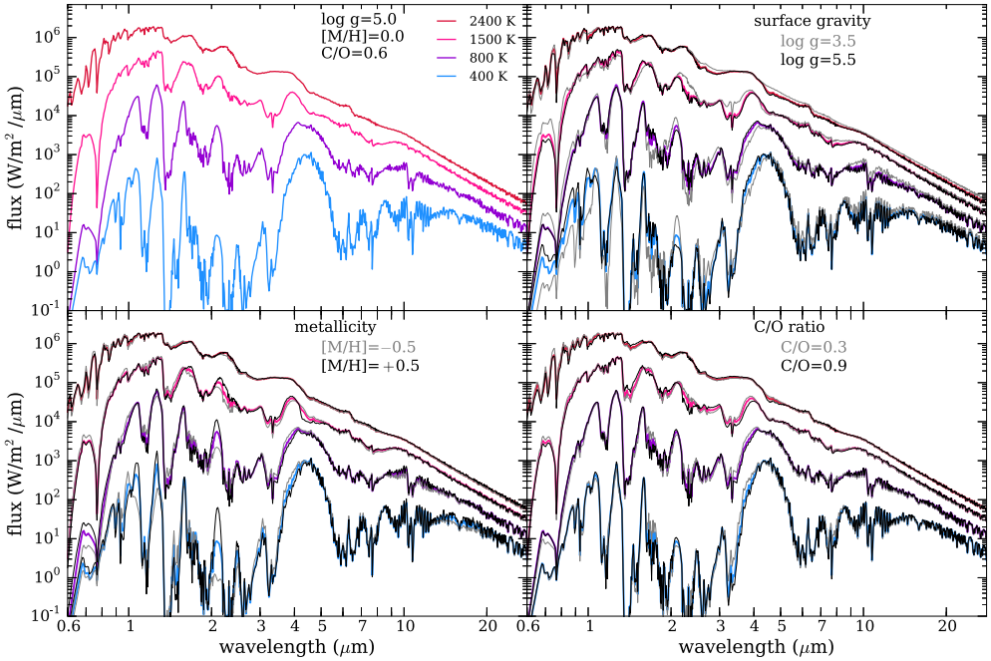

Figure 18: Taken from Figure 2 of Marley et al. [41]. Plots illustrating the effects of temperature, surface gravity, metallicity, and C/O ratio on models from the Sonora Bobcat grid. Temperature has the most dramatic impact on the spectrum, but the other three parameters are useful for fine-tuning fits of models to data.

Chapter 5

Spectral Fitting/ The Code

The spectral fitting code used in this project was originally created as a means of finding unresolved brown dwarf binaries using the methods developed in [45, 46, 47]. For this project, the code was predominantly used in the single-fitting mode, although the binary-fitting feature was used for a small portion. In this chapter, I describe the development of the code, where the code can be accessed, its single- and binary-fitting capabilities, and planned improvements.

5.1 Development of the Code

The development of the code was an iterative process that began before my time at BYU and included the work of multiple individuals [48, 49, 50, 51]. I refer readers to my undergraduate senior thesis [52] for a more detailed history of the code.

In summary, as of April of 2020 the binary fitting code was functional and produced results that matched those given in Burgasser et al. and Bardalez-Gagliuffi et al. [45, 46]. However, using the code required running multiple scripts in Perl, C++, and Python as well as editing multiple files by hand. The process was time-intensive, required user input at multiple steps, could only be run on one object at a time, and could take upwards of 1-2 hours per object.

My undergraduate research from 2020-2021 involved re-writing the Perl script in Python, creating a Python pipeline that would run the entire code from a single command, and adding the option to perform fits to multiple objects in one run.

I also added the ability to use real brown dwarf spectra obtained from the SpeX Prism Library [32] as models in lieu of the theoretical models. The purpose of this feature is to be able to link together "families" of similar objects. For example, if a feature in the spectrum of one of the target objects is not well-fit by the theoretical models, a fit to real data could reveal whether or not this feature appears in the spectra of other objects. For the duration of this paper, fits to theoretical models are called "SM" fits (short for "Saumon Models"), while fits to real SpeX spectra are called "RM" fits (short for "Real Models").

The Python pipeline I created as an undergraduate still called the old C++ scripts, so downloading the code and all of the necessary Python packages and C++ libraries was an element of frustration for new users. As a part of this master's thesis, I removed all of the C++ dependencies. Now, the entire code is written in Python and includes only four separate code files. Input parameters are entered into a .txt file as are the names of all of the objects to be fit. The entire fitting process can then be called with a single command and left to run without user supervision.

Other improvements made as a part of this project include cleaner output of results, the option to plot on a log scale, and the ability to mask over user-defined spectral regions (this element was included in the old C++ version of the code but had not yet been added to the Python version). I also adapted the code to run well for spectra taken with different instruments. Specifically, capabilities have been added for data obtained with the Spitzer IRS, SpeX, AKARI, and TRIPLESPEC instruments.

5.2 Accessing and Running the Code

All of the files needed to run the code can be found at the following GitHub address: https://github.com/savanahkay/binary-fit.git. Future students at Brigham Young University can also find the code on the data drive of the upstairs lab machines in the data/StephensBinaryFittingCode folder or on the Google Drive folder used by Denise Stephen's research group (StephensResearchGroup/BinaryFitting/Code; access will need to be granted by Denise Stephens).

Running the code requires installing Python 3 and the following packages: numpy, scipy, tqdm, os, pandas, itertools, and matplotlib. A section providing a more detailed description of the code as well as instructions on how to use the parameter files and call the code is given in Appendix 1 of this paper.

5.3 Single Fitting

The single-fitting element of the code uses simple optimization of the goodness-of-fit statistic (also called an "adapted χ^2 value" in [45]) described in Cushing et al. [47] to match each object to its best-fit model. This statistic, G_k, is defined in Equation 3.

The summation over λ represents summing over all the wavelength values included in the data. The variables w_λ , f_λ , and σ_λ are the weight, flux, and error of the data at each wavelength, $F_{k,\lambda}$ is the flux of the kth model at each wavelength, and C_k is the scaling factor used to scale the kth model to fit the data. The optimization function (I use the scipy "optimize.minimize" function with the numerical Nelder-Mead algorithm option) minimizes G_k by allowing C_k to fluctuate. This optimization is performed for each model, and the code then sorts the fit results by G_k. The model with the smallest G_k is the best fit for that object.

$$G_k = \sum_\lambda w_\lambda \left(\frac{f_\lambda - C_k F_{k,\lambda}}{\sigma_\lambda}\right)^2 \qquad \textbf{Equation 3}$$

I note that the current iteration of the code assumes equal weighting of all data points, so the w_λ term in Equation 3 is set to 1 at all wavelengths. This weighting term should be implemented for situations in which the data being fit does not have a consistent resolution across its entire wavelength domain: for example, in cases where different spectral regimes were obtained with different telescopes. The error term was also set to 1 for all wavelengths for this project because some of the archival data had recorded error values of zero at some wavelengths, resulting in division by zero. The error term could be easily re-implemented for future projects.

5.4 Binary Fitting

The binary fitting process is based on the methods described in [45,46]. First, composite spectra representing the spectra of unresolved binary pairs are generated by adding the fluxes of two individual model spectra at each wavelength. Every possible combination of two individual model spectra is used to generate the full suite of composite models.

The algorithm then optimizes the same goodness-of-fit statistic described in the last section for each composite model. The composite model with the lowest G_k value is considered to be the best binary fit.

Once both a best single fit and best binary fit have been determined for the object in question, the goodness-of-fit statistics for the two best fits can be used to calculate an η value according to Equation 4 from [45]. ν_{single} and ν_{binary} represent the degrees of freedom of the single and binary fits, respectively. The η value is then used in an F-test to determine the

likelihood that the binary model is a better fit than the single model. If the code returns a 95% likelihood or higher, the object is considered to be a likely binary.

$$\eta = \frac{\min\{G_{k,single}\}/\nu_{single}}{\min\{G_{k,binary}\}/\nu_{binary}} \qquad \textbf{Equation 4}$$

I note that the current code follows the suggestions of [45] and uses the number of data points used in the fit for the degrees of freedom. Because the single and composite models have the same number of data points, the ν values are equal and cancel out. This method of calculating an η value results in an unexpectedly high number of likely binaries.

Also, this statistical method does not consider the multiple model subsets used and their slightly different parameters/inconsistent parameter grids. We observed that some of the objects that were marked as likely binaries were best fit by composite models that were the sum of two models with the same effective temperature from different subsets: for example, a 1200 K S&M model and a 1200 K bobcat model. I believe that these fits do not represent true binaries, but instead show that the different model subsets have their own individual strengths and weaknesses. For example, the 1200 K S&M model is able to model clouds but has outdated methane opacities, while the 1200 K bobcat model has improved methane opacities but no clouds. In this example, a composite model made of one S&M model and one bobcat would be able to better fit both the methane and clouds simultaneously, and thus have a much lower goodness-of-fit statistic than either model alone.

Because the binary fitting portion of the code was such a small portion of this project, I chose to ignore the η value and instead compare the best binary and single fits for the same object by eye rather than spending a significant amount of time developing a new statistical scheme that would account for the multiple model subsets.

5.5 Planned Improvements

Future work on the code will focus on developing and implementing a new method to statistically compare the single and binary best fits. It is likely that this will require only using a single model set with consistent parameter options. I plan to use the upcoming Diamondback model grid (another iteration of the Saumon & Marley models) for future versions of the code.

I also plan to incorporate a function that will perform error analysis and generate uncertainties for the best-fit parameter estimates. Because the optimization function used in the code is based on a numerical algorithm that starts with a different random guess each run, the code does not always find exactly the same best-fit model for the same object. The variation in best-fit parameters falls within a reasonable range, but some sort of uncertainty estimate would allow for more confident conclusions for future work.

The error and weight values in Equation 3 could also be re-implemented for future iterations of the code.

Chapter 6

Data

Over 300 brown dwarf spectra were fit to models as part of this project. In this chapter, I describe where these data were obtained and, when applicable, how they were reduced.

6.1 Archival Data

The majority of the brown dwarf spectra used in this project were downloaded from the SpeX Prism Library [32] or the BDNYC Database [53]. The data were all obtained with the SpeX spectrograph [54] at the NASA Infrared Telescope Facility (IRTF). The wavelength range for these spectra was generally 0.8-2.5 μm. The resolution of each spectrum was either $\lambda/\Delta\lambda$ = 75 or 120.

The headers of the archival data provided 2MASS J, H, and K magnitudes as well as optical and near-infrared spectral types for each object. The SpeX Prism Library documentation explains that most of this supplemental data was obtained from the brown dwarf archive previously maintained by Gellino & Kirkpatrick [55]. Because this archive is no longer available online, the specific references for each magnitude and spectral type cannot be detailed here.

As described in Chapter 3, the methods for determining optical spectral types differ from the methods for determining infrared spectral types. Optical types are generally only used for characterizing early L dwarfs, as they still emit sufficient flux in the far optical. These early Ls

can also be given infrared types. Cooler brown dwarfs are generally classified only with infrared types as they do not emit much light in the far optical. However, a few of the late L dwarfs and even some of the T dwarfs included in this sample had optical types listed in their headers. Some objects in the sample had both optical and infrared types, while other objects only had one type listed. The optical and infrared types for the same object did not always agree, so the analysis given in Chapters 7 and 8 differentiates between the two typing systems. Only a small handful of the spectral types from the literature included uncertainty estimates, so error bars are not included in this work. Future projects could involve creating spectral type uncertainty estimates.

This archival data was normalized, and thus needed to be flux-calibrated before the model-fitting process. The flux calibration routine used by [51] was incorporated into the main fitting code (see Appendix 1 for the code and instructions) to simplify this process. The 2MASS H and K magnitudes for each object were fed into the code and used along with published 2MASS filter profiles to calibrate each spectrum before the fitting steps.

The object name, spectral types, magnitudes, and references for each of the 306 archival spectra used in this project are given in Appendix 2.

6.2 Parallaxes

Many of the 306 archival objects also had parallaxes published on the Simbad database [56]. Most of these distances were either obtained with GAIA [57,58] or as a part of the Hawaii Infrared Parallax Program [59]. These published parallaxes were used to convert the apparent 2MASS J, H, and K magnitudes into absolute magnitudes.

6.3 New Observations with TRIPLESPEC

We also performed new observations of 16 L- and T- type brown dwarfs with the TRIPLESPEC instrument [60] on the Apache Point Observatory (APO) 3.5-meter telescope. TRIPLESPEC is an infrared spectrometer with a wavelength coverage from 0.95-2.46 μm. The 1.1 arcsecond slit was used, giving a resolution of R = 3500. A detailed explanation of the observations and reduction process is given in Conner Scoresby's senior thesis [61].

The object name, spectral types, magnitudes, and references for these 16 brown dwarfs are given in Appendix 3.

Chapter 7

General Trends

The first focus after performing the spectral fits was to look for overall trends in the data. The analysis of these general trends is presented in this chapter, while a closer look at the results for each individual spectral type is given in the next chapter.

7.1 Temperature vs Spectral Type

I began by plotting the effective temperature of the best-fit model versus the recorded spectral type of each object. Because some objects had both optical and infrared spectral types recorded that conflicted with one another, separate plots were created for infrared types and optical types. Since optical classification is generally not used for spectral types later than L, small black points were used to plot the infrared-type data for later spectral types on the optical plot. These plots are given in Figure 20.

Both the optical and infrared plots show a loose correlation between spectral type and temperature. This correlation has the general shape of a cubic function, with a flat turning point centered near spectral type L8. This flattening of the temperature trend fits with the theory: as a brown dwarf transitions from type L to type T, silicate clouds clear away from the upper atmosphere and allow light from deeper, hotter layers of the atmosphere to shine through. This

causes the decreasing trend in observed effective temperature versus spectral type to slow down temporarily [62,63,35].

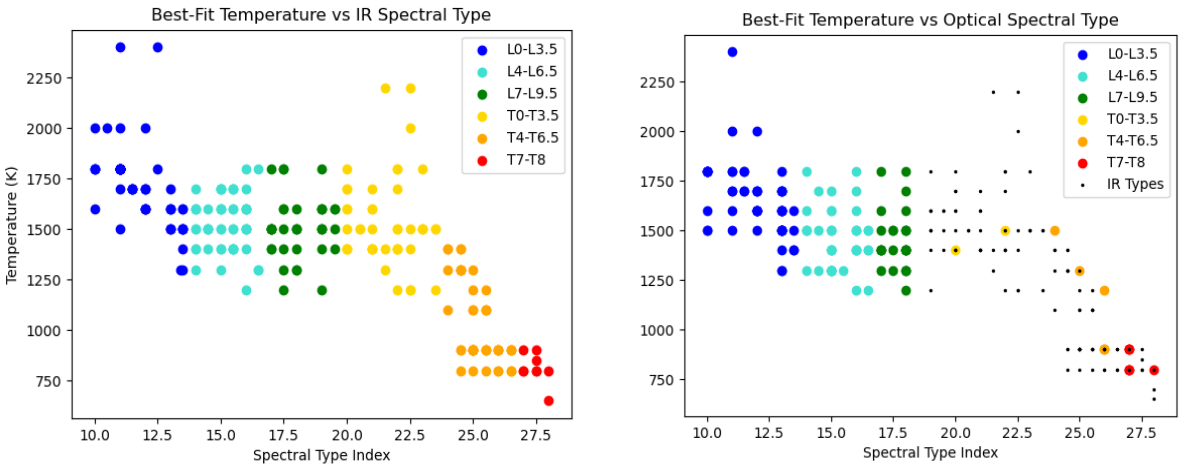

Figure 20: A plot of the temperature of the best-fit model vs recorded spectral type of each object in the sample. Colors represent different spectral type groups. As some objects had both optical and infrared spectral types recorded and the two types did not always agree, separate plots are given for optical and infrared spectral types. Because optical spectral types are usually not assigned to objects later than the L/T transition, later objects with infrared types are plotted as small black dots on the right plot.

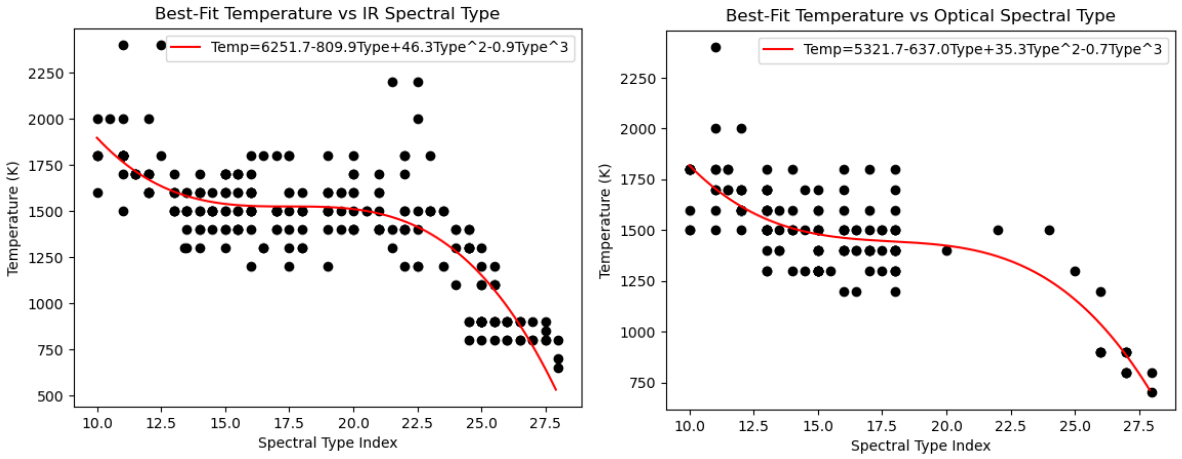

Figure 19: Plots of best-fit temperature versus spectral type for the objects in our sample (black), fit with a cubic regression function (red). The usefulness of this regression function is limited due to the wide spread of temperature possibilities for each spectral type, but at the least provides an estimate for the mean temperature of each spectral type.

In order to quantify this trend, I fit a cubic function to the data. Plots showing the resulting regression curve for both the infrared- and optical-type data sets are given in Figure 19.

I note that, due to the large spread in possible temperatures for each spectral type, the regression functions are not necessarily useful in converting between temperature and spectral type. However, the regression function does provide an estimate for the mean temperature of each spectral type. Comparison of the regression functions based on infrared and optical types shows that the optical types generally correspond to slightly cooler temperatures than the infrared types. This could either be a result of the way in which optical and infrared types are assigned, or observation bias of the different surveys that focus on either optical or infrared classification.

7.2 Absolute J Magnitude vs J-K Color

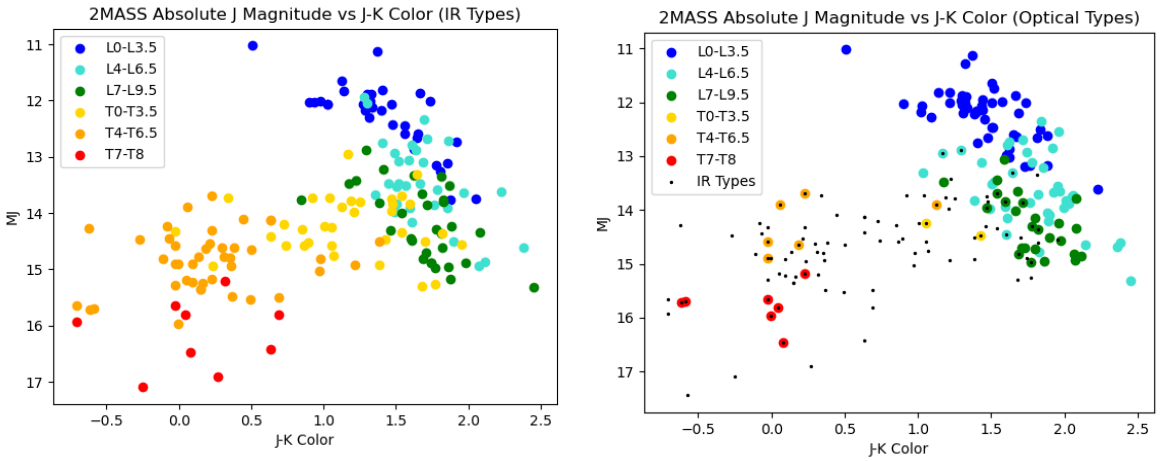

Figure 21: Plots of absolute 2MASS J- magnitude vs 2MASS (J-K) color for the archival objects with published parallaxes. Colors indicate spectral type. As some objects had both optical and infrared spectral types recorded and the two types did not always agree, separate plots are given for optical and infrared spectral types. Because optical spectral types are usually not assigned to objects later than the L/T transition, later objects with infrared types are plotted as small black dots on the right plot.

I next plotted absolute 2MASS J magnitude versus 2MASS J-K color. These plots are given in Figure 21. The plots show an initial reddening with spectral type for early-to-mid L types. This same reddening is described in the literature as being a result of thickening silicate clouds. As the spectral type evolves from late-L to early-T, the J-K color quickly swings leftward

and becomes progressively bluer with spectral type. The literature suggests that this shift to bluer colors is due to the silicate clouds clearing away, allowing light from deeper, hotter layers of the atmosphere to shine through. Methane is also condensing into clouds throughout the T-type sequence and removing light from the H- and K-bands. [63,35,64]

The infrared and optical-type plots match fairly well, although there is a little more scatter in color for the L4-L6.5 optical types than is seen for the infrared types. This scatter seems to line up with the trend observed in the temperature-spectral type plots of Figure 20: if optical types tend to run 1-2 spectral types ahead of infrared types, this could explain both the slightly lower average temperatures for optical types compared to infrared types as well as the inclusion of slightly bluer objects in the L4-L6.5 range for optical types.

The infrared-type plot shows a definite increase in color scatter for the mid-to-late T-dwarfs as compared to the rest of the data. There are not enough late T-dwarfs in the sample to make a conclusive statement regarding this scatter; it could simply be a result of the dimness of T-dwarfs in the near-infrared and resulting uncertainties in the model fits.

Assuming that this scatter is a real effect, one possible explanation is that the salt and sulfide clouds described by Morley et al. [36] have begun to set in for some of the T dwarfs, causing their colors to begin to redden again, while this cloud formation has not yet set in for the bluest objects. Another contributing factor could be the deepening of the water band around 1.2 μm, which removes light from the middle of the J-band. If the water clouds described in [44] are appearing sooner for some T-dwarfs than for others, this could contribute to the scatter in observed colors.

7.3 Implications for Best's Gap

The pileup of objects in the L/T transition predicted by Saumon & Marley [38] and Kirkpatrick et al [39] occurred in the temperature range 1200-1400 K. The temperature versus spectral type plots in Figure 20 and Figure 19 show that objects with spectral types from L3 to T4 can be found with these temperatures. Thus, it would indeed make sense to observe a pileup of objects in this temperature range: the flattening-out of the temperature trend results in a large spectral-type range that could correspond to 1200-1400 K. However, referring to this as a pileup "in the L/T transition" does not seem to be very accurate, both because this temperature range extends to spectral types on either side of the transition and because the archival L/T transition objects could have temperatures as high as 1800 K.

Best et al. [40] observed their gap at a J-K color of about 1. I note that Best used the MKO photometric system to calculate these colors while this project uses the 2MASS photometric system. $J\text{-}K_{MKO}$ of 1 does not correspond directly to $J\text{-}K_{2MASS}$ of 1, so the plots in Figure 21 should be used with caution in the context of Best's gap. However, if $J\text{-}K_{MKO}$ of 1 corresponds to a $J\text{-}K_{2MASS}$ value anywhere from 0.5-1.5, Figure 21 suggests that Best's observed gap would correspond to a much smaller spectral-type range than Saumon & Marley and Kirkpatrick's pileup.

In summary, based on the trends observed in this project, I believe that the issue of Best's gap versus a pileup is an issue of comparing apples to oranges. All three papers could be seeing the same distribution of objects but comparing their data using non-equivalent terms.

7.4 Surface Gravity

I next analyzed the surface gravity distribution of the archival objects. As explained in previous chapters, surface gravity can be used as an indication of age. Objects with lower surface

gravities are thought to be young, fluffy objects that have not yet finished contracting. Theory suggests that there should be some critical mass below which a fragment of a molecular cloud is unable to form a brown dwarf [65]. If this is true, there should be a spectral type/temperature at which young, low-gravity objects disappear.

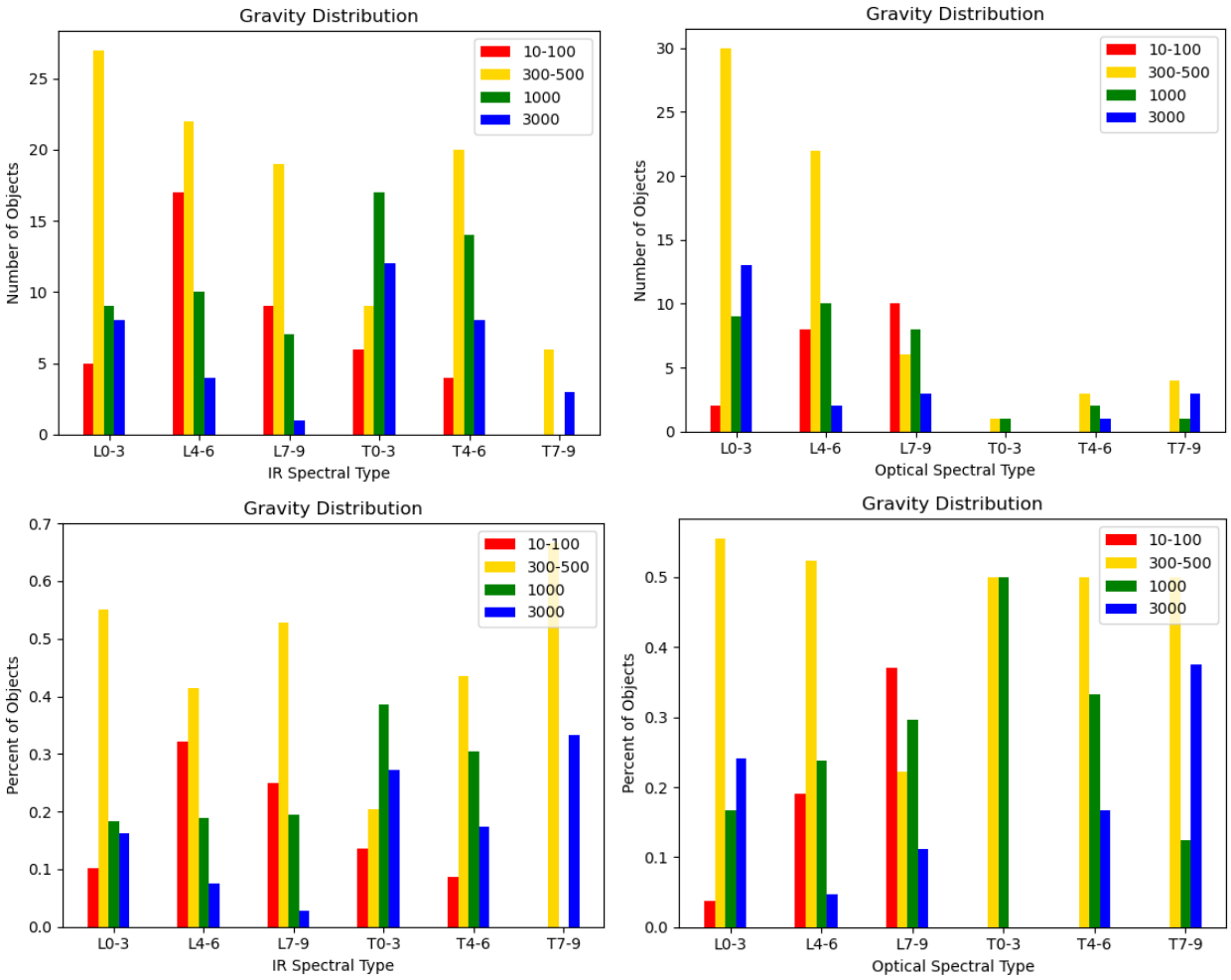

Figure 22: Histograms showing the distribution of surface gravity (based on the parameters of the best-fit model for each object) and spectral type. The plots on the left use infrared spectral types, while the right plots use optical types. The top two plots give the number of objects in each bin, while the bottom two plots give the percent of objects in each bin.

In order to investigate this theory, I created histograms of the surface gravity distribution of my sample objects based on spectral type (again separated into optical and infrared types). Figure 22 gives these histograms both based on the number of objects in each bin (top two plots)

and the fraction of objects in each bin (bottom two plots). I note that the mid- and late- T types are underrepresented in this sample, so the numerical and percentage histograms should be used in tandem to account for this.

The infrared-type histograms show a peak in the distribution of the lowest surface-gravity objects (red bar) at the L4-L6 spectral-type bin. The distribution of these low-gravity objects then falls off with spectral type until disappearing in the T7-T9 bin. The optical-type histograms show a peak in the distribution of these low-gravity objects in the L7-L9 bin. This is consistent with the theory presented in section 7.2: if infrared types tend to lag slightly behind optical types, the L4-L6 infrared bin and L7-L9 optical bin could have a significant overlap.

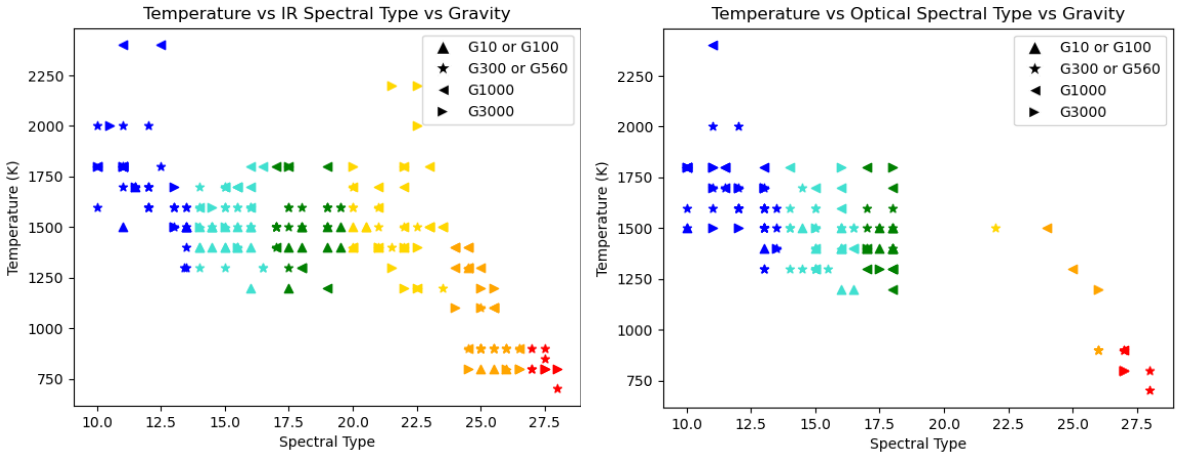

Figure 23: Best-fit surface gravity values have been added to the temperature-spectral type plots given in Figure 20. The up-triangle, star, left-triangle, and right-triangle symbols represent different surface gravity values, listed in increasing order.

I pause here to note a very possible issue with this analysis: there are significantly fewer late T-dwarfs in the sample than there are L- and early T-dwarfs. This is especially true for the subset of objects with optical types. Thus, it is entirely possible that the disappearance of lower surface gravity objects is a result of the smaller sample size and not a true effect. The sample

would need to be extended to include more late T-dwarfs as well as Y-dwarfs in order to make a more conclusive statement.

In Figure 23, I add surface gravity estimates to the temperature-spectral type plots shown previously. There appears to be a slight tendency for lower surface gravity objects to have cooler temperatures than objects of the same spectral type with higher temperatures, especially for the infrared types. It is also interesting that the major outliers in the early L-types (dark blue) are best fit with moderately high surface gravities and that the major outliers in the early T-types (gold) are best fit with the highest surface gravity values.

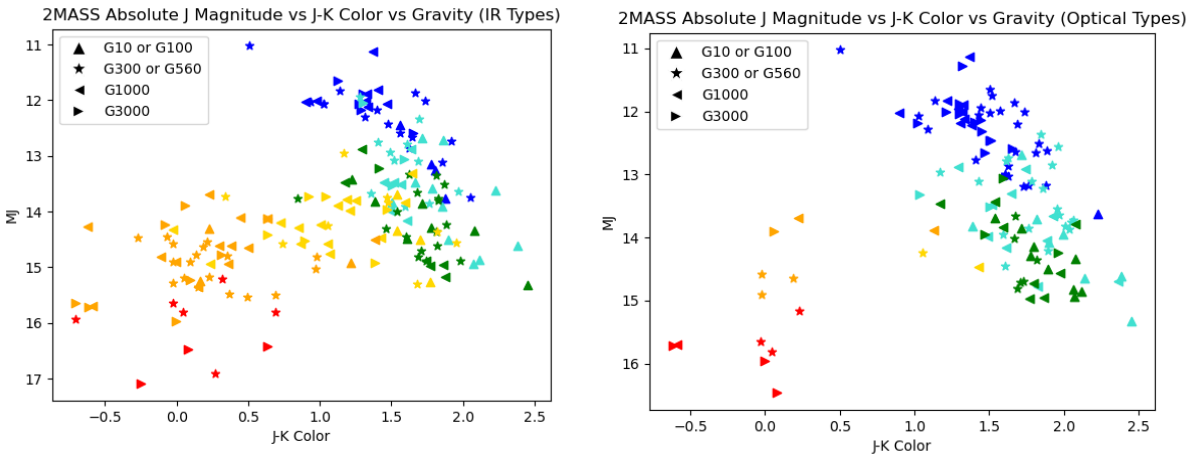

Figure 24: Best-fit surface gravity values have been added to the absolute 2MASS J-magnitude vs 2MASS J-K color plots given in Figure 21. The up-triangle, star, left-triangle, and right-triangle symbols represent different surface gravity values, listed in increasing order.

Figure 24 gives the absolute 2MASS J-magnitude vs 2MASS J-K color plots shown previously, but with surface gravity information added. The only apparent trend to this plot is that most of the objects in the reddest "elbow" of the curve (colors from 2-2.5) were best fit with the lowest surface gravity values. This lines up with theory: younger objects with lower surface gravities are expected to be able to keep silicate clouds in their upper atmospheres for longer, and thus achieve redder colors than older, higher-gravity objects of the same spectral type [66].

The results presented in this section suggest that there are a few slight trends to the surface gravity distribution that can be explained with theory. At the same time, there is a lot of scatter to the distribution and none of the trends presented above were perfect. A similar model-fitting analysis performed by Stephens et al. [63] suggested that surface gravity is not very well-constrained by fits to the entire near-infrared spectrum. In the future, I plan to fit narrower wavelength regimes that are known to be particularly sensitive to surface gravity (such as the H_2 absorption region in the K-band [64]) to see if clearer gravity trends will emerge. I also plan to generate uncertainty estimates for the best-fit gravity values in order to be able to make more confident observations.

7.5 Clouds

The distribution of cloud sedimentation efficiency (f_{sed}) values for the objects in my sample is shown in Figure 25. For both the infrared-type and optical-type plots, it is apparent that L-types tend to be best-fit by f_{sed} values of 1, 2, or 3, with 2 being the most common value on average. For the infrared-type plot, the early T-type objects show a large scatter in f_{sed}, with every value represented. We do not see this same scatter for the early T-type objects in the optical type plots, most likely because there are so few objects. Then, for both the infrared and optical plots, cloudless models take over for the mid-to-late Ts, with just a few objects matching with an f_{sed} of 3 or 4.

Recall that smaller values of f_{sed} mean smaller individual cloud particles but thicker, hazier clouds [38]. The atmospheres of L dwarfs are believed to have thick, dusty silicate clouds [35]: this aligns well with f_{sed} values of 1 or 2. Around the L/T transition, these silicate clouds are believed to fall below the atmosphere while sulfide clouds begin to form [35,36]. This

change in upper-atmosphere cloud composition could explain the scatter of f_{sed} values for the early T-types.

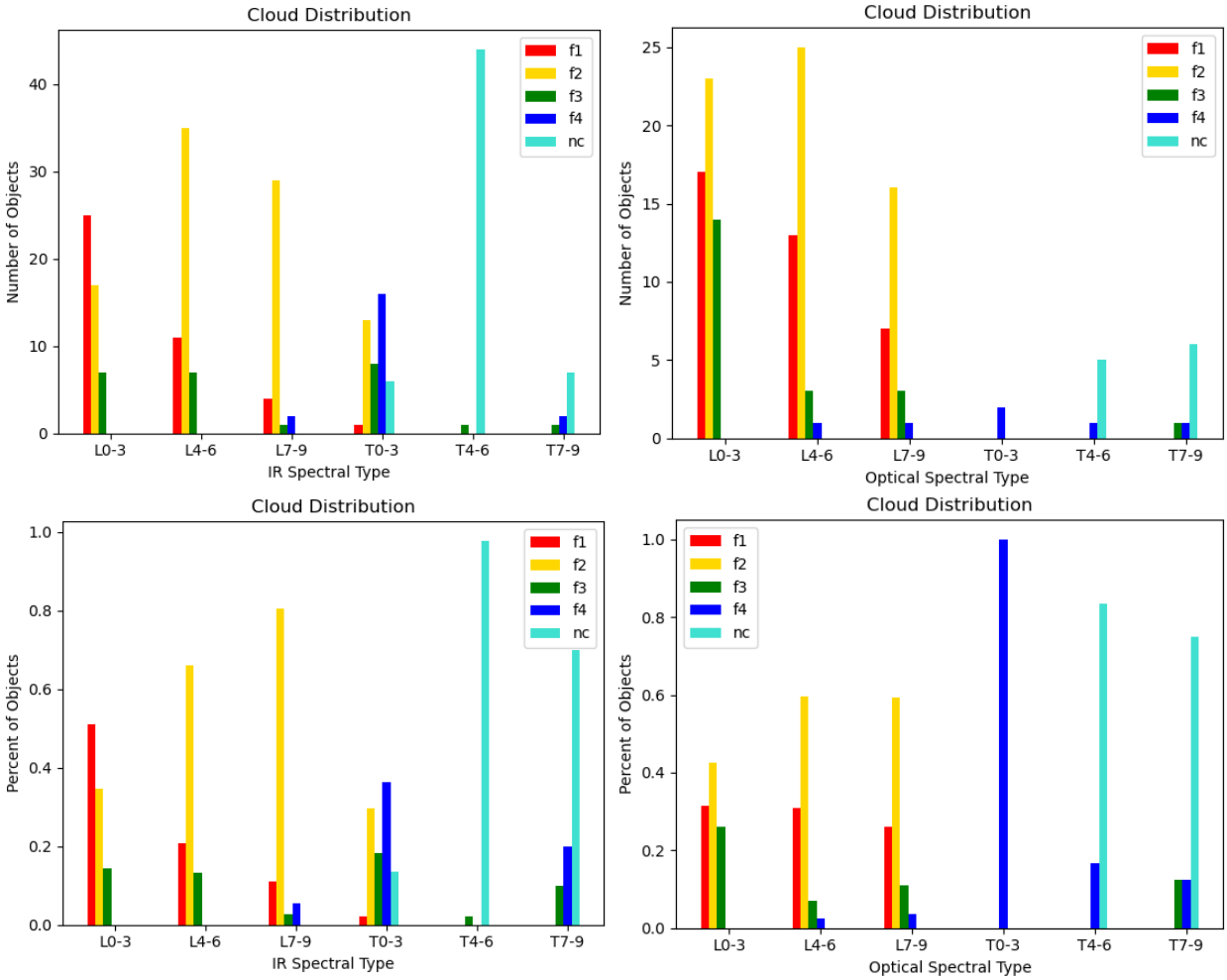

Figure 25: Histograms showing the distribution of the cloud sedimentation efficiency parameter f_{sed} (based on the parameters of the best-fit model for each object) and spectral type. The plots on the left use infrared spectral types, while the right plots use optical types. The top two plots give the number of objects in each bin, while the bottom two plots give the percent of objects in each bin.

The fact that nearly all of the mid-to-late T-dwarfs are best-fit by models with f_{sed} = nc does not necessarily mean that these objects are truly cloudless: further inspection of the model fits shows that many of these objects were best fit by bobcat models (cloudless but with updated methane opacities) rather than S&M or Morley models (which can be cloudless or cloudy, but have outdated methane opacities). Methane absorption is so strong for the T-dwarfs that it

becomes much more important than cloudiness for model fitting. In order to truly see the f_{sed} distribution of mid-to-late T-dwarfs, we would need a cloudy grid of models with updated methane opacities. No such model set has been published to date. I do note that the few T-dwarfs that were not fit by bobcat models generally had high f_{sed} values of 3 or 4, supporting the theory that clouds in T-dwarf atmospheres are thinner than the silicate clouds of L-dwarfs [36].

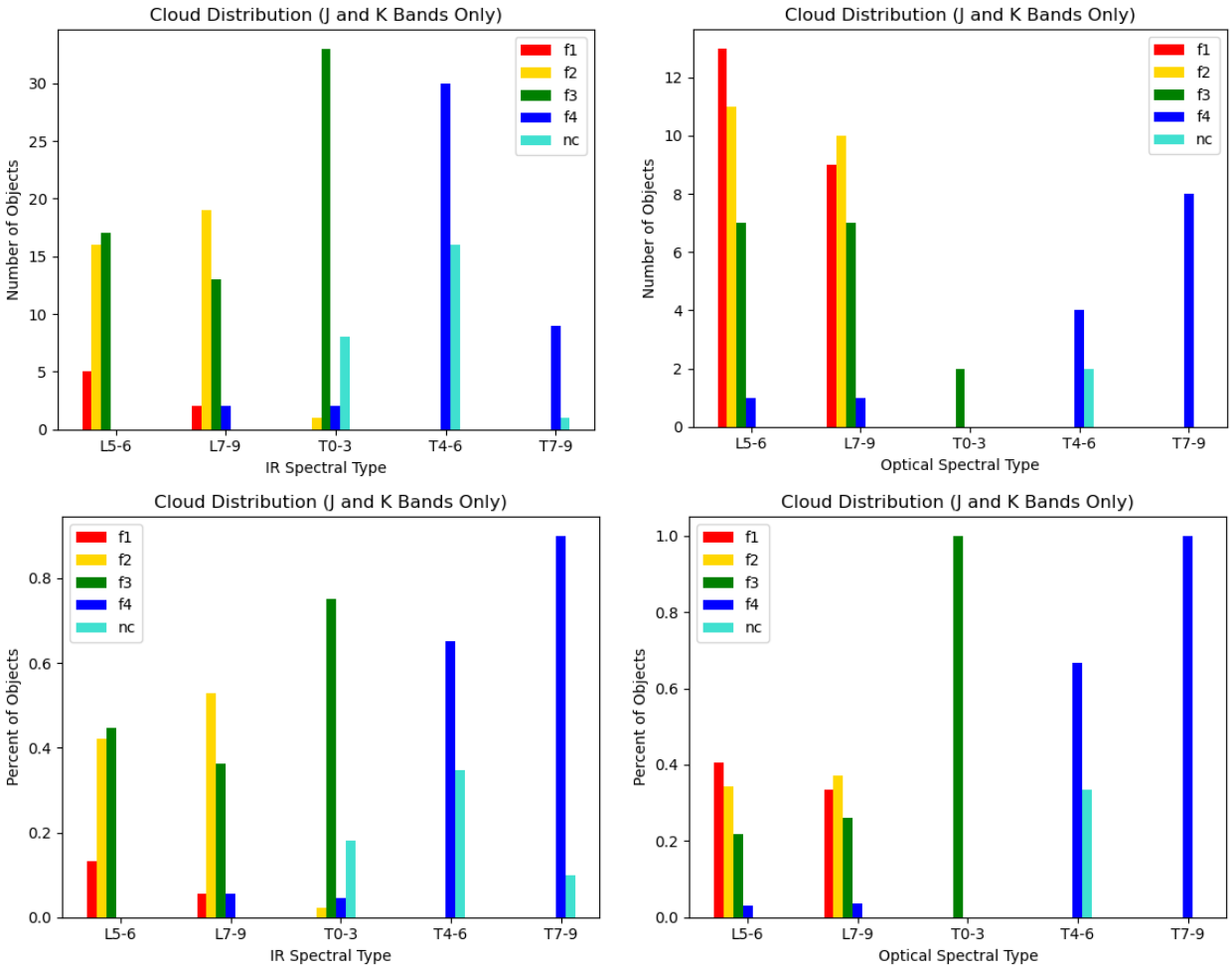

Figure 26: Histograms showing the distribution of the cloud sedimentation efficiency parameter f_{sed} (based on the parameters of the best-fit model for each object) and spectral type. These plots differ from those in Figure 25 in that only the J and K bands were included in the model fitting. This excluded the spectral regions with outdated methane opacities. The plots on the left use infrared spectral types, while the right plots use optical types. The top two plots give the number of objects in each bin, while the bottom two plots give the percent of objects in each bin.

In order to further investigate the effect of methane on the best-fit cloud distribution, I performed new fits for all of the objects in my sample with spectral types of L5 or later. I did not re-fit the objects with earlier spectral types because methane features should not be present in early L-dwarf spectra. For these fits, I used the masking function in the code to limit the fitting to the J- and K-bands, excluding the methane feature at 1.6 μm found in the H-band. Figure 26 gives the resulting cloud distribution of the new fits. This distribution again shows that f_{sed} values of 1, 2, or 3 are the most common for the mid-to-late L-types. However, many more T-types fit to $f_{sed} = 4$ rather than $f_{sed} = nc$ now that fitting the methane was no longer required. It appears that thin clouds remain important for the late T-types.

This observed cloud distribution agrees well with the literature. Stephens et al. [2] performed a similar analysis of the f_{sed} parameter using only the S&M models. They also found that L-dwarfs are best-fit by f_{sed} values of 1 or 2. Their analysis of the T-dwarf fits showed that f_{sed} grew quickly through the early T-types (seen in the scatter of f_{sed} for T0-T3 in my data) and that late T-dwarfs were generally fit by either $f_{sed} = 4$ or $f_{sed} = nc$.

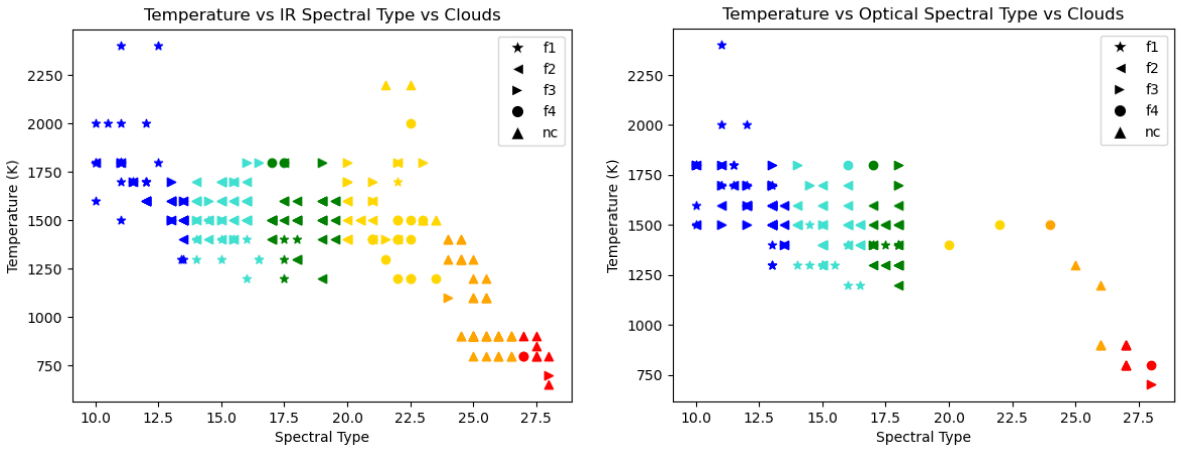

Figure 27: Best-fit f_{sed} values have been added to the temperature-spectral type plots given in Figure 20. The various symbols represent different f_{sed} values.

In Figure 27, the f_{sed} distribution is shown in context of the temperature-spectral type plot. Here we see the same trends observed in Figure 25: f_{sed} generally increases with spectral type until f_{sed} = nc quickly takes over around T4. There does appear to be a slight trend where cloudier atmospheres have lower temperatures for the same spectral type—suggesting that the clouds prevent photons from escaping from deeper, hotter levels of the atmosphere—although this is not a perfect trend by any means.

Figure 28 adds f_{sed} information to the 2MASS J-magnitude vs 2MASS J-K color plot. This figure supports the theory that brown dwarfs with redder colors generally have hazier atmospheres (f_{sed} = 1 or 2) [35]. There is a definite increase in f_{sed} moving from right-to-left (red-to-blue), up until the clouds disappear for the mid Ts.

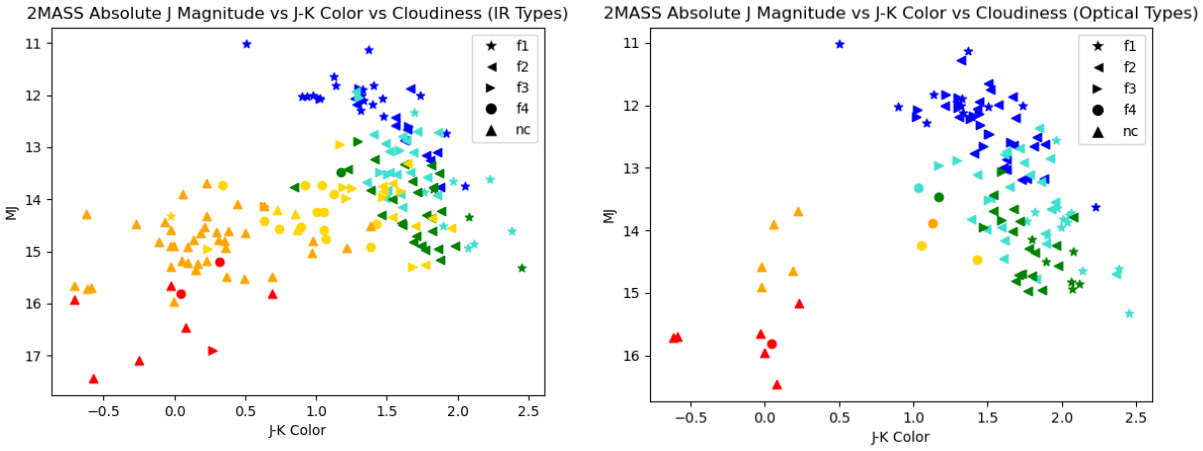

Figure 28: Best-fit f_{sed} values have been added to the absolute 2MASS J-magnitude vs 2MASS J-K color plots given in Figure 21. The various symbols represent different f_{sed} values.

Chapter 8

Results for Individual Spectral Types

Here I present trends seen in the model fits for each individual spectral type. I continue to distinguish between optical and infrared spectral types. When half-types are given, I round down for grouping purposes. For example, objects of type L1.5 are grouped with the L1s. Specific brown dwarfs are referred to by the first four digits of their 2MASS designations (which also correspond to the first four digits of their Right Ascension (RA) coordinates).

8.1 L Types

8.1.1 L0-L3

Fit results for the archival objects of infrared or optical type L0 are given in Figure 29 and Figure 30, respectively. The J-band is generally well-fit for all of these objects. The models consistently are slightly brighter than the data in the H-band around 1.6 μm and dimmer than the data around 1.75 μm, although the discrepancy is slight. Almost without exception, the models underfit the data in the K-band around 2.25 μm.

J0141, J0406, and J1711 all have colder best-fit temperatures than would be typically expected for L0 objects. These objects have been previously flagged in the literature as "peculiar," "gamma," "lg," or ";". All three objects also have more triangular H-bands than the other L0s. They were all fit with surface gravities less than 1000 cm/s^2, while most of the other L0s had gravity fits of 1000 or 3000 cm/s^2. The low gravities of these objects appear to result in

some physical cloud effect that gives the H-band the triangular shape. This agrees with statements made in [90] that a triangular H-band profile is an indication of young age.

The fits for the L1 types, given in Figure 31 and Figure 32, look very similar to the L0 types. The K-band is still generally underfit around 2.25 μm. The models often have a triangular shape for the H-band (similar to the peculiar L0s) that does not match the more rounded shape of the H-band for the data. The model H-bands generally have higher flux peaks than the data H-bands.

The models are still generally underfitting the K-band. However, J1756 and J1440 are both able to match the K-band well (at the expense of the H-band) by fitting to models with temperatures that are noticeably hotter than the other L1s.

The L2 fits in Figure 33 and Figure 34 show that the H-band fits look about the same, although the peaks are not quite as overfit as they were for the L1s. Similar to the two hot L1s, J1431, J1434, and J0921 were able to fit the K-band well but have model temperatures that are abnormally high.

The L3 spectral type (Figure 35 and Figure 36) seems to be a turning point: both the H- and K-band fits are starting to look better, although there are still exceptions.

8.1.2 L4-L6

The L4 fits are shown in Figure 37 and Figure 38. I noted in the last section that L3 is a turning point: spectral types L4-L6 on average have better fits to the K-band than were seen for spectral types L0-L3, although there are exceptions to this. The shape of the H-band shows quite a bit of variation from one object to the next even within the same spectral type. For example, some L4s have very triangular H-bands (like Gliese 417BC), while other L4s have a more

pronounced absorption feature around 1.6 μm that causes the top of the H-band to fall off diagonally to the left. Even more unique is the double-spiked H-band peak seen in J0805.

The L5 (Figure 39 and Figure 40) and L6 (Figure 41 and Figure 42) fits look very similar to the L4s. The K-band is still fitting well, but the models are struggling to fit the varying H-band shapes seen in the data.

8.1.3 L7-L9

Figure 43 and Figure 44 show that the L7 fits generally do very well. There is still variation in the H-band, although the models are usually able to match the general shape. The three worst fits are to the three objects that have H-bands shaped like plateaus. These objects are J2252, J0423, and J0518. All three of these objects also show a slight absorption dip in the K-band around 2.2 μm that is not as pronounced in the other L7s.

The L8 objects (Figure 45 and Figure 46) look very similar to the L7s. Three more H-band plateaus are seen in this spectral type: J0032, J1207, and Gl337CD. These three objects also show the deeper absorption at 2.2 μm seen for the three L7s.

There were no objects with optical type L9. The infrared L9s are shown in Figure 47. The fits for this spectral type are generally poorer than for the mid L-types, both in the H- and K-bands. The object J0328 shows a plateau, while the H-band of J0805 (mentioned previously for its optical type L4) seems to be a cross between a plateau and the more common diagonal slant. This odd shape could be explained if J0805 were an unresolved binary system containing both a plateaued L-dwarf and a more typical L-dwarf.

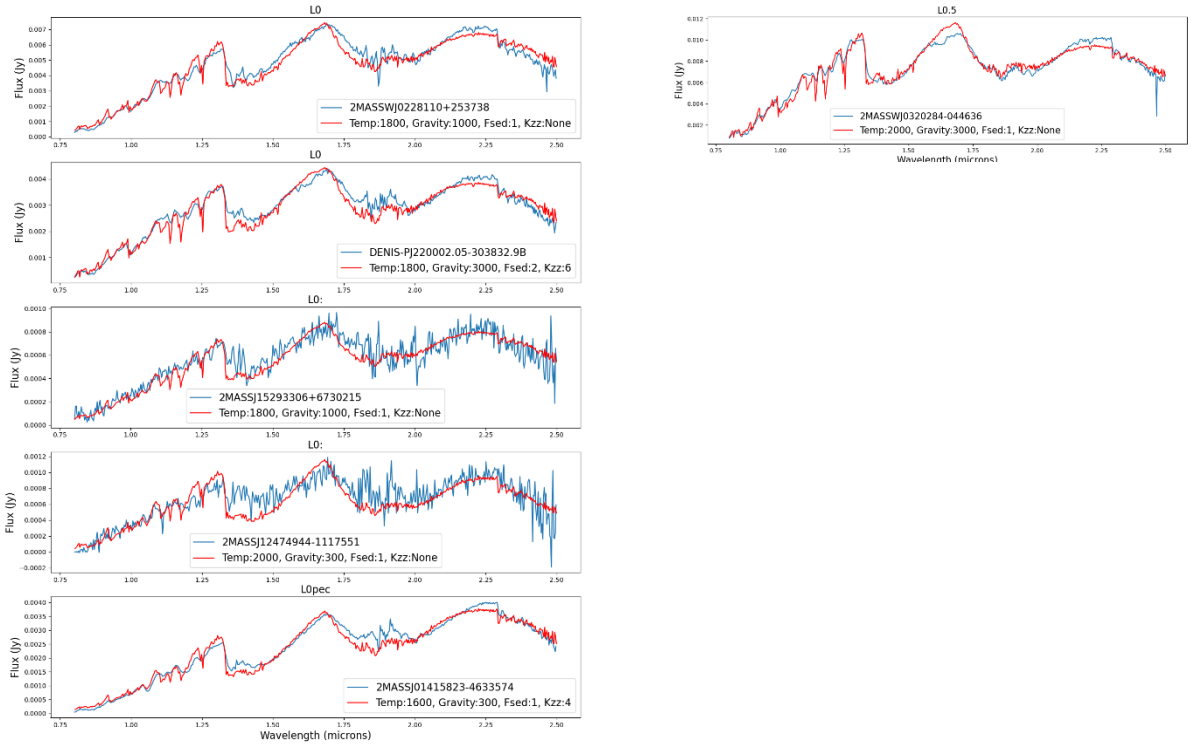

Figure 29: Best-fit models (red) are plotted over the archival spectral data (blue) for all of the objects in my sample of infrared-type L0 and L0.5. The object names and best-fit parameters are given in the plot keys.

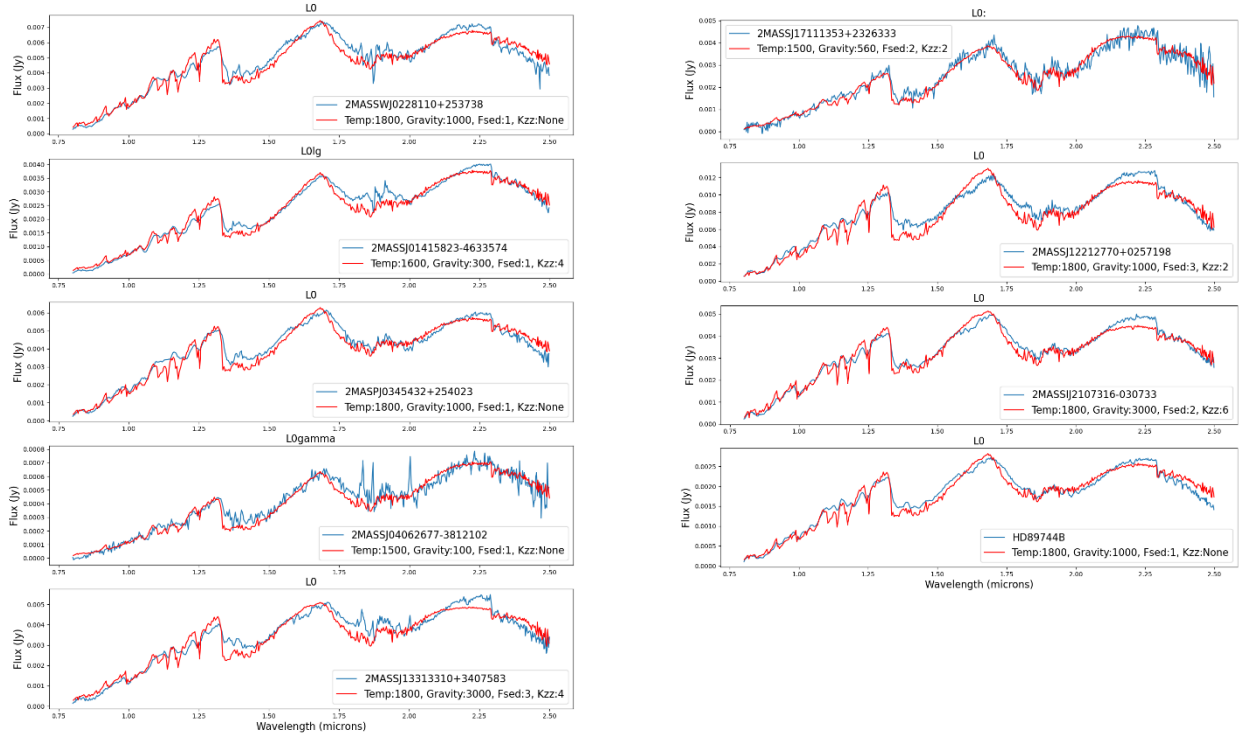

Figure 30: Best-fit models (red) are plotted over the archival spectral data (blue) for all of the objects in my sample of optical-type L0 and L0.5. The object names and best-fit parameters are given in the plot keys.

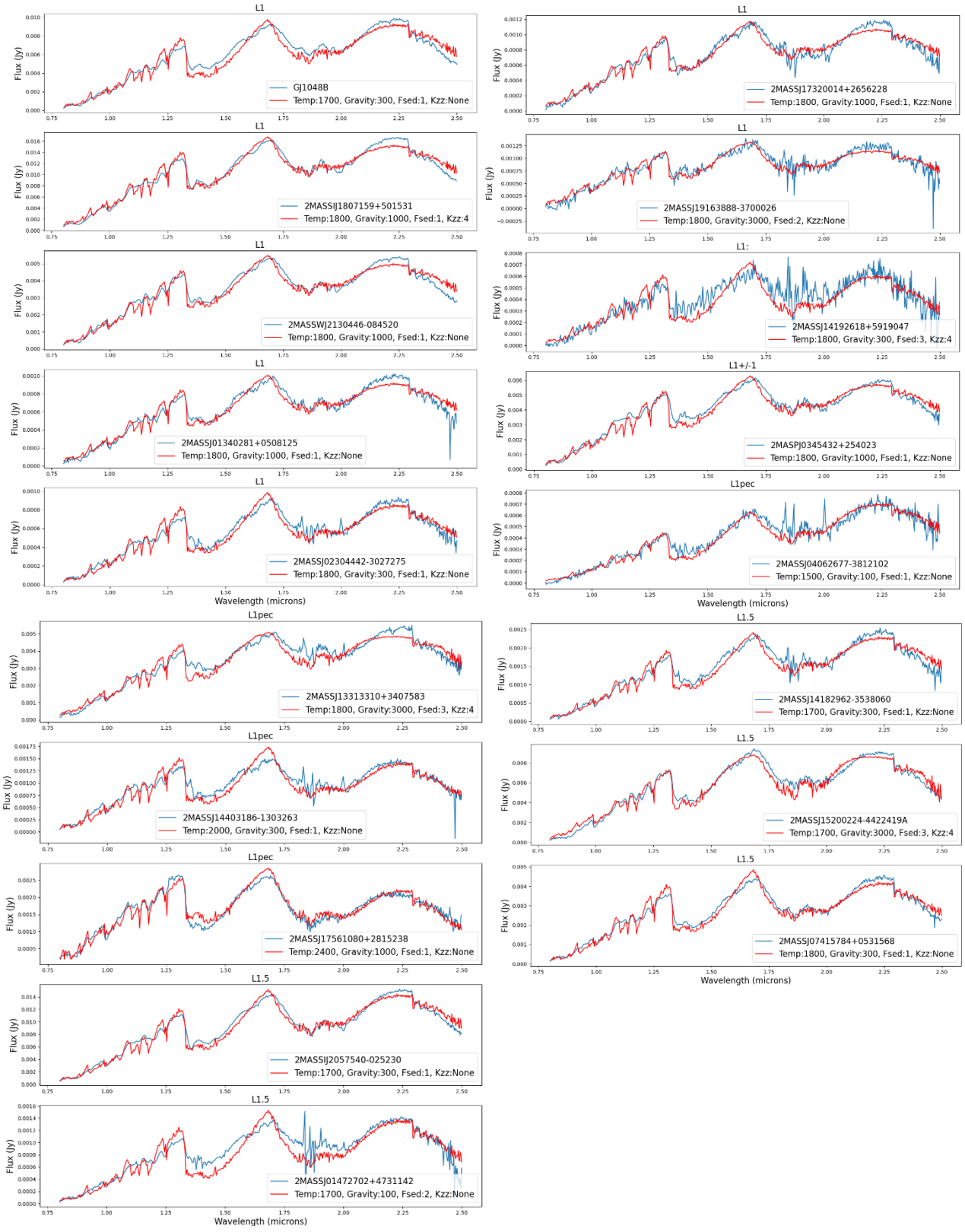

Figure 31: Best-fit models (red) are plotted over the archival spectral data (blue) for all of the objects in my sample of infrared-type L1 and L1.5. The object names and best-fit parameters are given in the plot keys.

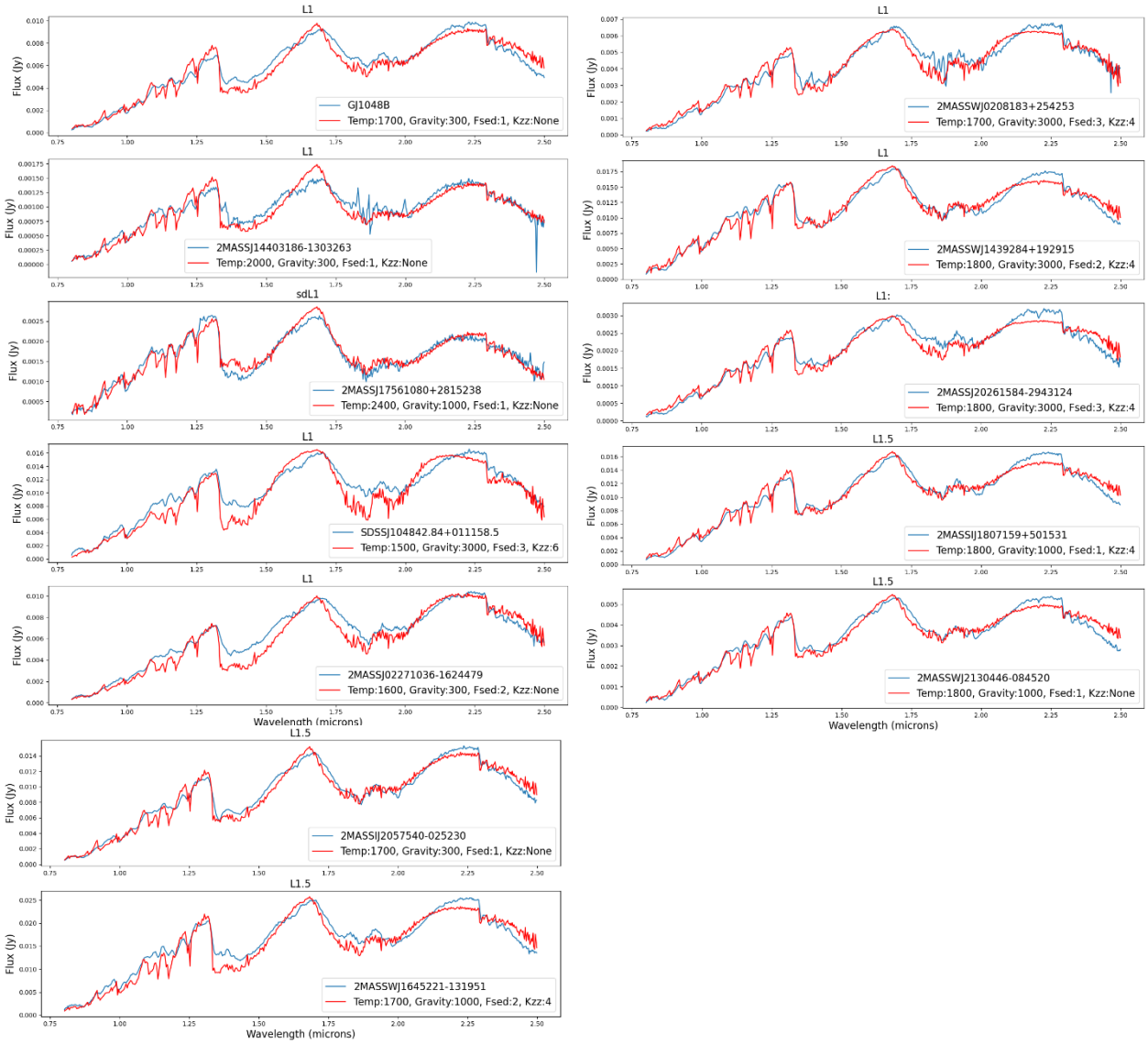

Figure 32: Best-fit models (red) are plotted over the archival spectral data (blue) for all of the objects in my sample of optical-type L1 and L1.5. The object names and best-fit parameters are given in the plot keys.

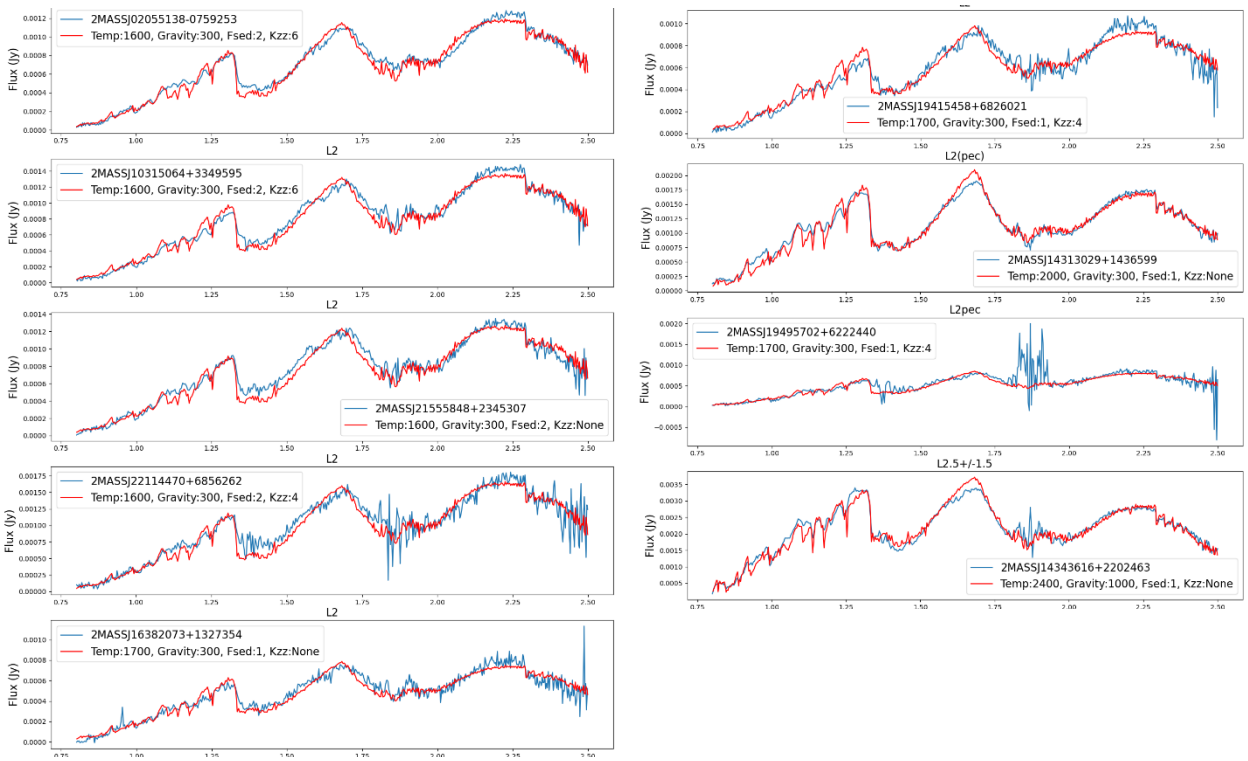

Figure 33: Best-fit models (red) are plotted over the archival spectral data (blue) for all of the objects in my sample of infrared-type L2 and L2.5. The object names and best-fit parameters are given in the plot keys.

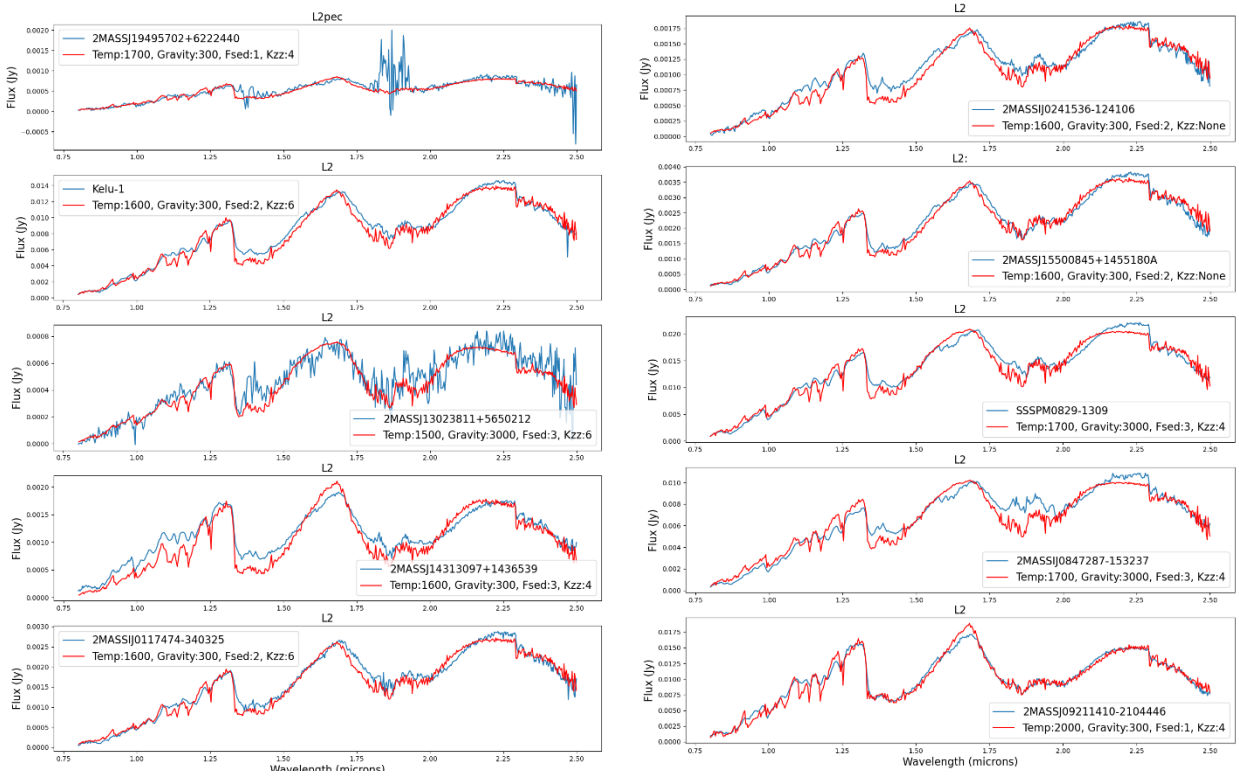

Figure 34: Best-fit models (red) are plotted over the archival spectral data (blue) for all of the objects in my sample of optical-type L2 and L2.5. The object names and best-fit parameters are given in the plot keys.

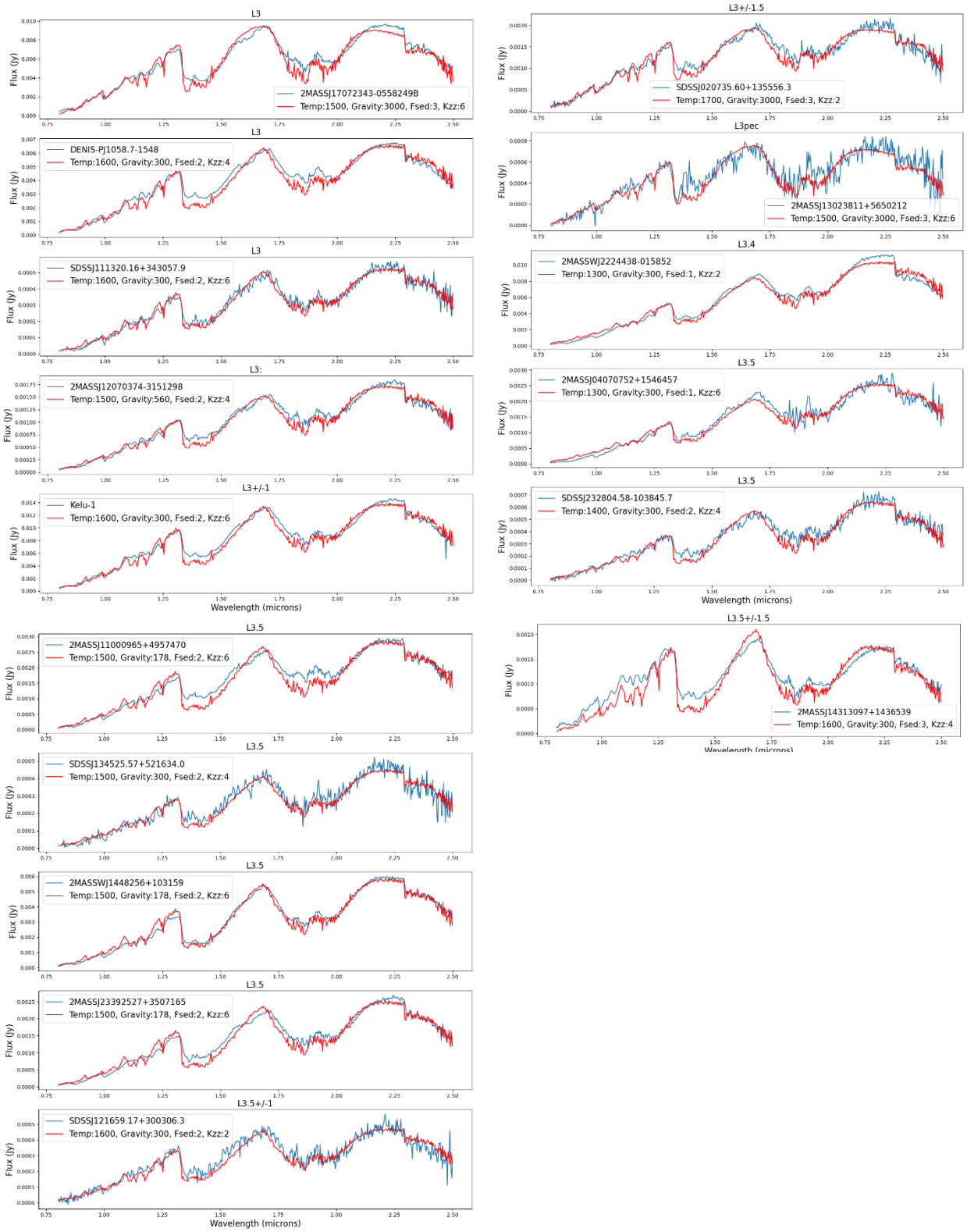

Figure 35: Best-fit models (red) are plotted over the archival spectral data (blue) for all of the objects in my sample of infrared-type L3 and L3.5. The object names and best-fit parameters are given in the plot keys.

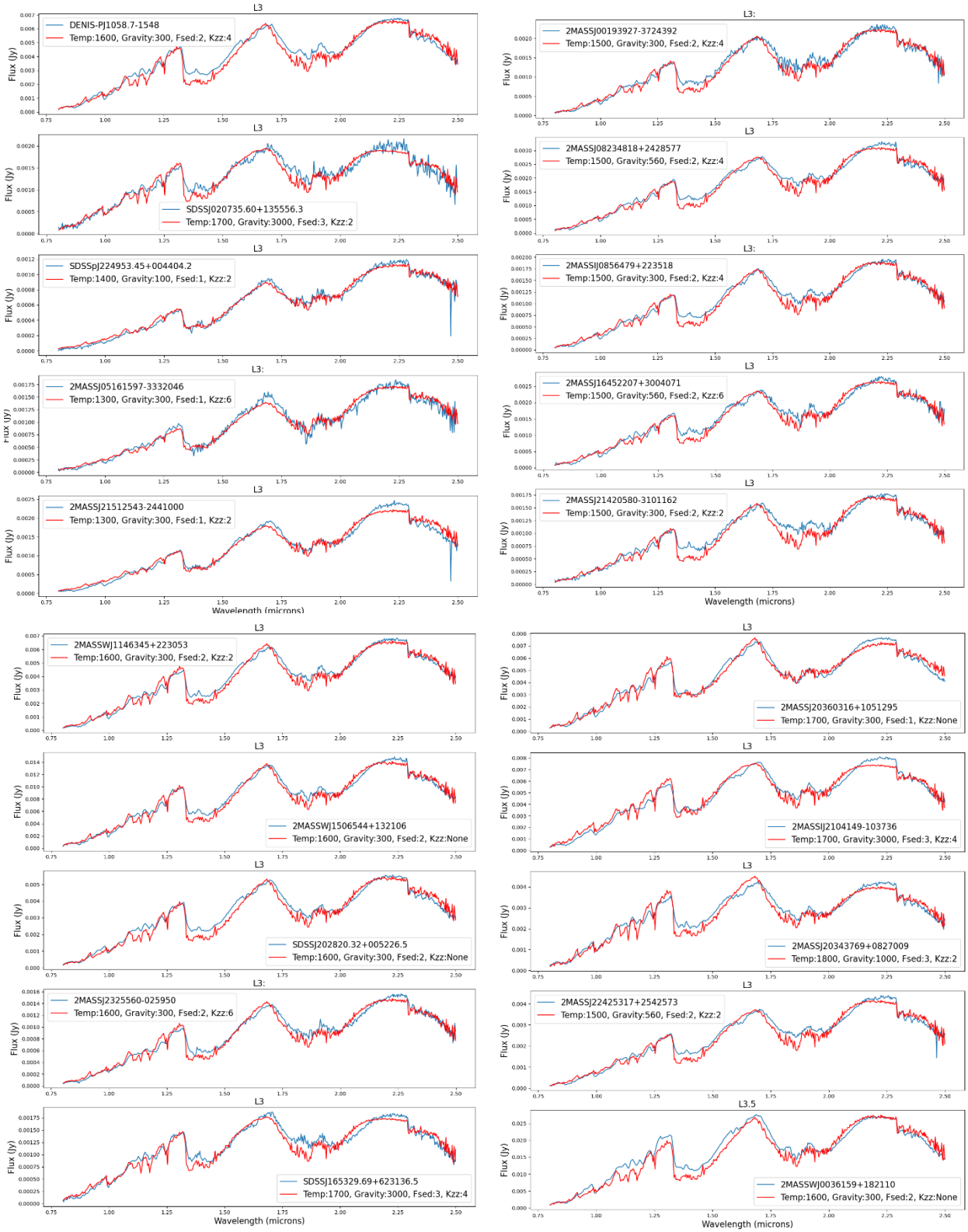

Figure 36: Best-fit models (red) are plotted over the archival spectral data (blue) for all of the objects in my sample of optical-type L3 and L3.5. The object names and best-fit parameters are given in the plot keys.

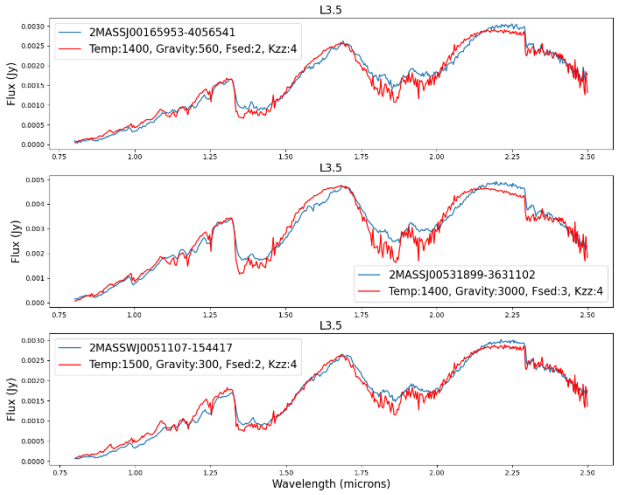

Figure 36: Best-fit models (red) are plotted over the archival spectral data (blue) for all of the objects in my sample of optical-type L3 and L3.5. The object names and best-fit parameters are given in the plot keys.

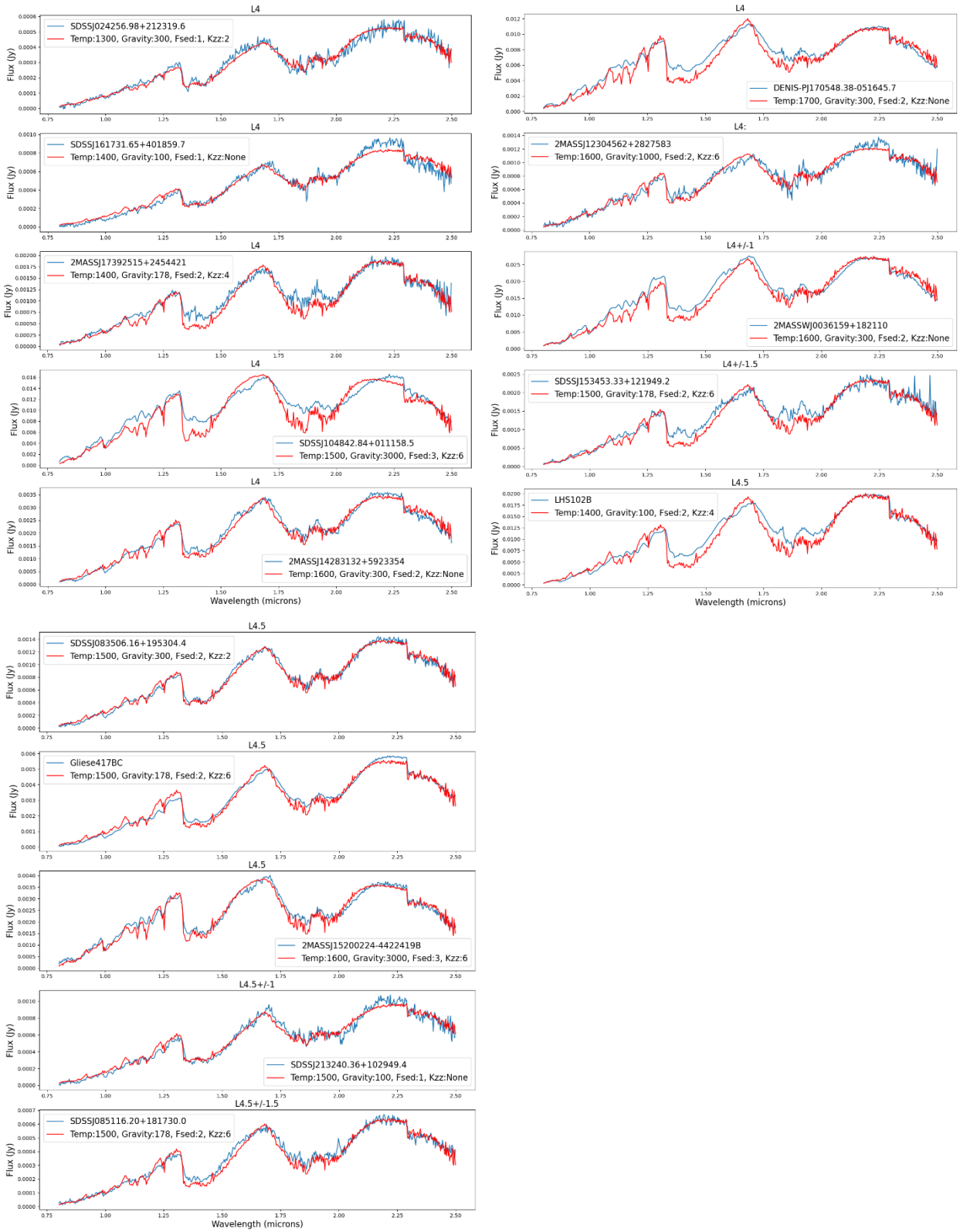

Figure 37: Best-fit models (red) are plotted over the archival spectral data (blue) for all of the objects in my sample of infrared-type L4 and L4.5. The object names and best-fit parameters are given in the plot keys.

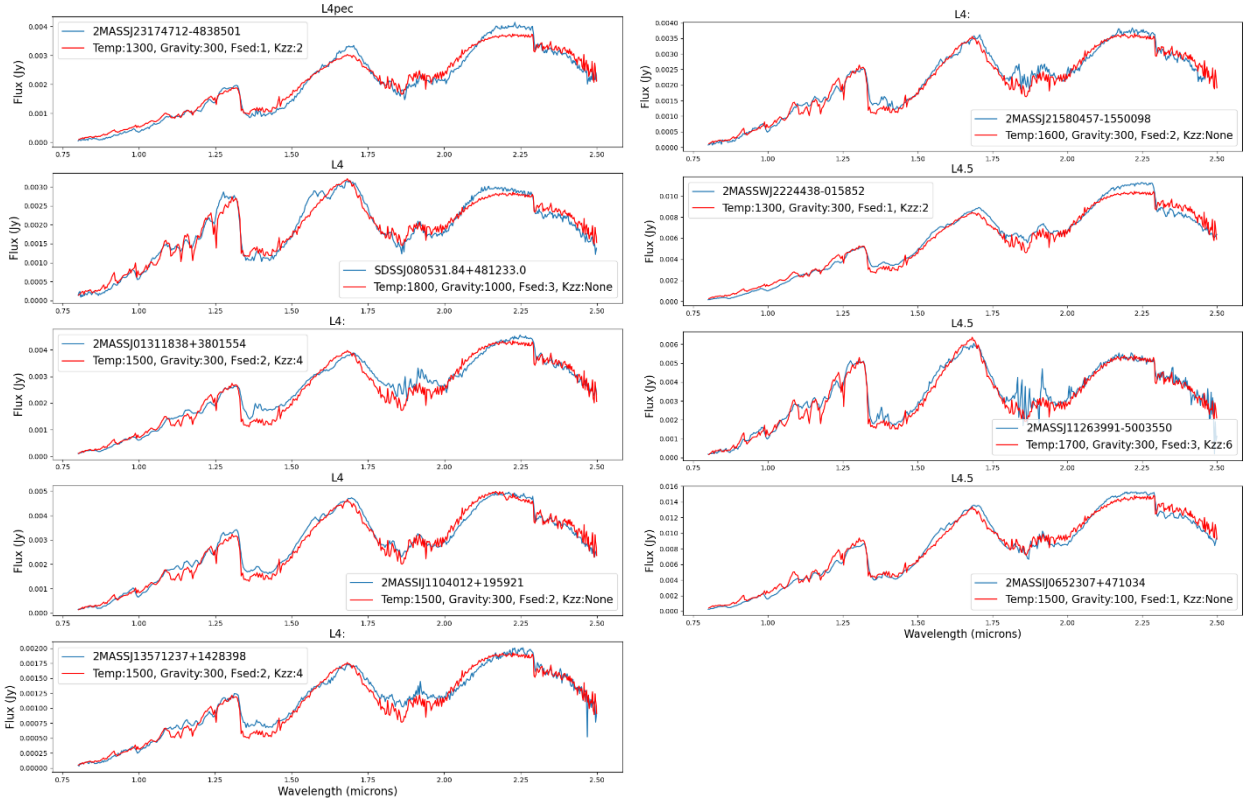

Figure 38: Best-fit models (red) are plotted over the archival spectral data (blue) for all of the objects in my sample of optical-type L4 and L4.5. The object names and best-fit parameters are given in the plot keys.

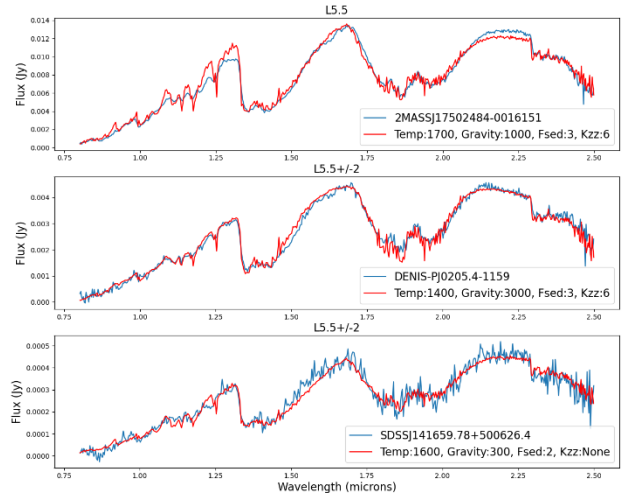

Figure 39: Best-fit models (red) are plotted over the archival spectral data (blue) for all of the objects in my sample of infrared-type L5 and L5.5. The object names and best-fit parameters are given in the plot keys.

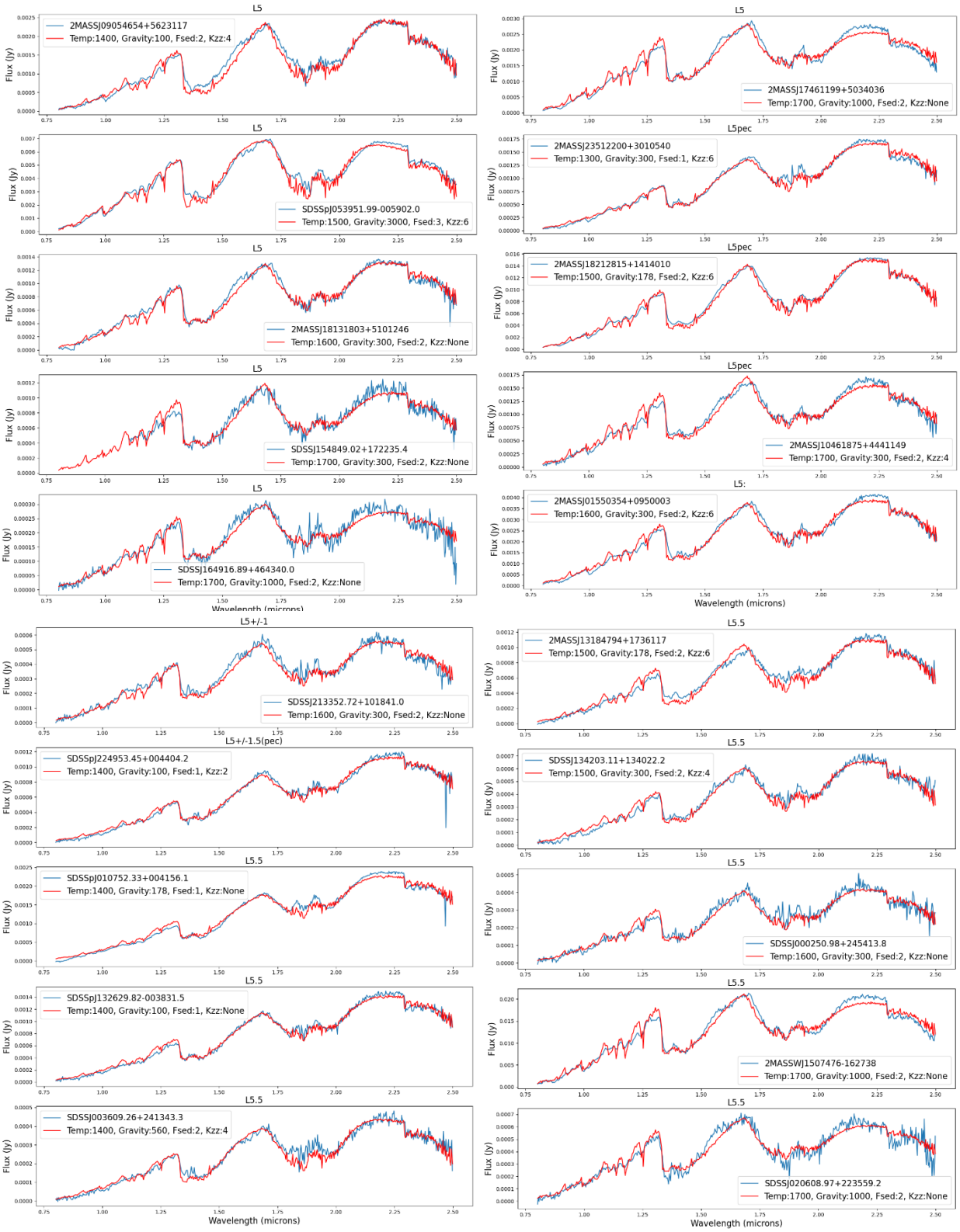

Figure 39: Best-fit models (red) are plotted over the archival spectral data (blue) for all of the objects in my sample of infrared-type L5 and L5.5. The object names and best-fit parameters are given in the plot keys.

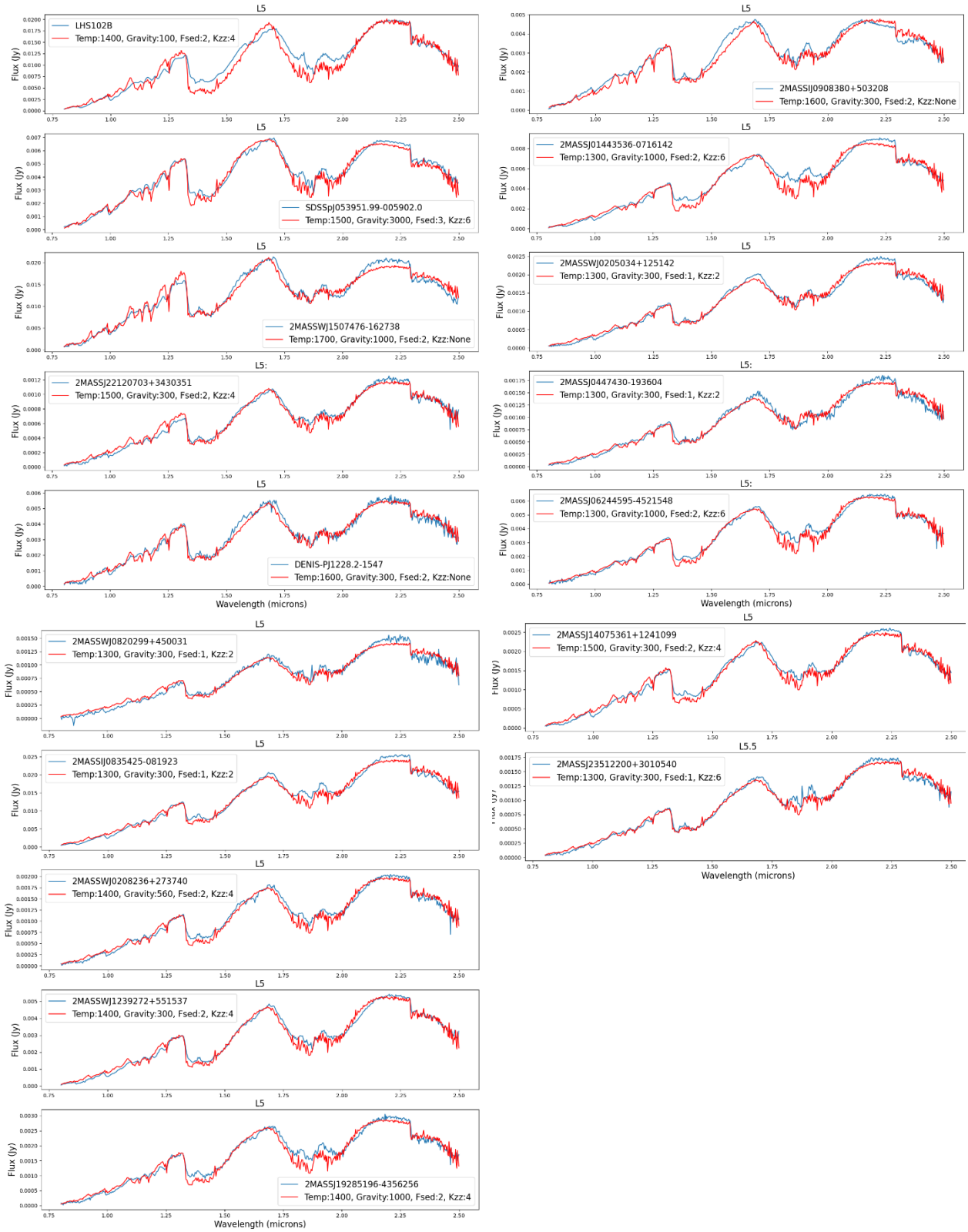

Figure 40: Best-fit models (red) are plotted over the archival spectral data (blue) for all of the objects in my sample of optical-type L5 and L5.5. The object names and best-fit parameters are given in the plot keys.

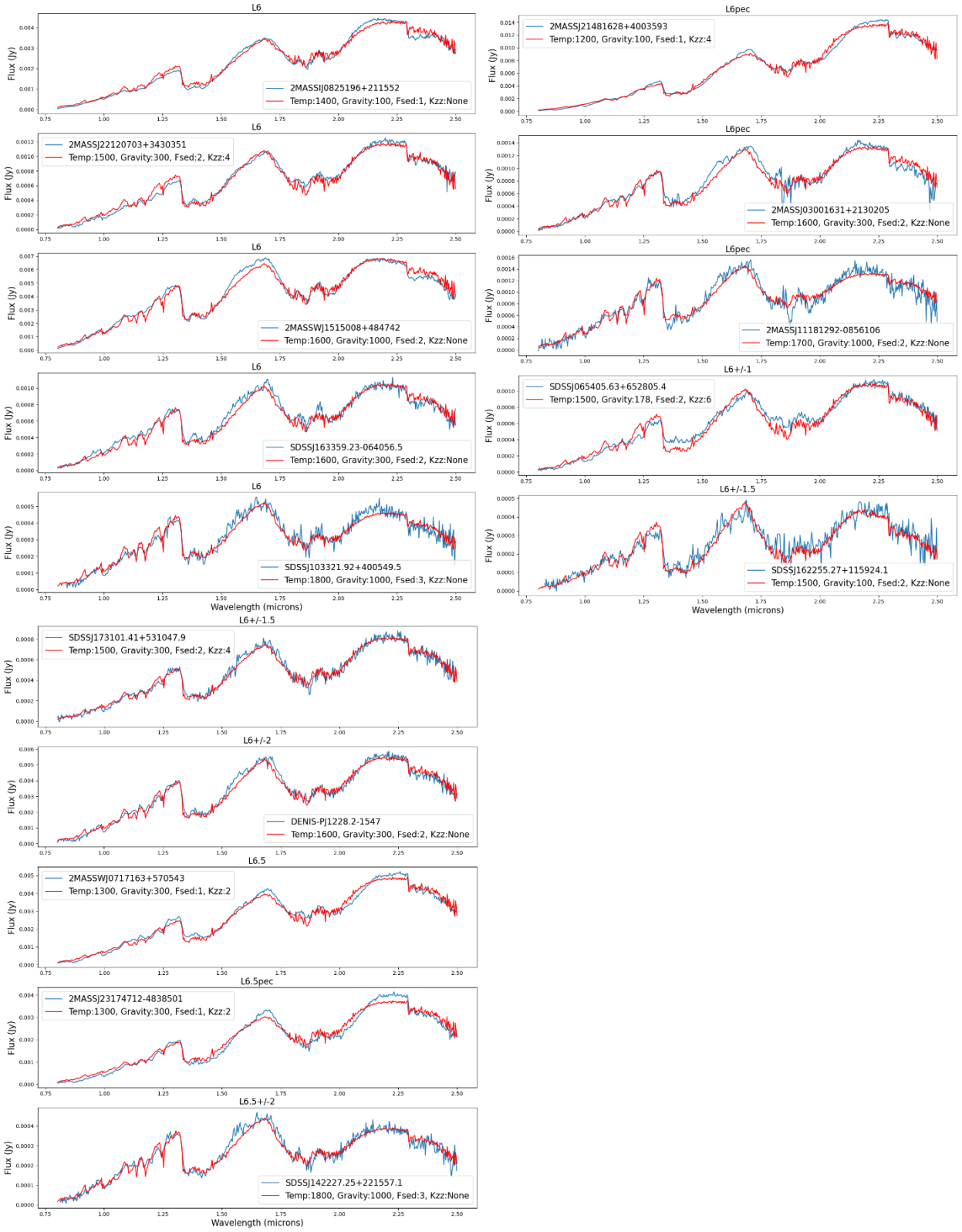

Figure 41: Best-fit models (red) are plotted over the archival spectral data (blue) for all of the objects in my sample of infrared-type L6 and L6.5. The object names and best-fit parameters are given in the plot keys.

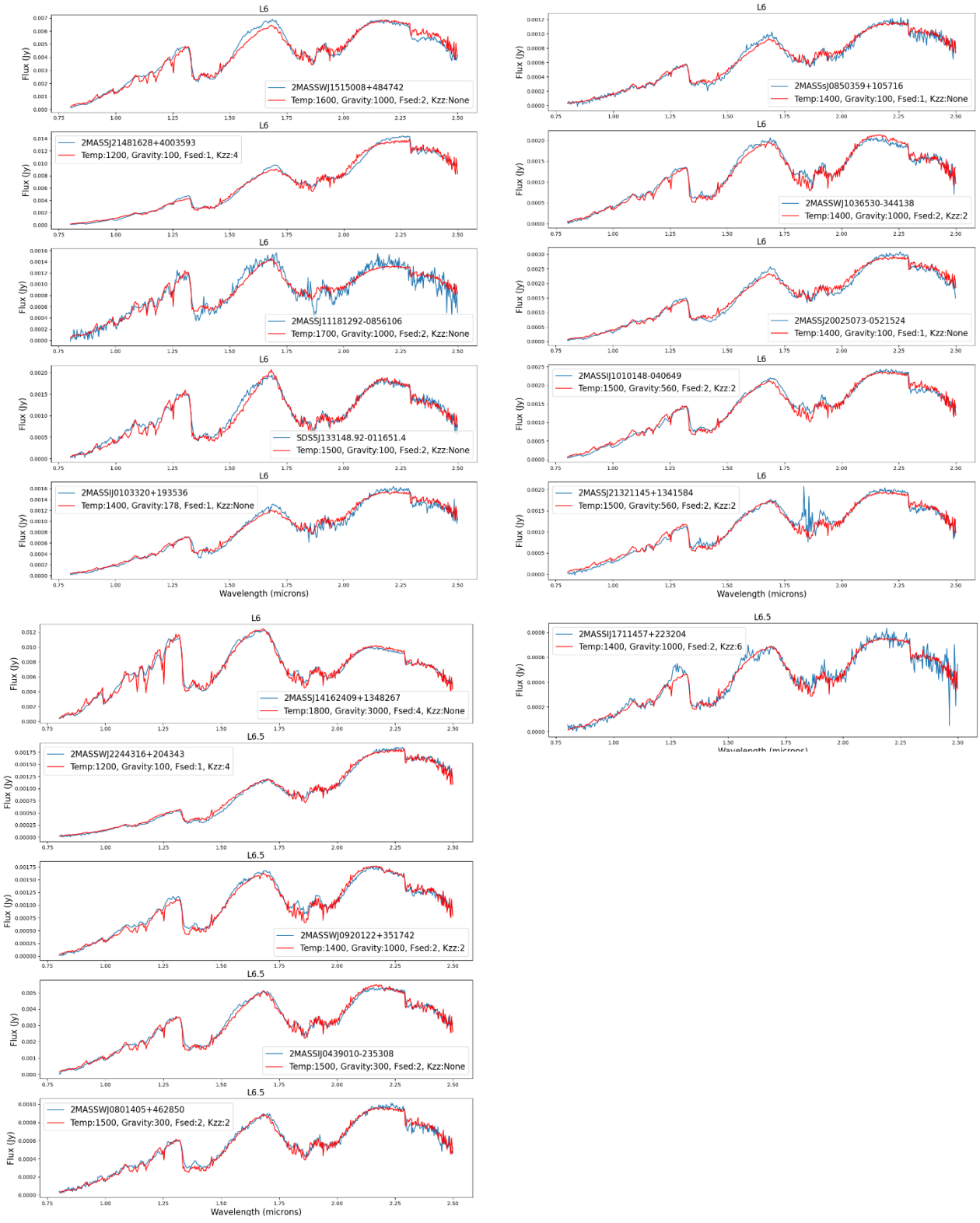

Figure 42: Best-fit models (red) are plotted over the archival spectral data (blue) for all of the objects in my sample of optical-type L6 and L6.5. The object names and best-fit parameters are given in the plot keys.

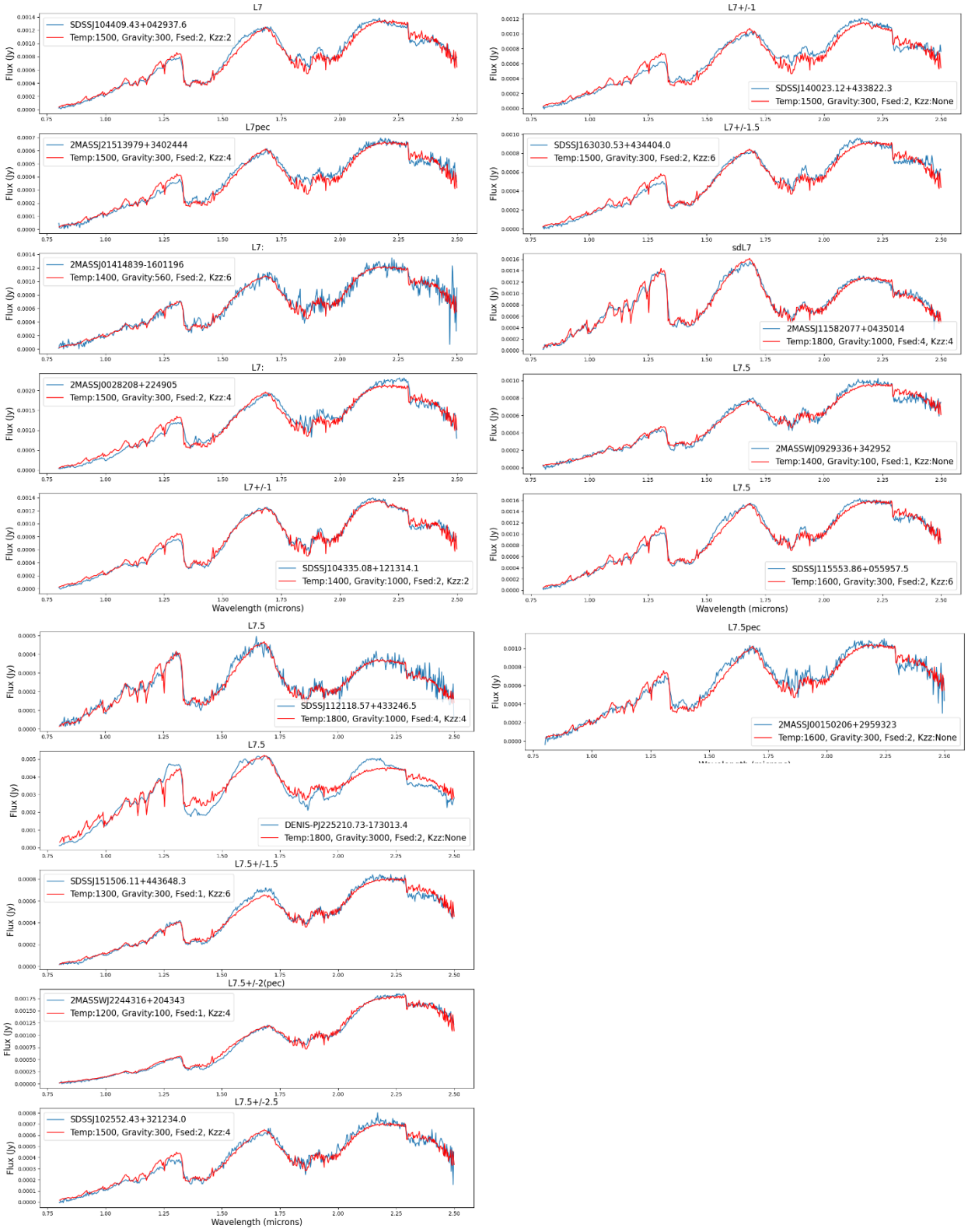

Figure 43: Best-fit models (red) are plotted over the archival spectral data (blue) for all of the objects in my sample of infrared-type L7 and L7.5. The object names and best-fit parameters are given in the plot keys.

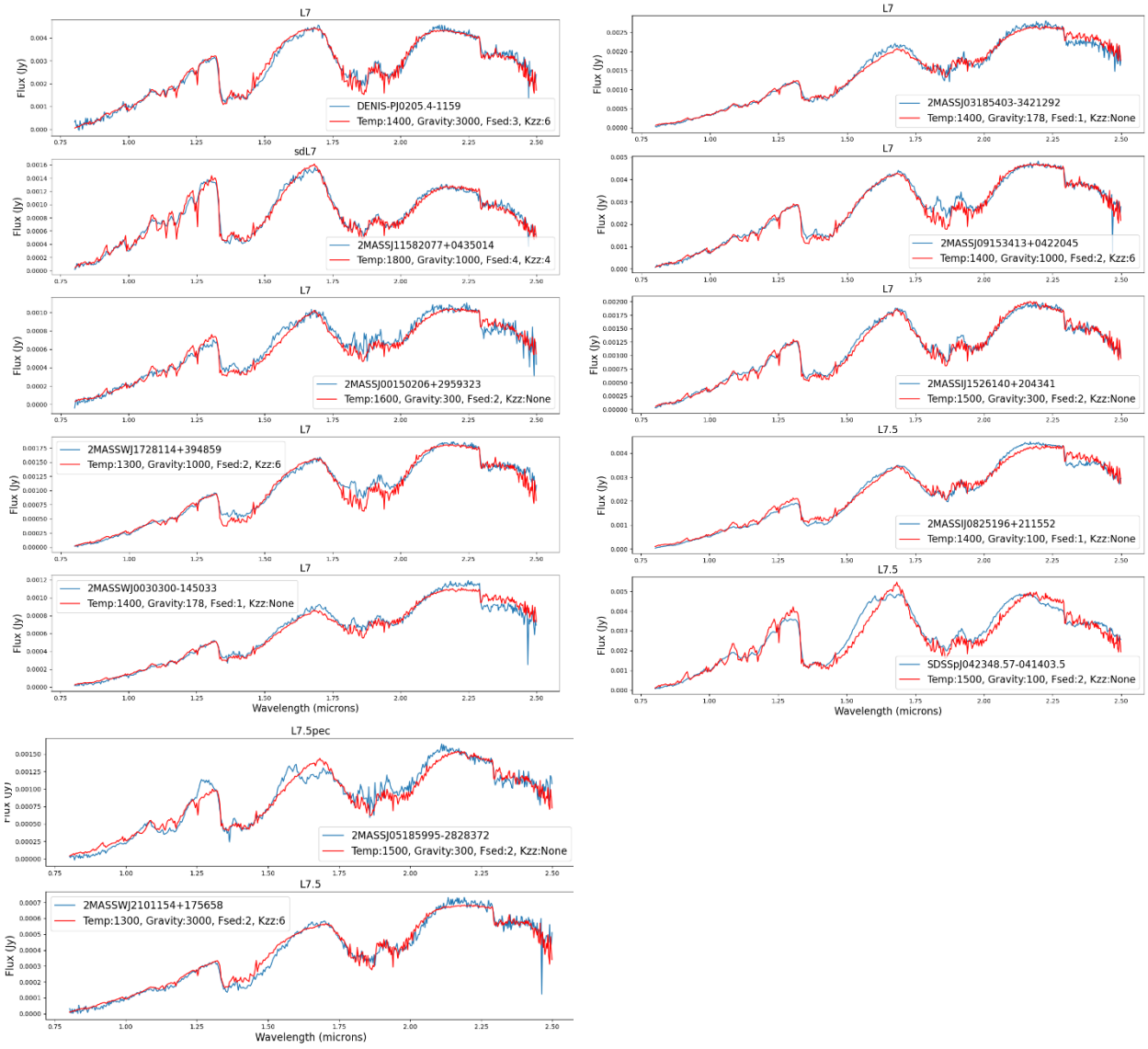

Figure 44: Best-fit models (red) are plotted over the archival spectral data (blue) for all of the objects in my sample of optical-type L7 and L7.5. The object names and best-fit parameters are given in the plot keys.

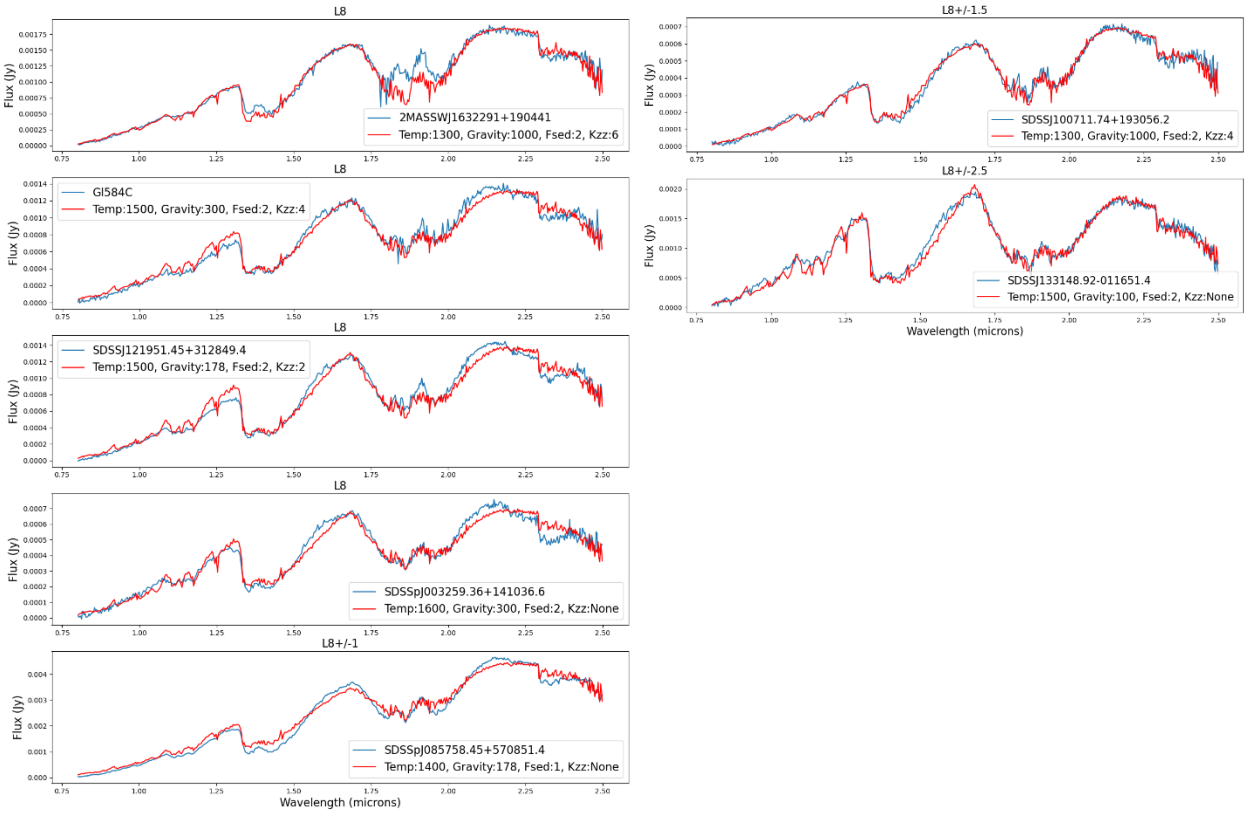

Figure 45: Best-fit models (red) are plotted over the archival spectral data (blue) for all of the objects in my sample of infrared-type L8 and L8.5. The object names and best-fit parameters are given in the plot keys.

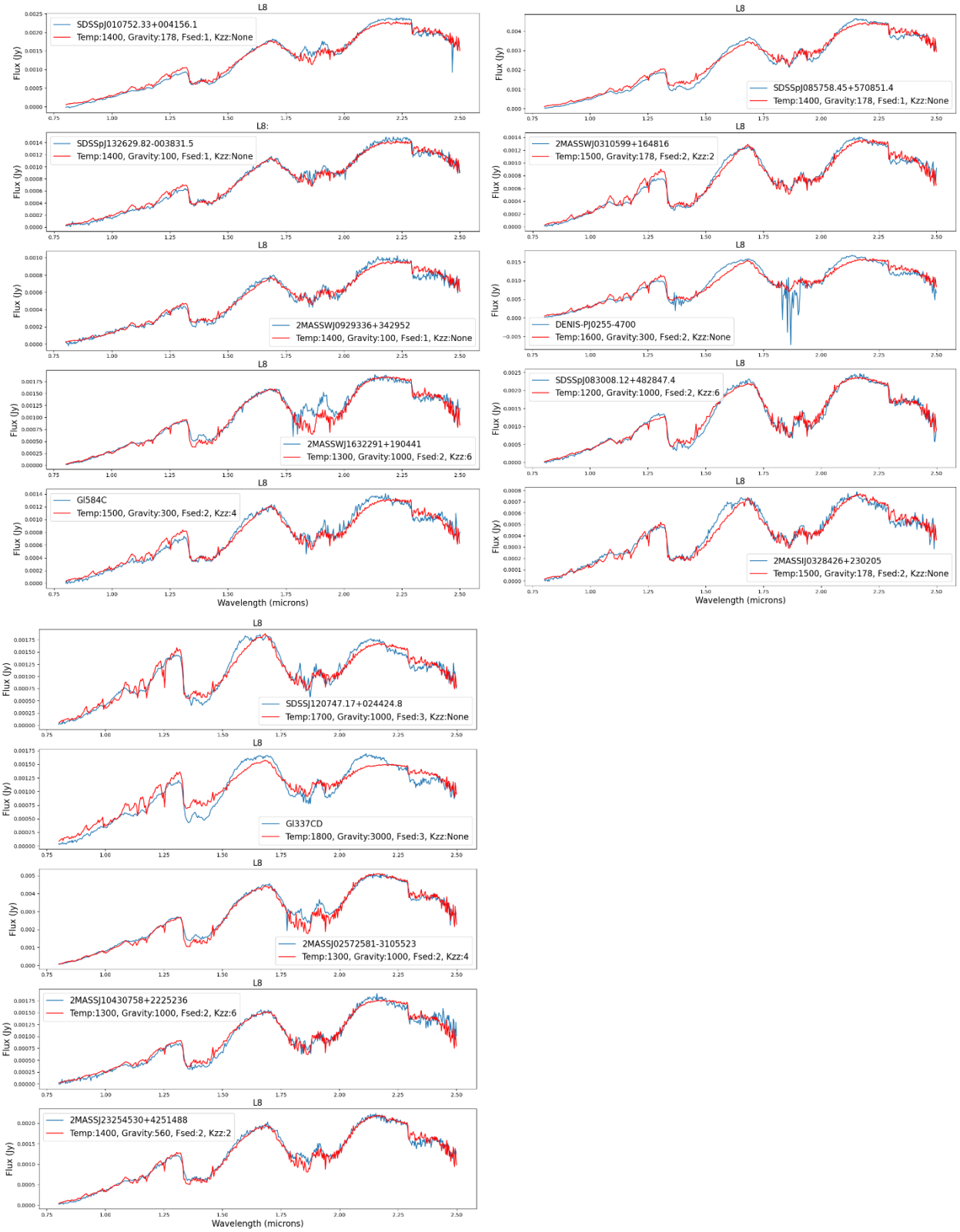

Figure 46: Best-fit models (red) are plotted over the archival spectral data (blue) for all of the objects in my sample of optical-type L8 and L8.5. The object names and best-fit parameters are given in the plot keys.

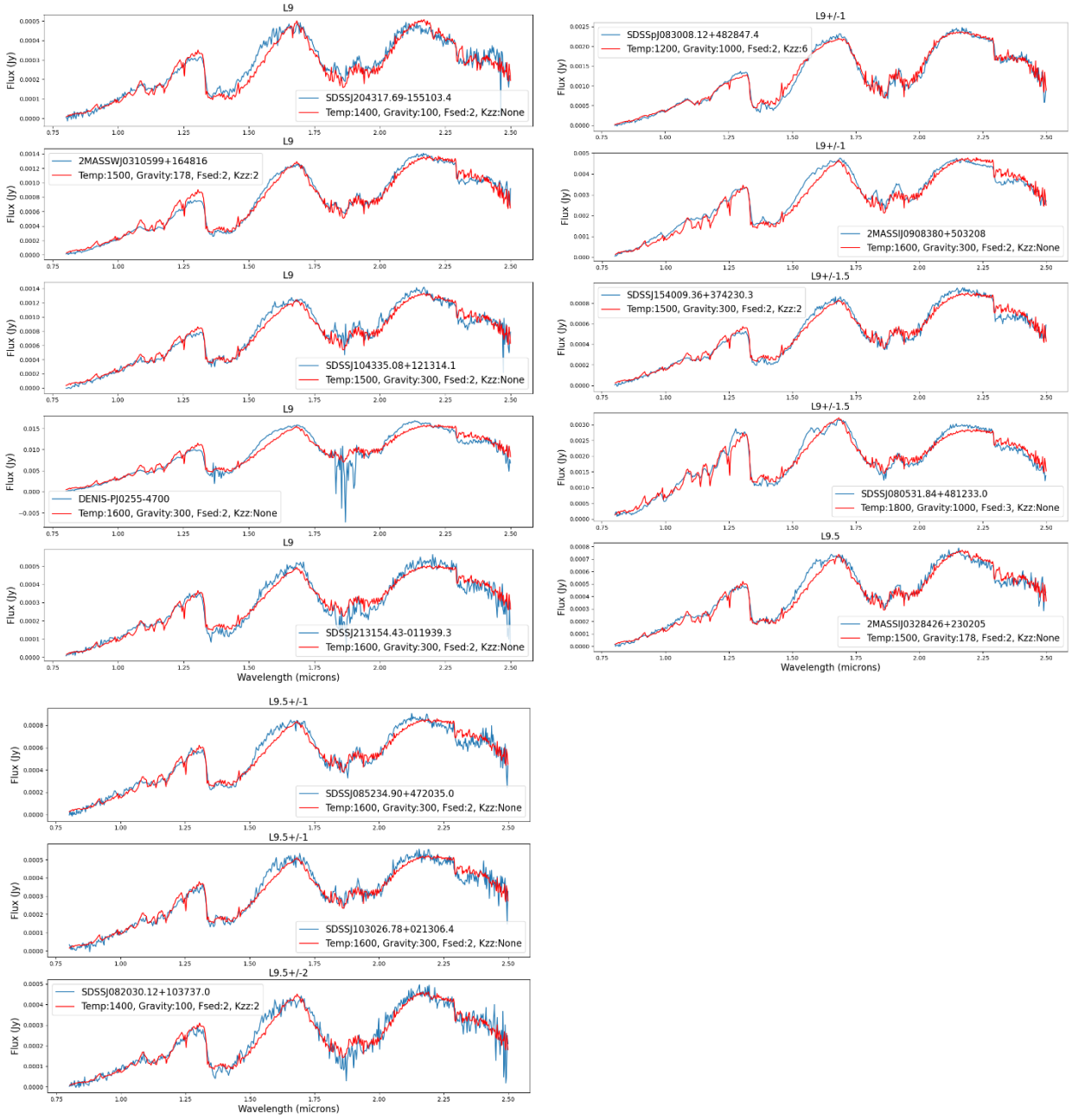

Figure 47: Best-fit models (red) are plotted over the archival spectral data (blue) for all of the objects in my sample of infrared-type L9 and L9.5. The object names and best-fit parameters are given in the plot keys.

8.2 T Types

8.2.1 T0-T3

The plateaued H-bands become even more common for the T0 objects (Figure 48 and Figure 49). The absorption dip at 2.2 μm also is more prevalent for the T0s. Both features are likely due to the appearance of methane. J1511 has a particularly interesting H-band: the top of the band dips in the middle where earlier spectral types had a peak.

The same double-peaked H-band appears in about one third of the T1 objects (Figure 50), and the absorption at 2.2 μm continues to deepen. However, J0858 and J0518 both show double peaks like the other early Ts but have K-bands that look more like L-types since neither object shows much absorption at 2.2 μm. These two objects could be candidates for binarity: if they were each unresolved binary systems containing one L- and one T-type object, this could explain how they can simultaneously show T-like H-bands and L-like K-bands.

The T2 fits are given in Figure 51 and Figure 52. Methane absorption has removed a significant amount of flux from the H-band, causing the J- and H-bands to have nearly the same height. The methane absorption feature at 1.6 μm has become strong enough that the H-band now slopes diagonally to the right. Many of the fits for this spectral type are poor, likely due to the many atmospheric changes taking place in the L/T transition.

Spectral type T3 (Figure 53) is another turning point. Half of the objects fit to S&M models, while half instead fit to bobcat models. Methane appears to have finally become strong enough to be more important to the fits than clouds. The objects that matched with bobcat models (J1206, J1209, J1750, and J1214) are fit beautifully, while the S&M fits are very poor for the J- and H-bands.

8.2.2 T4-T6

The T4-type objects are the best-fit objects in the entire sample (Figure 54 and Figure 55). Nearly all of these objects matched with cloudless bobcat models and are fit almost perfectly. If sulfide clouds have already begun to condense in T4-dwarfs, they do not yet appear to have much of an effect on the spectra. The absorption feature in the J-band around 1.15 μm has begun to deepen noticeably with temperature.

Enough light has been removed from the H-band by methane absorption that it has fallen below the peak height of the J-band for the T5-type objects (Figure 56 and Figure 57). Absorption at 1.15 μm continues to deepen.

The T6-type objects in Figure 58 and Figure 59 are fit poorly at 1.6 μm. The models predict a spike here that overfits the data. This is likely another methane opacity value that needs to be updated. The J- and K-bands are still generally fit very well. The models are well-able to replicate the extreme suppression of the K-band and the near-complete absorption at 1.15 μm.

8.2.3 T7-T8

The mismatch between the data and the models at 1.6 μm is even more apparent for the T7-types (Figure 60 and Figure 61) and the T8-types (Figure 63 and Figure 62). The general shapes of the J- and K- bands are well fit for these types, although the models underfit the peaks of these bands for almost every object. Comparison of the fits of these objects to the plots from Morley et al. [36] shown in Figure 16 suggests that the models could be suppressed due to sulfide clouds: perhaps the objects that are underfit have thinner clouds than Morley predicts.

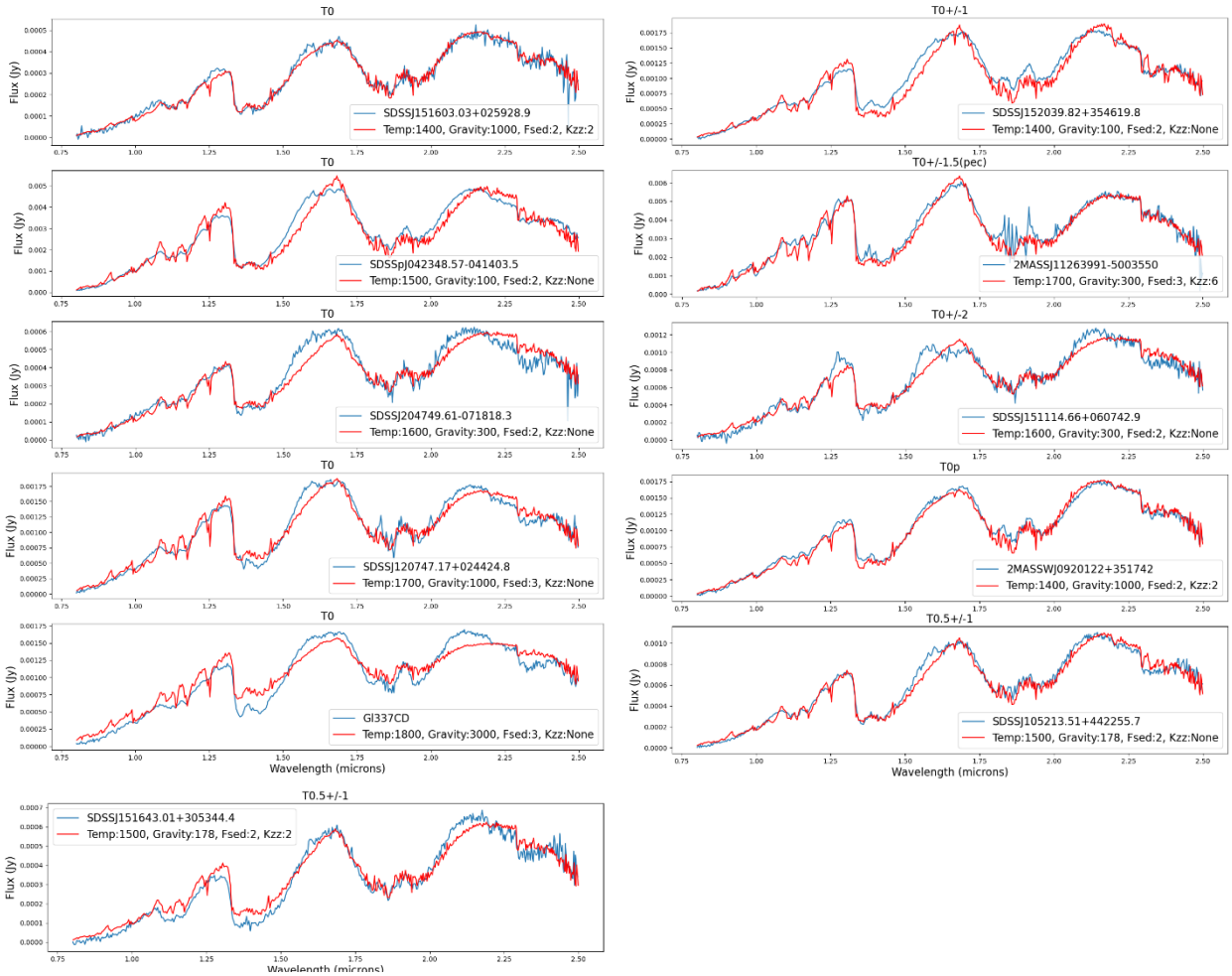

Figure 48: Best-fit models (red) are plotted over the archival spectral data (blue) for all of the objects in my sample of infrared-type T0 and T0.5. The object names and best-fit parameters are given in the plot keys.

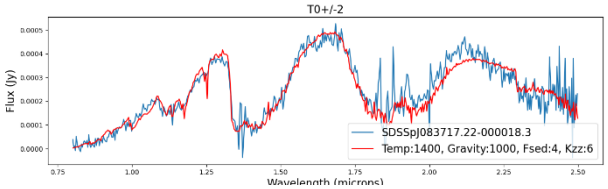

Figure 49: This was the only archival object assigned an optical type of T0. The data is given in blue, while the best-fit model is shown in red.

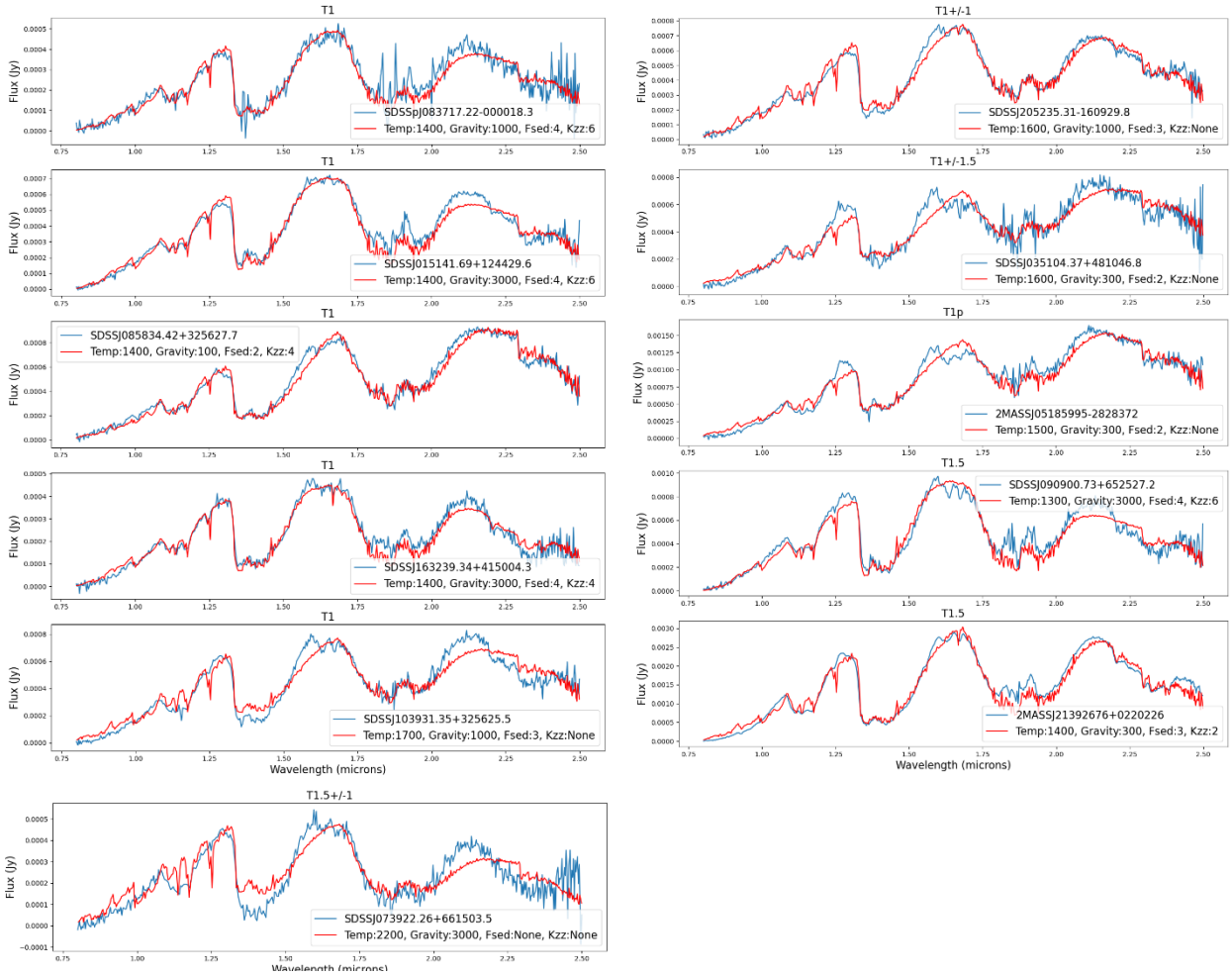

Figure 50: Best-fit models (red) are plotted over the archival spectral data (blue) for all of the objects in my sample of infrared-type T1 and T1.5. The object names and best-fit parameters are given in the plot keys.

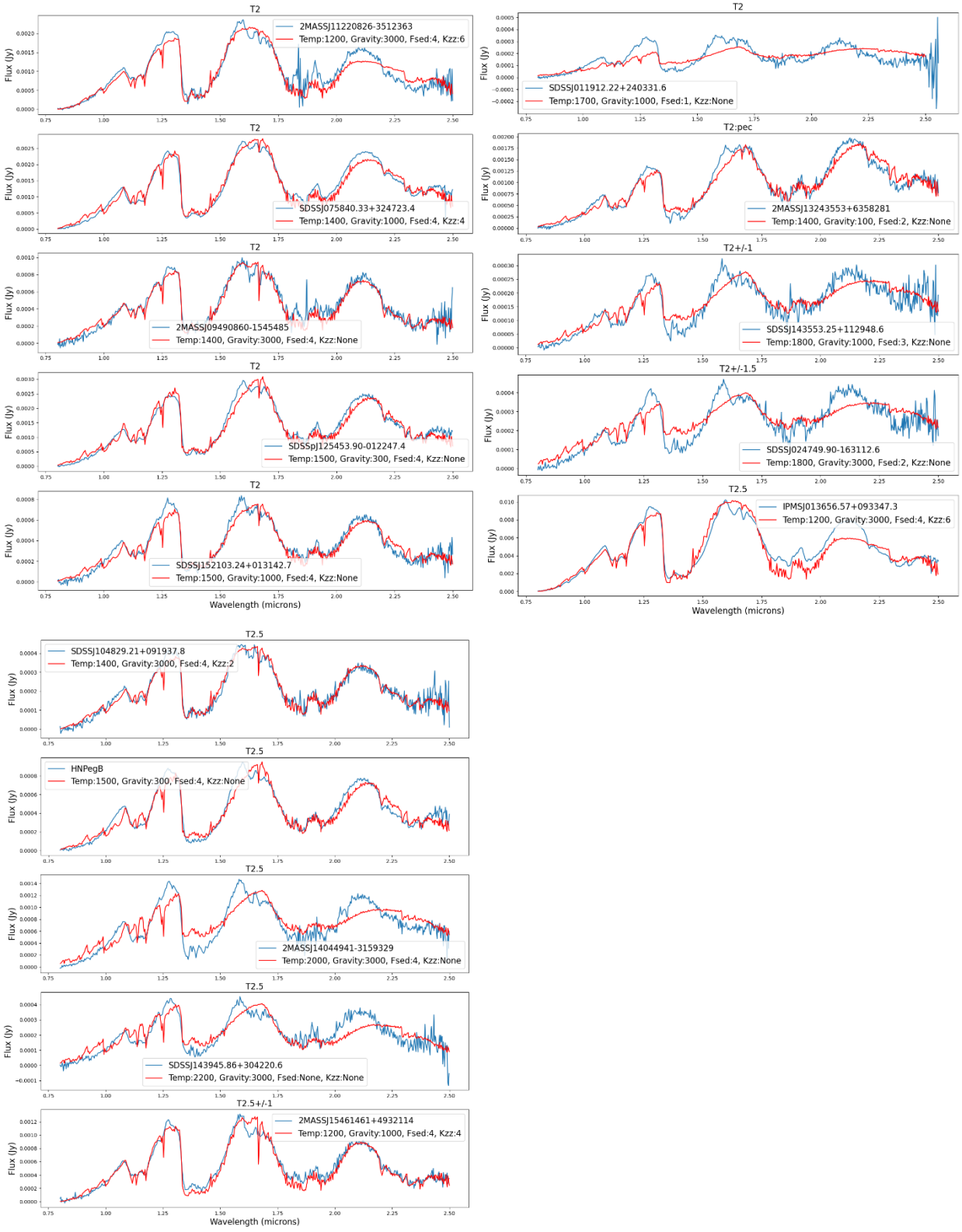

Figure 51: Best-fit models (red) are plotted over the archival spectral data (blue) for all of the objects in my sample of infrared-type T2 and T2.5. The object names and best-fit parameters are given in the plot keys.

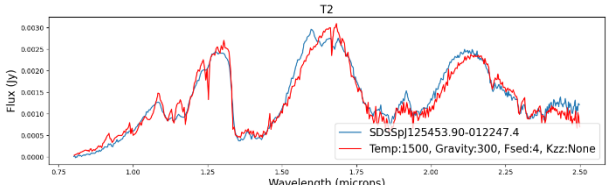

Figure 52: This was the only archival object assigned an optical type of T2. The data is given in blue, while the best-fit model is shown in red.

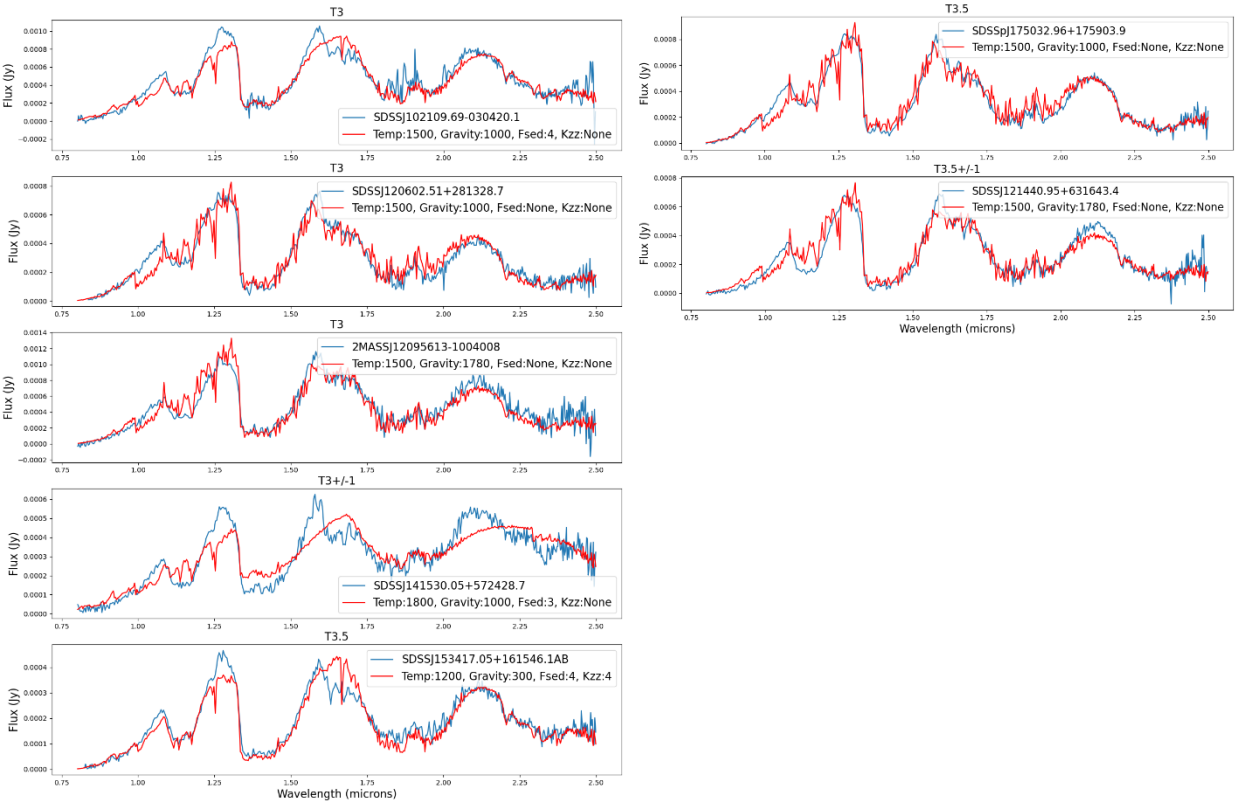

Figure 53: Best-fit models (red) are plotted over the archival spectral data (blue) for all of the objects in my sample of infrared-type T3 and T3.5. The object names and best-fit parameters are given in the plot keys.

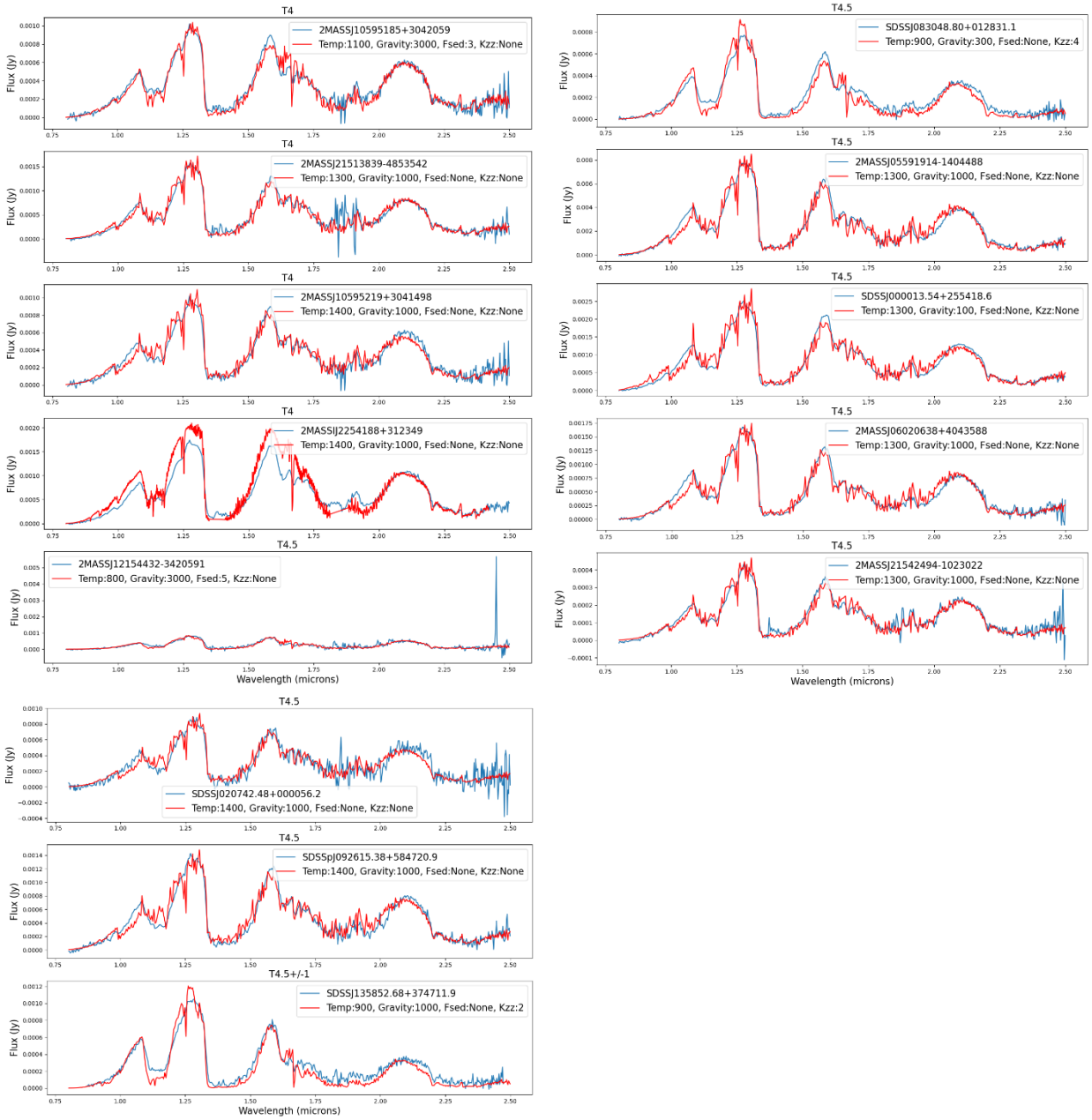

Figure 54: Best-fit models (red) are plotted over the archival spectral data (blue) for all of the objects in my sample of infrared-type T4 and T4.5. The object names and best-fit parameters are given in the plot keys.

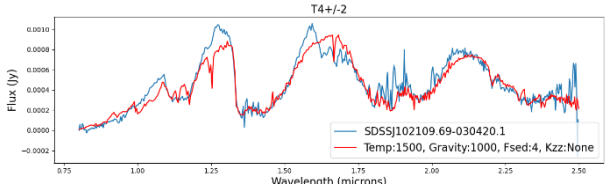

Figure 55: This was the only archival object assigned an optical type of T4. The data is given in blue, while the best-fit model is shown in red.

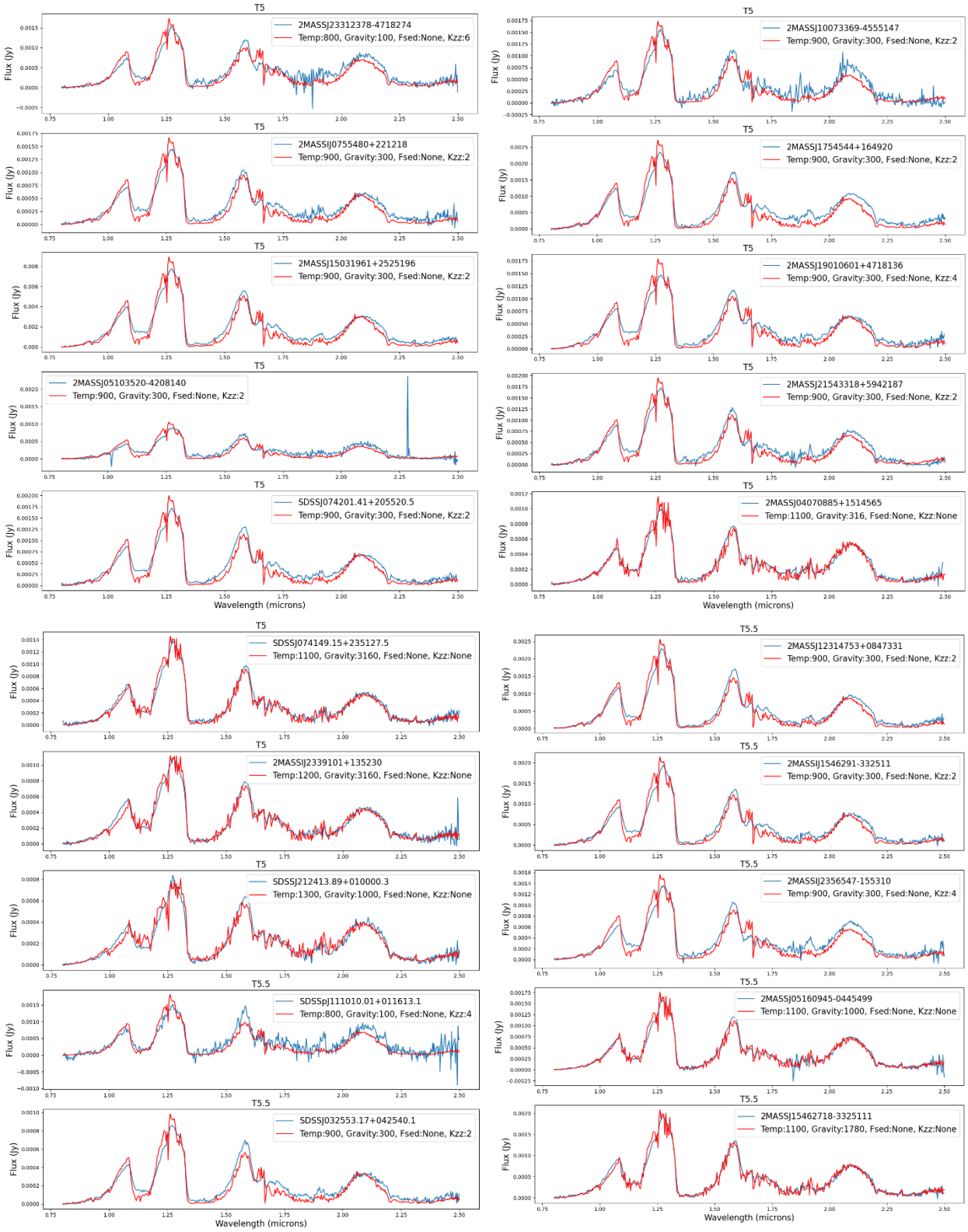

Figure 56: Best-fit models (red) are plotted over the archival spectral data (blue) for all of the objects in my sample of infrared-type T5 and T5.5. The object names and best-fit parameters are given in the plot keys.

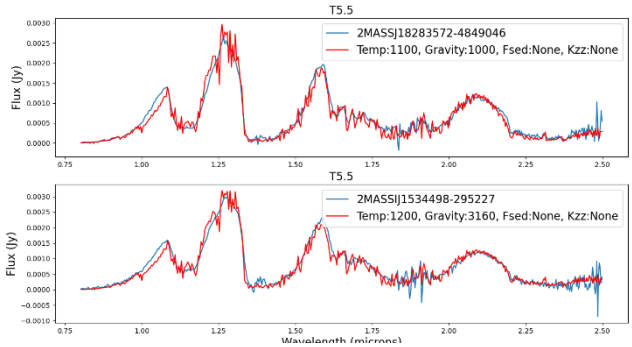

Figure 56: Best-fit models (red) are plotted over the archival spectral data (blue) for all of the objects in my sample of infrared-type T5 and T5.5. The object names and best-fit parameters are given in the plot keys.

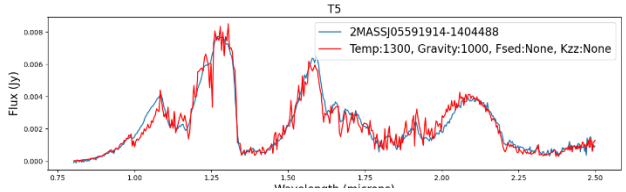

Figure 57: This was the only archival object assigned an optical type of T5. The data is given in blue, while the best-fit model is shown in red.

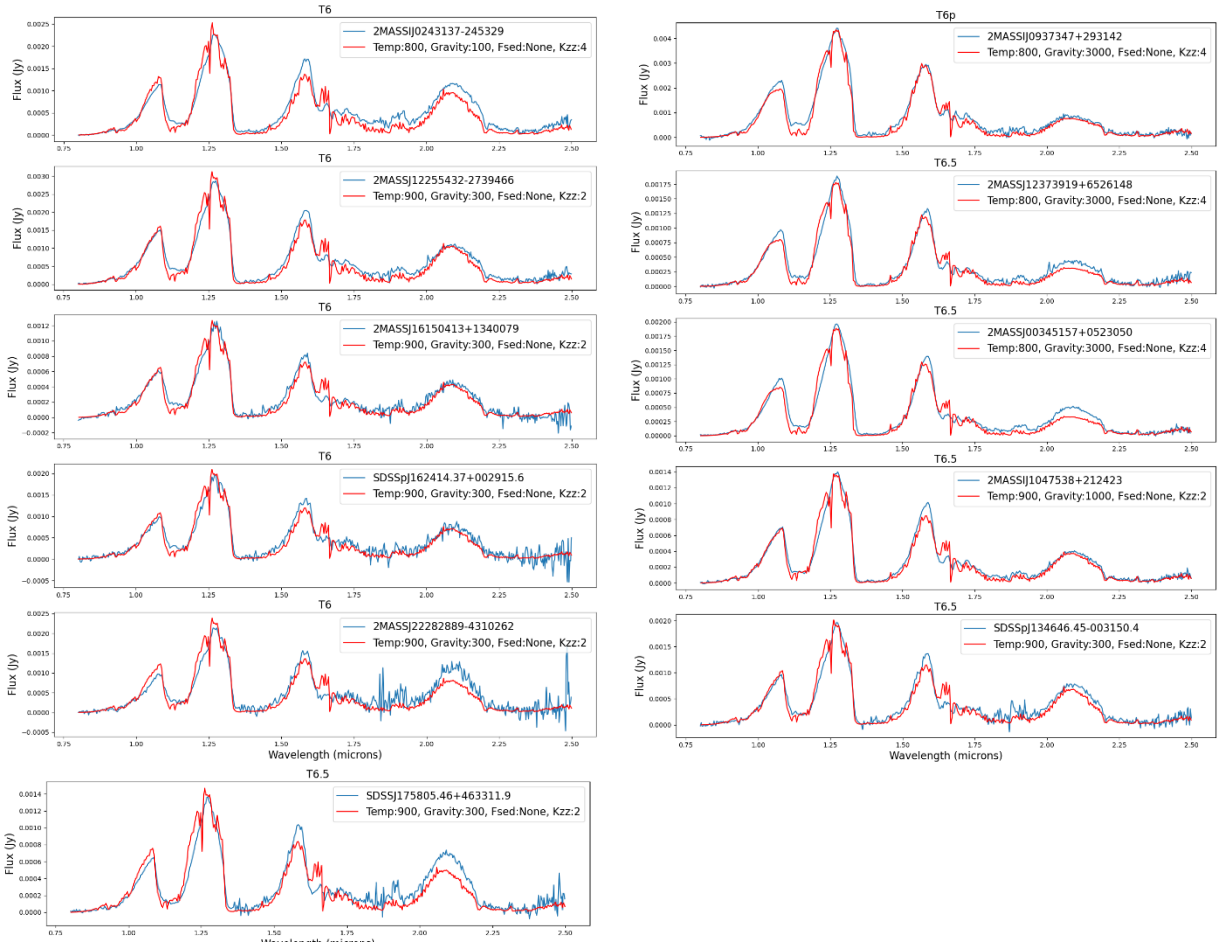

Figure 58: Best-fit models (red) are plotted over the archival spectral data (blue) for all of the objects in my sample of infrared-type T6 and T6.5. The object names and best-fit parameters are given in the plot keys.

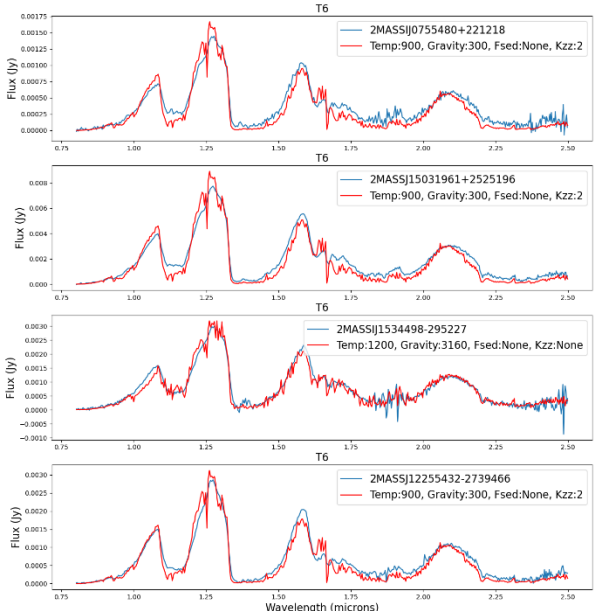

Figure 59: Best-fit models (red) are plotted over the archival spectral data (blue) for all of the objects in my sample of optical-type T6 and T6.5. The object names and best-fit parameters are given in the plot keys.

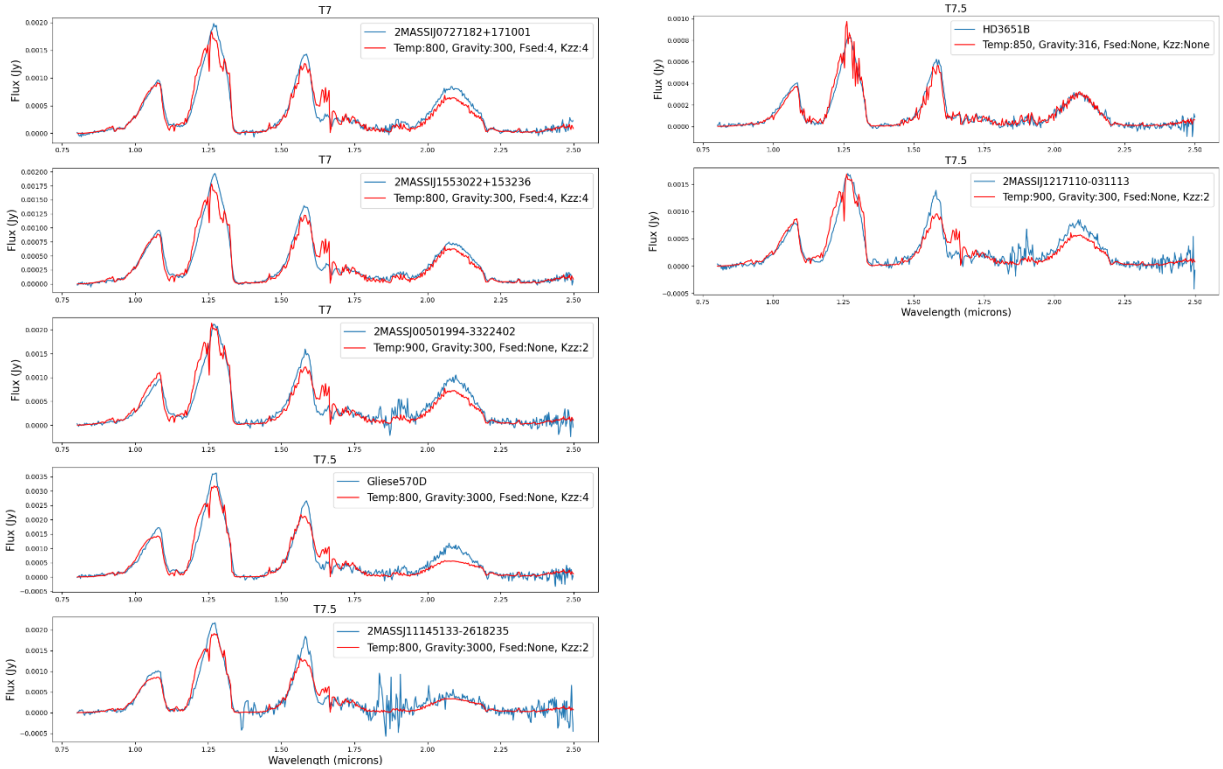

Figure 60: Best-fit models (red) are plotted over the archival spectral data (blue) for all of the objects in my sample of infrared-type T7 and T7.5. The object names and best-fit parameters are given in the plot keys.

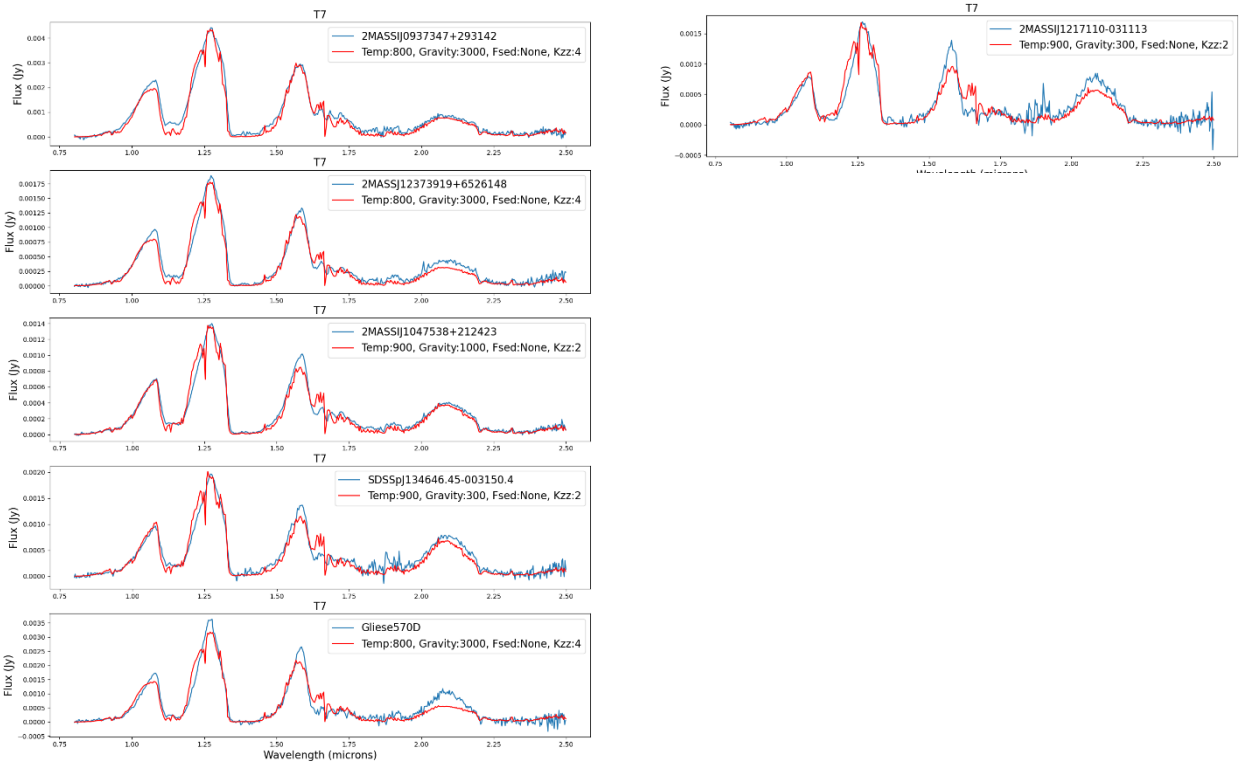

Figure 61: Best-fit models (red) are plotted over the archival spectral data (blue) for all of the objects in my sample of optical-type T7 and T7.5. The object names and best-fit parameters are given in the plot keys.

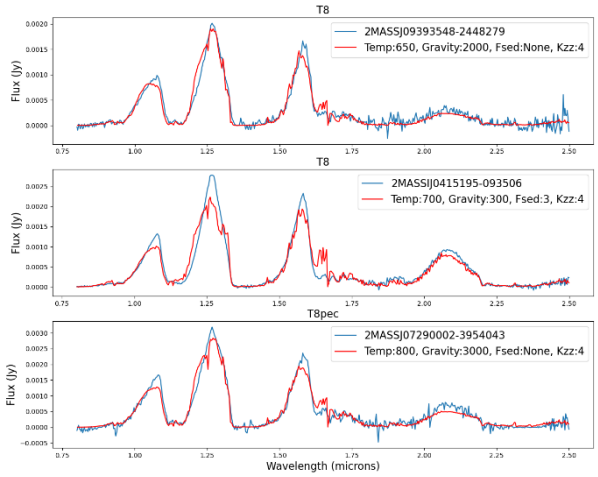

Figure 63: Best-fit models (red) are plotted over the archival spectral data (blue) for all of the objects in my sample of infrared-type T8 and T8.5. The object names and best-fit parameters are given in the plot keys.

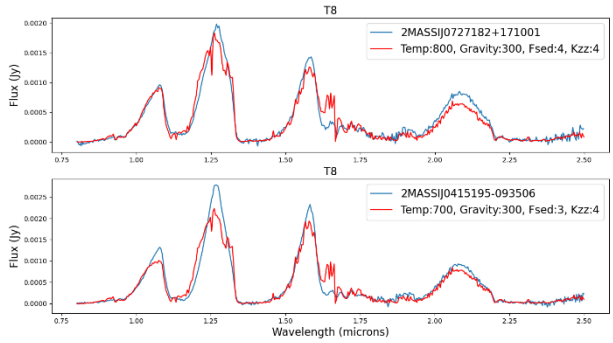

Figure 62: Best-fit models (red) are plotted over the archival spectral data (blue) for all of the objects in my sample of optical-type T8. The object names and best-fit parameters are given in the plot keys.

8.3 TRIPLESPEC Data

The 16 objects observed with TRIPLESPEC were chosen because they had J-K colors that placed them in Best's gap. Conner Scoresby presents a detailed analysis of the spectra of all 16 objects in his senior thesis [61]. I refer readers to his paper for an in-depth literature review and thorough discussion of the real model (RM) single and binary fitting results for each target. I acknowledge that Conner was the Primary Investigator (PI) on the TRIPLESCPEC proposals, selected the targets, and performed all of the data reduction. I will mainly highlight the

theoretical model (SM) fit results for the 16 objects here, focusing on features that are more relevant to this project, and leave the rest of the analysis to Conner.

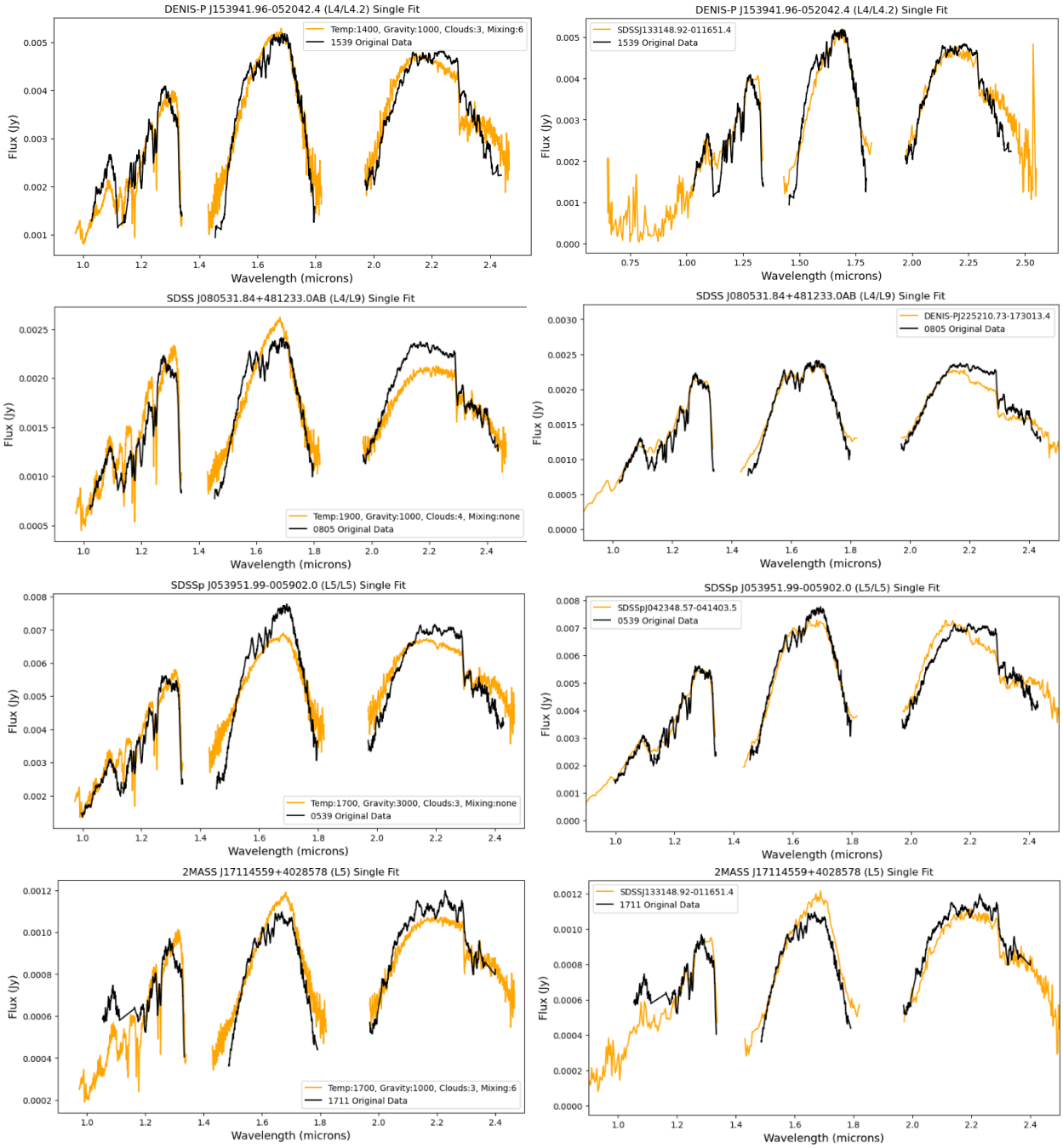

Figure 64: Model-fitting results for the L4-L5 type objects observed with TRIPLESPEC. Black curves correspond to the data, while orange curves correspond to either the theoretical model (SM) fits or the real model (RM) fits. SM fits are on the left, and RM fits are on the right. The legend of each plot gives either the parameters of the best-fit SM model or the object name of the RM model. The wavelength regimes in-between the J, H, and K bands have been masked over due to atmospheric absorption.

8.3.1 L4-L5

The fits of the four L4 and L5 TRIPLESPEC objects are shown in Figure 64. All four objects are underfit by the theoretical models in the K-band to varying degrees, like many of the L-type archival objects. The SM models struggle to fit the H-band peak for all of the objects except for J1539. The H-band peaks are reminiscent of the plateau features observed in some of the late L-types or double-peaks seen in a few of the early T-types. These H-band features are rare in the archival data for spectral types L4 and L5, however, suggesting that perhaps the spectral typing taken from the literature for the TRIPLESPEC objects is off by a type or two. Unlike most of the archival objects, all four TRIPLESPEC objects show a truncation in the J-band peak that is not represented in any of the SM model fits.

J0805 is interesting- this object also had an archival SpeX spectrum that was discussed in the last section of this paper. I previously flagged the archival fit for this object because of its double-peaked H band. Both the archival spectrum and new TRIPLESPEC spectrum show this double-peak as well as the J-band truncation, showing that these are real features and not simply reduction errors. Further inspection of the archival fits that were flagged for double-peaks or plateaued H-bands reveals that others in this group demonstrate similar J-band truncations. For example, the RM fits for J0805 and J0539 both matched to archival objects showing truncated J-bands (J2252 and J0423).

There appears to be a link between the truncated J-bands and plateaued or double-peaked H-bands. The archival fits of the previous section show that these features are fairly rare, but pop up often enough in the mid-to-late Ts and early Ls that further investigation is warranted. One possible explanation is that these objects are unresolved binary systems, and that the poor fits are not necessarily a reflection upon the theoretical models. Another possibility is that J- and H-band

methane absorption is appearing earlier than expected for some objects, or that clouds of another previously-unexplored molecule are found in these objects but not in others. Either of these scenarios would require adjustment to the theoretical models.

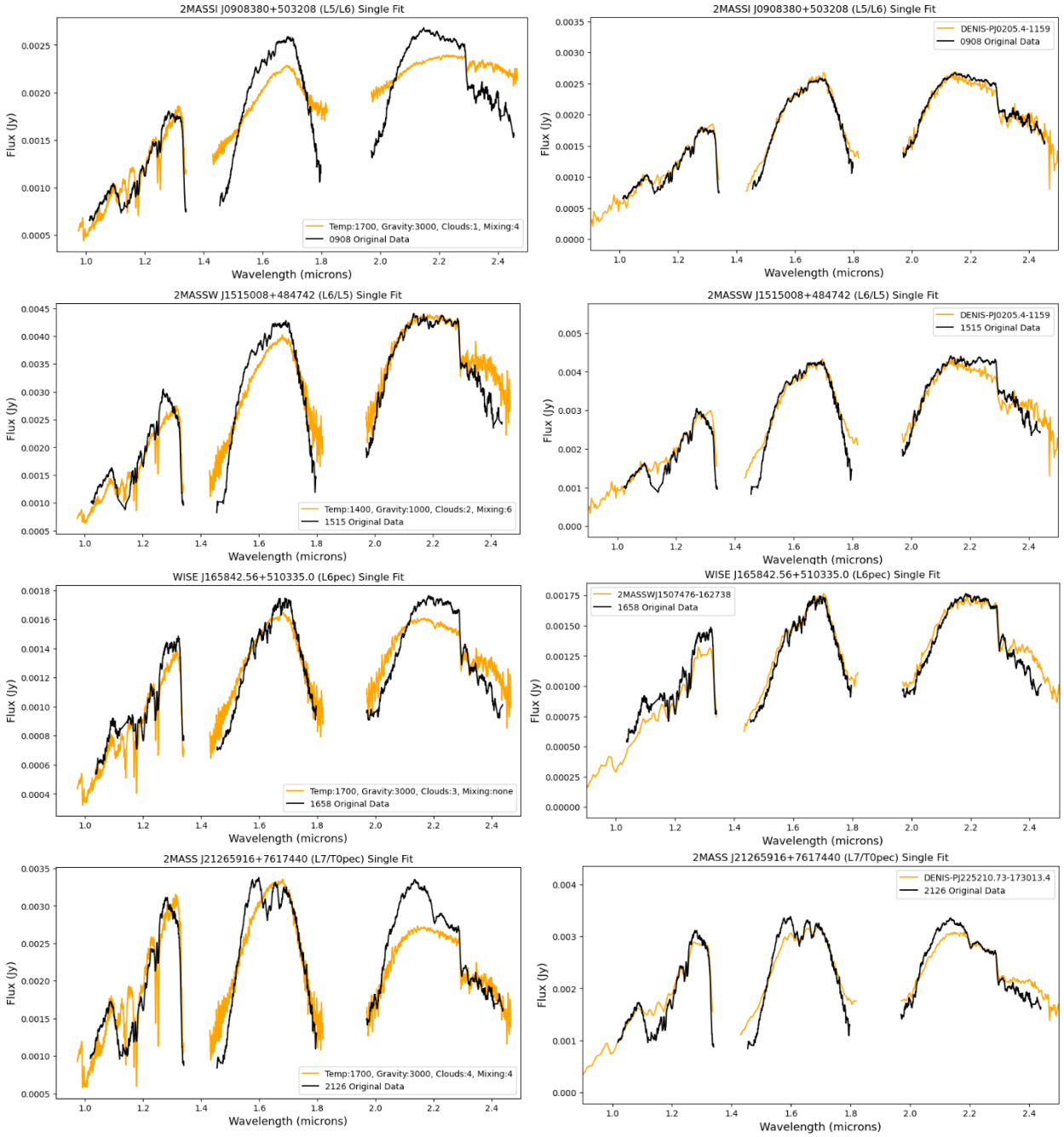

Figure 65: Model-fitting results for the L6-L7 type objects observed with TRIPLESPEC. Black curves correspond to the data, while orange curves correspond to either the theoretical model (SM) fits or the real model (RM) fits. SM fits are on the left, and RM fits are on the right. The legend of each plot gives either the parameters of the best-fit SM model or the object name of the RM model. The wavelength regimes in-between the J, H, and K bands have been masked over due to atmospheric absorption.

8.3.2 L6-L7

The fits for the four TRIPLESPEC objects in this spectral range are given in Figure 65. The SM model fits for these objects are generally poor, aligning with the trend observed in the archival data that SM fits on average are the worst for objects of L/T transition types.

The SM fit for J0908 is exceptionally poor: the model is really only able to fit the J-band. The H- and K-bands are both noticeably underfit. However, the RM fit for J0908 is spot-on, showing that there is at least one other archival object with similar physical characteristics. The simultaneous underfitting of both the H- and K-bands could be an indication that the J-band of J0908 is abnormally suppressed compared to the other two bands. Further modeling with the PICASO code (discussed in the next chapter) could reveal the cause of this suppression.

J1515 has a much better SM fit than J0908, although both the J- and H-bands are slightly underfit. The J-band for this object shows the same truncation observed for all four of the TRIPLESPEC objects of types L4-L5. The SM model fit completely misses this feature.

The SM fit for J1658 is generally good, although the K-band is underfit like was observed for many of the archival objects of this spectral type. This object has a fairly typical late L-type spectrum.

The object J2126 shows both the double-peaked H-band and the truncated J-band seen in J0805. Both objects also have an overluminous K-band compared to the model fit.

8.3.3 L8-T0

The fits for these objects are given in Figure 66. The SM fits for J0031 and J1809 are nearly perfect: the models are able to replicate the K-bands of these objects particularly well. However, the K-band fits for J0920 and J1851 are some of the worst so far. The models under-predict methane absorption and over-predict CO absorption. This could possibly be explained by

the combined effects of the spectral types of these objects being slightly too early and vertical mixing not being sufficiently accounted for.

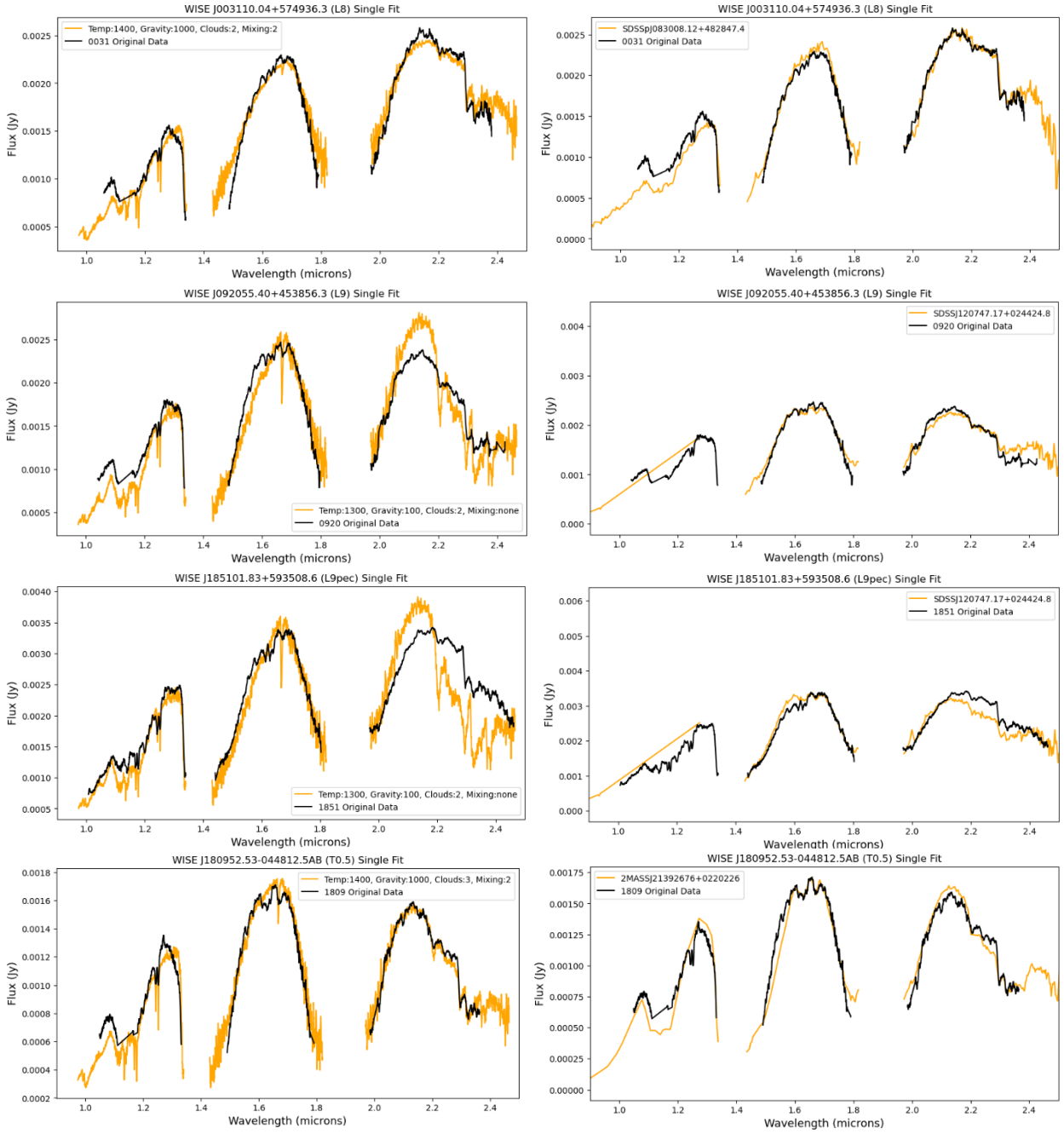

Figure 66: Model-fitting results for the L8-T0 type objects observed with TRIPLESPEC. Black curves correspond to the data, while orange curves correspond to either the theoretical model (SM) fits or the real model (RM) fits. SM fits are on the left, and RM fits are on the right. The legend of each plot gives either the parameters of the best-fit SM model or the object name of the RM model. The wavelength regimes in-between the J, H, and K bands have been masked over due to atmospheric absorption.

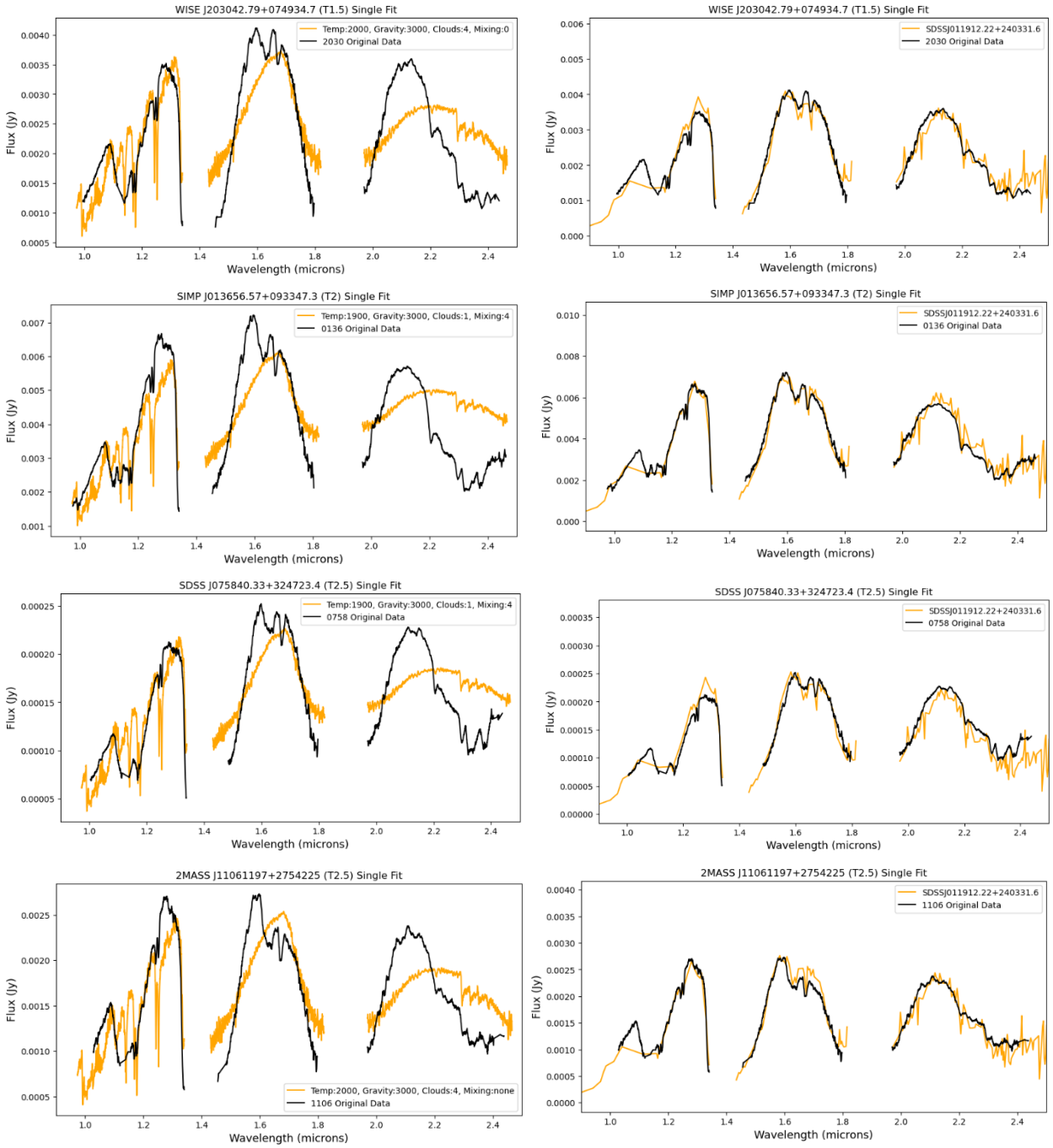

Figure 67: Model-fitting results for the T1-T2 type objects observed with TRIPLESPEC. Black curves correspond to the data, while orange curves correspond to either the theoretical model (SM) fits or the real model (RM) fits. SM fits are on the left, and RM fits are on the right. The legend of each plot gives either the parameters of the best-fit SM model or the object name of the RM model. The wavelength regimes in-between the J, H, and K bands have been masked over due to atmospheric absorption.

8.3.4 T1-T2

The fits for the TRIPLESPEC objects with spectral types from T1-T2 are given in Figure 67. The spectra and fits for all four of these objects are interestingly similar. All four objects show a deepening of the water absorption feature around 1.15 μm that the archival data showed was typical for mid T-types. All four objects show the beginning of methane absorption at 1.6 μm that aligns with the archival early T-types. The shapes of all four K-bands are similar to the K-bands of some of the archival early T-types. However, all four objects were best fit by SM models with temperatures of either 1900 or 2000 K: much too hot for a T-dwarf. These fits match the relative heights of the J- and H-bands (although are missing the deepened water absorption and onset of methane absorption), but completely fail to fit the shape of the K-band.

A few archival early T-type objects had overly hot SM model fits with similar issues, such as J0247 and J1435. While all of these objects have very obvious T-dwarf methane and water absorption, there is something about the relative peak heights of the different bands or the relative CO/methane absorption depths that causes the fitting algorithm to select models with temperatures typical of L-dwarfs. There is a clear model-data discrepancy here.

8.4 Binary Fits

Many of the “odd” objects discussed in the previous three sections can be grouped into families. For example, multiple L-dwarfs had similar H-band plateaus, while other L-dwarfs had H-band double peaks as well as truncated J-bands. One “odd” family for the T-dwarfs included the objects with too-hot model fits. A proposed explanation for the oddities of these objects was that they could be unresolved binary systems containing two brown dwarfs of different spectral

types. Rather than present binary fits for all 322 brown dwarfs in the sample, I chose a few archetypal objects from each "odd" family and use these to investigate the hypothesis of binarity.

8.4.1 Double-Peak Family

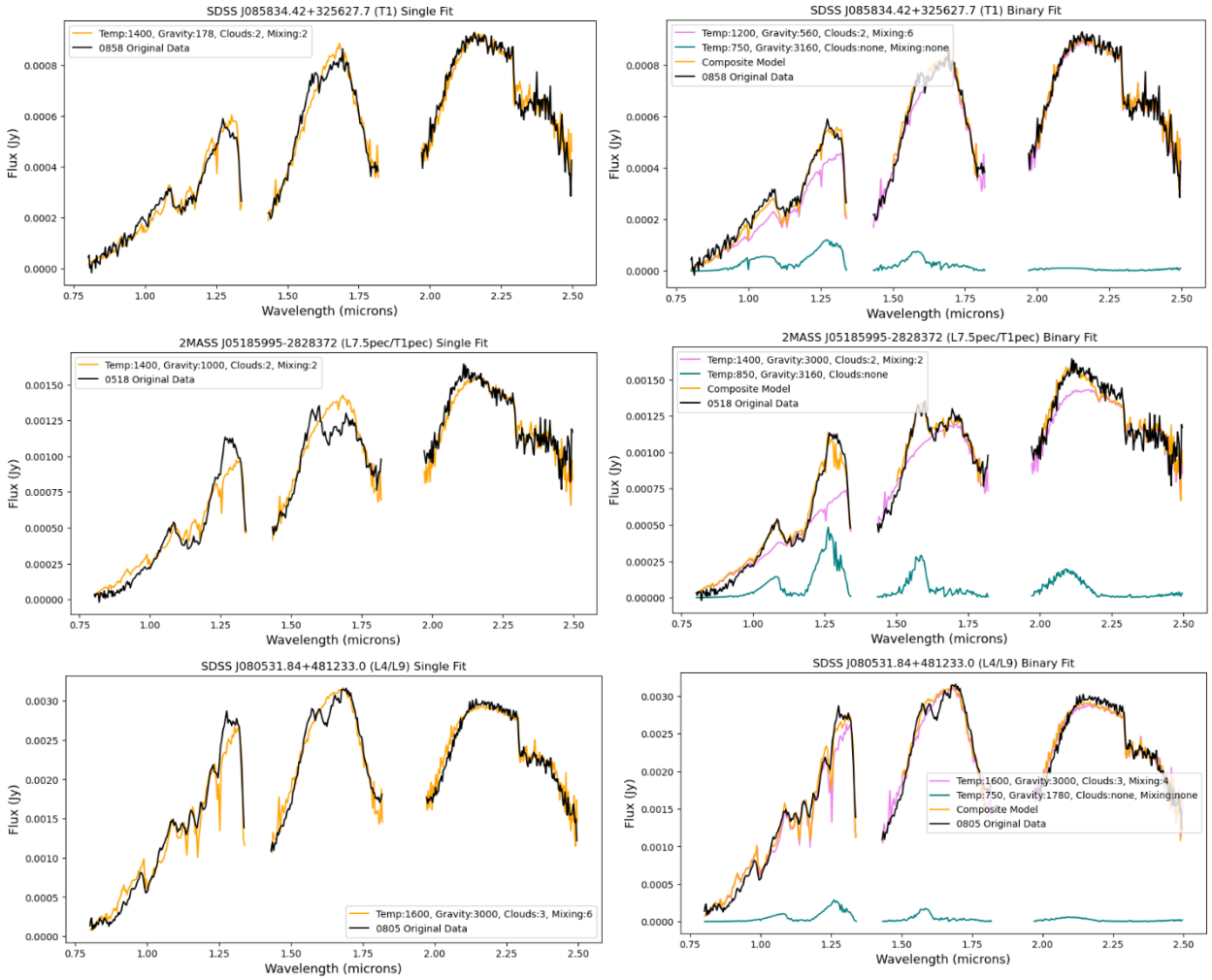

Figure 68: Plots of the single (left) and binary (right) best-fit models of three archival brown dwarfs whose spectra showed a double peak in the H-band. The double peak is most prominent for J0518, which is also the object that shows the most obvious improvement between the single and binary fits.

The archival spectra for J0858, J0518, and J0805 all showed double-peaked H-bands to varying degrees. Their single and binary fits are compared in Figure 68. Each of the three objects matched with composite spectra containing one warmer object (with a temperature that could

correspond to an object of mid L- to early T-type according to Figure 19) and one cooler object (with a temperature consistent with a late T-type or early Y-type). All three objects were fit at least slightly better with the binary model than with the single model, but the improvements for J0858 and J0805 were too small for a conclusive statement regarding possible binarity. However, J0518 is almost certainly an unresolved binary object. This was also the object with the most pronounced H-band double peak. This suggests that strong double peaks are likely explained by binarity, but faint double peaks need to be explored further.

8.4.2 Plateau Family

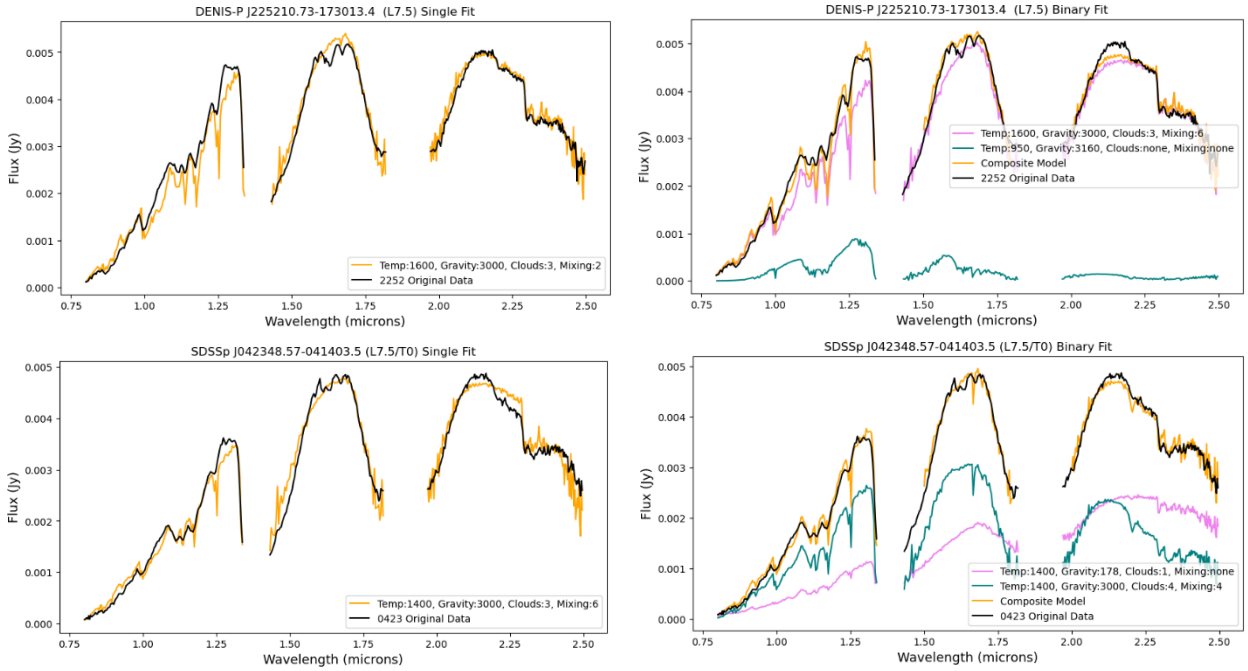

Figure 69: Plots of the single (left) and binary (right) best-fit models of two archival brown dwarfs whose spectra showed a plateau in the H-band and slight methane absorption at 2.2 µm.

Two objects of type L7 were chosen to represent the family of objects with H-band plateaus and early methane absorption at 2.2 µm. The fits of these objects—J2253 and J0423—are given in Figure 69.

The binary fit for J0423 slightly improves the fits of all three bands, but upon further inspection the binary is composed of two models of the same temperature (1400K) just with different values of gravity, clouds, and mixing. I believe this object is not a true binary, but simply did not match well with any of the model grid gravity/clouds/mixing combinations and thus tried to invent its own. This object would be an excellent candidate for PICASO fitting (described in the next chapter).

The binary fit for J2252 is slightly better for the J- and H-bands, but worse for the K-band. Although the composite model for this object contains models of two different temperatures, I still believe it to be unlikely that this object is an unresolved binary.

Both of these late L-dwarfs fall at the beginning of the L/T transition where the archival data fits generally begin to worsen. I conclude that a plateau is not necessarily an indicator of binarity, but is more likely an indication of a true physical process taking place in transition objects that is not well-fit by current model grids.

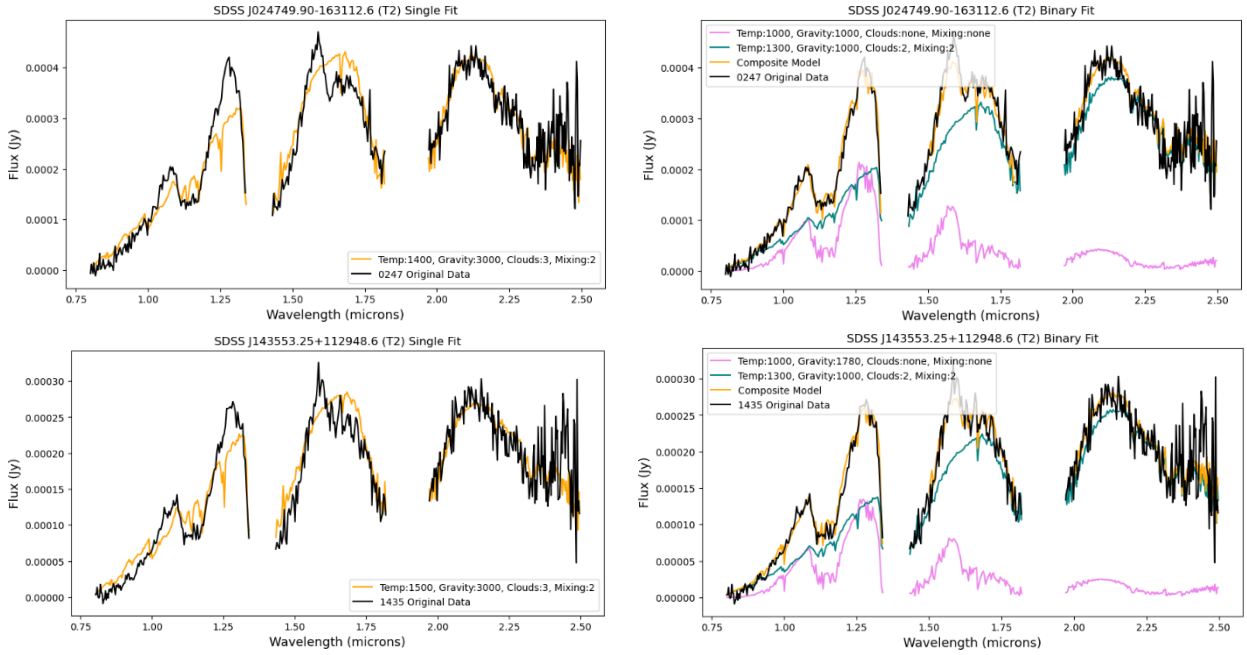

Figure 70: Plots of the single (left) and binary (right) best-fit models of two archival early T-type brown dwarfs whose single fits were too hot to belong to T-dwarfs.

8.4.3 Overly-Hot Early Ts

This family is composed of early T-dwarfs that showed very poor model fits and were best-fit by models with temperatures too high to fit in the spectral type. I chose J0247 and J1435 as the test objects from this group. Their fits are given in Figure 70. I note that the single fits shown in this figure are slightly different from the single fits given in the last chapter. This is a result of the numerical optimization starting from a different guess for this fitting run. For objects that are poorly fit by the data, the optimization function is more likely to find a slightly different answer each time.

These objects are fit significantly better by composite models than single models. Both of their composite models have components with temperatures of 1000 and 1300 K, corresponding to one cool L/T transition object and one mid T-dwarf (according to Figure 19).

I conclude that both of these objects are likely unresolved binary pairs. Other objects in the sample that are overluminous (shown by fits to models with temperatures too hot to belong to their measured spectral type) are thus likely candidates for binarity.

8.4.4 Binary Fits to Only J- and K- Bands

All three "odd-object" families investigated in this section have spectral types that are late enough for at least some methane absorption to be present in their spectra. As discussed in previous sections, many of the models used in this project had outdated H-band methane opacities. Thus, it seemed possible that the binary fits could be influenced by a single model's inability to fit the H-band methane absorption. In order to investigate this possibility further, I performed new binary fits on each of the same 7 archetypal objects, this time excluding the H-band from the fit.

The new fits for the double-peak family are presented in Figure 71. These fits are very similar to those from Figure 68: once again, all three objects fit to a composite spectrum made of one object of mid L- to early T-type and one cooler T-type object. The binary fits for J0858 and J0805 still show only slight improvement over the single fits, but J0518 again seems to be a likely binary candidate. Methane absorption in the H-band does not appear to be the reason for the odd spectral shapes of this family.

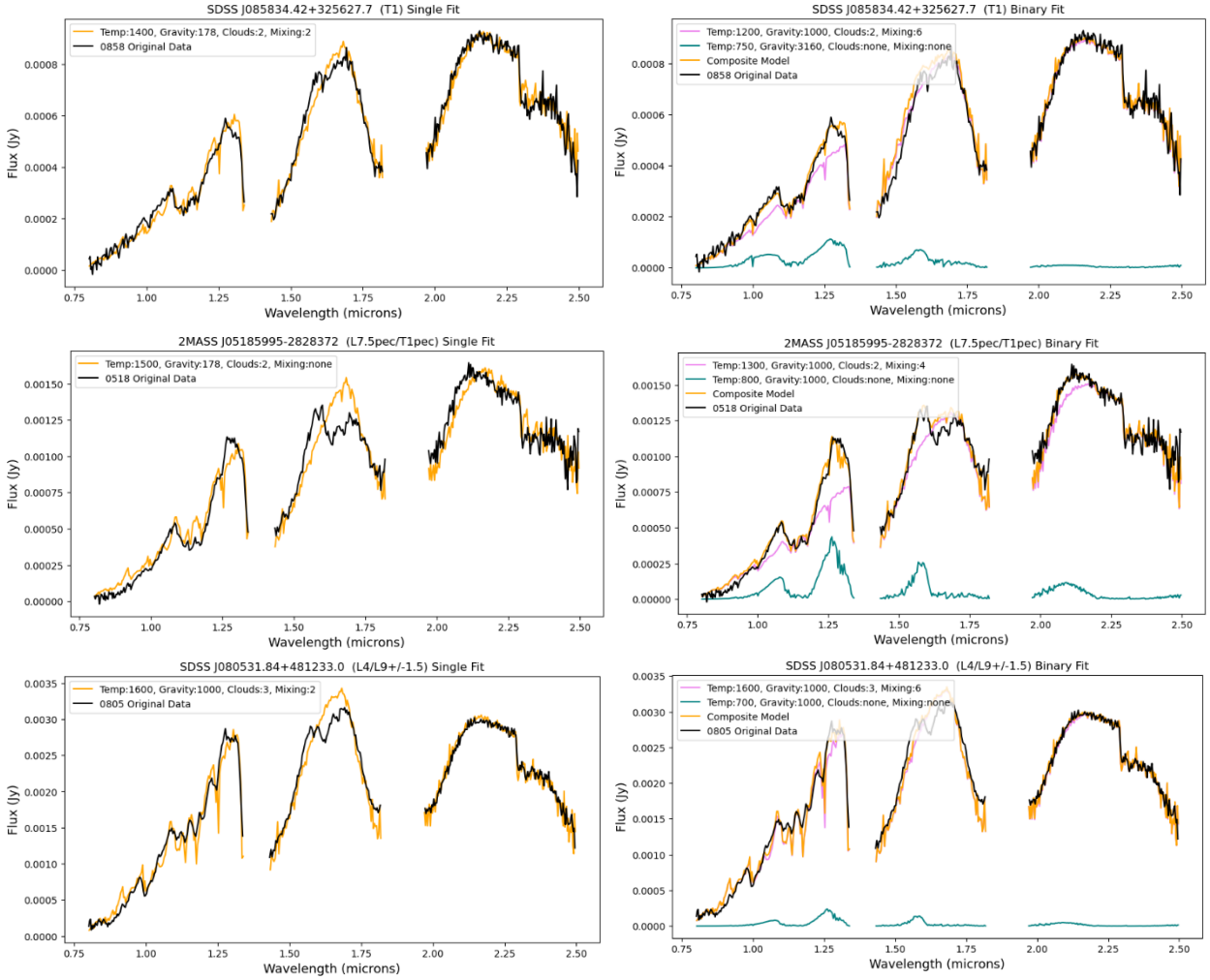

Figure 71: Plots of the single (left) and binary (right) best-fit models of three archival brown dwarfs whose spectra showed a double peak in the H-band. The H-band was masked over for these fits to avoid regions with possible outdated methane opacity values. The fits presented here are very similar to those presented in Figure 68, suggesting that methane is not the cause of any apparent binarity.

The new fits for the family with plateaued H-bands are given in Figure 72. Once again, the difference between the single and binary fits is too slight to provide convincing evidence that these objects could be unresolved binaries.

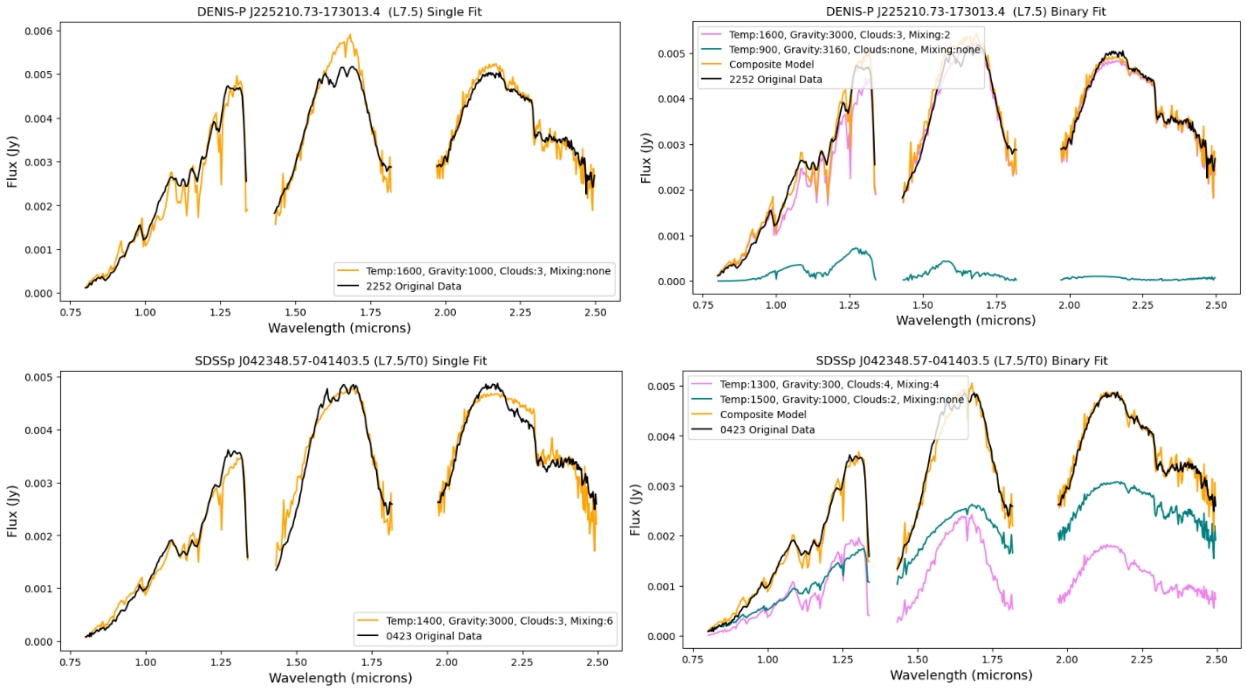

Figure 72: Plots of the single (left) and binary (right) best-fit models of two archival brown dwarfs whose spectra showed a plateau in the H-band and slight methane absorption at 2.2 μm. The H-band was masked over for these fits to avoid regions with possible outdated methane opacity values.

Finally, new fits for the overly-hot early T-dwarfs are given in Figure 73. When the H-band is excluded from the fitting, the new single fits find temperatures that are cool enough to be T-types. However, the best-fit single models significantly overfit the H-band. Interestingly, the binary fits are better-able to match the H-band for these objects even when the H-band is masked over. The J- and K-band shapes are sufficient to identify very similar binary components to those found when the entire spectrum is fit. Methane once again does not seem to be the cause of apparent binarity for this family.

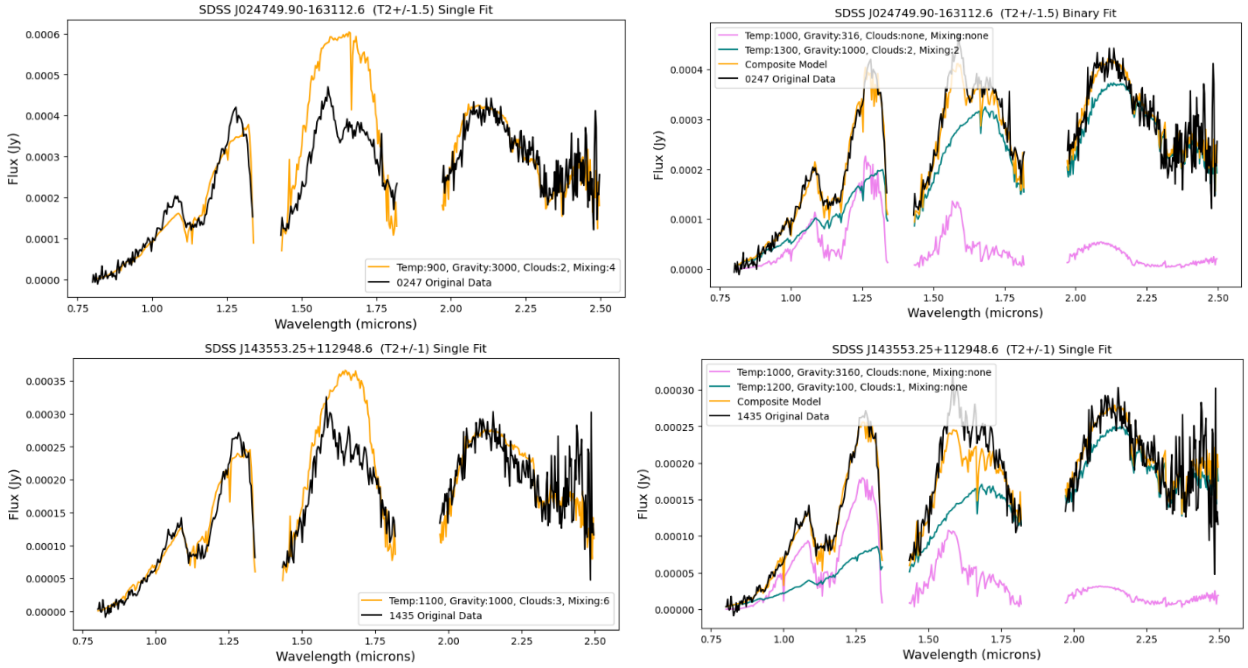

Figure 73: Plots of the single (left) and binary (right) best-fit models of two archival early T-type brown dwarfs whose original single fits were too hot to belong to T-dwarfs. The H-band was masked over for these fits to avoid regions with possible outdated methane opacity values.

Chapter 9

Conclusions

This project has demonstrated that there is much that can be discovered by comparing real brown dwarf data to theoretical models. Here, I summarize the main results of this project and outline plans for future work.

9.1 Summary of General Trends

When the best-fit parameters of the entire sample were plotted against each other, the following general trends were observed:

1. The correlation between temperature and spectral type was shown to loosely follow the shape of a cubic function, although both the scatter of temperatures for each spectral type and the flat region of temperatures make it impossible to assign an exact spectral type to an object based solely on its temperature.
2. Analysis of the temperature and color distribution of the sample suggested that the debate of Best's gap is a simple example of comparing apples to oranges: different authors are defining the L/T transition using terms that are not equivalent. The gap and the pileup could actually exist simultaneously.
3. The absolute J magnitude versus J-K color plot showed that objects in the elbow generally have low surface gravity values. The gravity distribution histograms also

suggested that the number of low gravity objects might fall off after the early T-types, although this could have been caused by the limited number of late T-type objects in the sample.

4. Comparison of the general trends of temperature, gravity, and clouds for objects with optical spectral types versus infrared spectral types suggested that optical spectral types tend to run 1-2 types ahead of infrared types. Thus, optical and infrared types should not be used interchangeably, and papers should be careful to explain which typing system is being used.
5. The distribution of the cloudiness parameter showed that L-dwarfs generally have thicker, hazier clouds than early T-dwarfs. The haziness of the clouds increases until the L/T transition. After the L/T transition, the cloud parameter was difficult to analyze because of the competition between cloudless models with updated methane and the older, cloudy models. However, when fits were limited to the J- and K-bands, T-dwarfs fit either to thin clouds or cloudless models.

9.2 Summary of Type-Specific Trends

Closer inspection of the individual spectra and model fits for each object revealed the following spectral-type-specific trends:

1. The K-band in L-type objects is underfit by the models more often than not.
2. The H-band peaks in L-type objects vary noticeably in shape even within the same spectral type. Notable shapes include triangular peaks, plateaued peaks, and double peaks. The models struggle to fit the wide range of H-band peaks. The double peak appears to be an indicator of binarity, but the plateaued shape is more likely caused by real physical attributes of the brown dwarf atmosphere.

3. Model fits are poor for objects around the L/T transition. The parameter combinations available for current model grids do not appear to have fine enough resolution to fit the many different changes taking place in the atmospheres of L/T transition objects. There could also be physical changes that are not included in the models at all.
4. Objects that are overluminous/have best-fit models with temperatures too high for the spectral type are likely candidates for binarity.
5. Mid T-type models show a flux spike at 1.6 μm that is not present in the data, even when bobcat models are included as fit options. This is likely another methane opacity value that needs to be updated, although it is possible that there is another cloud feature in the mid T-types that is missing from the models.
6. Late T-types are generally underfit in all three bands. This could be a result of model codes overpredicting the cloudiness of these objects.

9.3 Future Work

The sample of archival objects and new observations analyzed in this project included a limited number of late T-type objects and no Y-type objects. An important next step is to expand the sample to include more T- and Y-type objects. A handful of proposals were accepted for JWST Cycle 1 that involved observations of cool brown dwarfs. These data will be made publicly available this summer and can then be used to expand this project to cooler temperatures. Hopefully the inclusion of later spectral types will reveal whether there is a true low-gravity cutoff corresponding to a fragmentation limit, as discussed in Chapter 7.

The results of this project suggested that the surface gravity parameter is not well-constrained by model fits to the entire near-infrared spectrum. Future work could involve fitting

specific wavelength regimes that have been shown by the literature to be particularly sensitive to gravity. This could result in clearer trends in the gravity/spectral type distribution.

Binary fits were performed for many of the archival objects, but time constraints and the lack of a statistical measure of binarity meant that only a few of these binary fits were analyzed. In the future, I plan to improve the statistical aspect of the modeling code so that analyzing the binary fits of a large sample will be more feasible.

We have heard promises from the modeling teams that a new set of atmospheric models is coming that will contain updated methane values as well as clouds. Once these models are released, I plan to perform new model fits to this same sample to see if any of the model-data discrepancies are resolved and if there are any changes to the general trends.

Another important future step, as discussed in Chapter 5, will be adding uncertainty estimates to the fitting code. Running the fits over and over has been shown to produce slightly different results due to the numerical optimization algorithm starting from a different guess, so error analysis will be an important addition to future work. This will allow for more concrete conclusions, especially regarding some of the general trends discussed in Chapter 7.

The main future step is to use the open-source Planetary Intensity Code for Atmospheric Scattering (PICASO) to dig deeper into the common model-data discrepancies (such as the underfit K-band or plateaued H-band in L-type objects) observed as a part of this project. PICASO takes a starting guess for the best-fit parameters of an object and then allows users to iteratively refine the parameter values beyond the capabilities of a pre-existing model grid. With PICASO, users can also add, remove, or change the abundance of different cloud species in order to discover cloud molecules that might be missing from current models. Every time a parameter or cloud abundance value is altered, PICASO uses a radiative transfer code to generate a new

model in real time. PICASO has been mainly used for exoplanet atmospheres to date: this would be the first time that it was used to fit a large sample of brown dwarfs. This is a time-consuming, user-intensive process, but promises to provide deeper insight into why the models are failing to recreate certain spectral features seen in the data. [67,68]

9.4 Conclusion

The purpose of this project was to fit a large sample of archival brown dwarf spectra with theoretical models in search of general trends and areas where current models could be improved. Many trends and model/data discrepancies have been described in this paper. This and future work will provide important data needed to improve modeling techniques and refine theories of brown dwarf evolution.

As brown dwarf models are improved, not only do we gain insight into the physical processes taking place in brown dwarf atmospheres as they cool, but the same modeling techniques can be applied to exoplanetary atmospheres as well. The era of the James Webb Space Telescope promises to bring an explosion of both brown dwarf and exoplanetary observation, so now is the time to update models and prepare to analyze the coming influx of data.

Our understanding of the complex cloud chemistry of substellar atmospheres is evolving continuously, and with it grows our understanding of the universe as a whole. Much work remains to be done in brown dwarf atmospheric research: there are many questions that need answering, but the tools to seek these answers are finally available. Now is a thrilling time to be an infrared astronomer.

Bibliography

[1] S. Kumar, *The Astrophysical Journal*, 137, pp.1121 (1963).
[2] J. C. Tarter, *Astrophysics of Brown Dwarfs*; Proceedings of the Workshop, Fairfax, VA, Oct. 14, 15, 1985 (A87-38226 16-90). Cambridge, England and New York, Cambridge University Press, p. 121-138; Discussion, pp. 138 (1986).
[3] R. Rebolo et al., *Nature*, 377, 6545, pp. 129-131 (1995).
[4] R. Rebolo et al., *The Astrophysical Journal,* 469, pp. L53-L56 (1996).
[5] M. Zapatero-Osorio et al., *Astronomy & Astrophysics*, in press (1996).
[6] G. Basri et al., *The Astrophysical Journal,* 458, pp. 600 (1996).
[7] T. Nakajima et al., *Nature*, 378, 6556, pp. 463-465 (1995).
[8] J. D. Kirkpatrick et al., *The Astrophysical Journal*, 519, Issue 2, pp. 802-833 (1998).
[9] Skrutskie et al., *The Astronomical Journal*, 131, Issue 2, pp. 1163-1183 (2006).
[10] Epchtein et al., *Astrophysics and Space Science*, 217, Issue 1-2, pp. 3-9 (1994).
[11] D.G. York et al., *The Astronomical Journal,* 120, pp. 1579 (2000),
[12] A. J. Burgasser et al., *Conference Proceedings for IAU Ultracool Dwarf Stars Session,* ed. 1, pp. 169–182 (2001).
[13] E. L. Wright et al., *The Astrophysical Journal*, 140, pp. 1868 (2010).
[14] M. Cushing et al., *The Astrophysical Journal*, 743, Issue 1, article id. 50, pp. 17 (2011).
[15] http://www.johnstonsarchive.net/astro/browndwarflist.html
[16] A. J. Burgasser, *Physics Today*, Cambridge, MA: Massachusetts Institute of Technology. 61 (6): pp. 70–71 (2008).
[17] A. Fraknoi, D. Morrison, & S. Wolff, *17.3 the spectra of Stars (and brown dwarfs) - astronomy 2E*. OpenStax. https://openstax.org/books/astronomy-2e/pages/17-3-the-spectra-of-stars-and-brown-dwarfs (2022).
[18] A. P. Boss et al., *Trans. Int. Astron. Union*, Ser. A, 26, 183 (2007).
[19] S. Sorahana et al., *The Astrophysical Journal,* 767 (1): 77 (2013).
[20] M. Marley, American Astronomical Society, DPS meeting #35, id.43.03; *Bulletin of the American Astronomical Society*, Vol. 35, pp. 1006 (2003).
[21] Muirhead et al., *Astro2020: Decadal Survey on Astronomy and Astrophysics*, science white papers, no. 169; Bulletin of the American Astronomical Society, Vol. 51, Issue 3, id. 169 (2019).
[22] A. Burrows et al., *The Astrophysical Journal*, 491, pp. 856 (1997).
[23] https://science.nasa.gov/astrophysics/
[24] C. Wright, *To Study the Next Earth, NASA May Need to Throw Some Shade,* wired.com, (2022).
[25] K. Lodders, *Science*, 303, pp. 323 (2004).
[26] G. Basri, *Brown dwarfs and extrasolar planets*, Proceedings of a Workshop held in Puerto de la Cruz, Tenerife, Spain, 17-21 March 1997, ASP Conference Series #134, edited by Rafael Rebolo; Eduardo L. Martin; Maria Rosa Zapatero Osorio, pp. 394.
[27] Boss et al., *Brown Dwarfs, Proceedings of IAU Symposium #211*, San Francisco: Astronomical Society of the Pacific, 2003, pp. 529.
[28] OpenStax College. *Astronomy*. OpenStax. https://openstax.org/books/astronomy/pages/17-1-the-brightness-of-stars (2016).
[29] G. Alimonty, *EPJ Web of Conferences*, 189, 00003 (2018).

[30] S. Leggett et al., *Monthly Notices of the Royal Astronomical Society*, 373, 2, pp. 781-792 (2006).
[31] A. Burgasser et al., *The Astrophysical Journal*, 681, 579 (2008).
[32] A. Burgasser, "The SpeX Prism Library: 1000+ Low-resolution, Near-infrared Spectra of Ultracool M, L, T and Y Dwarfs". *International Workshop on Stellar Spectral Libraries*, (2014).
[33] *The Spectra of Stars (and Brown Dwarfs).* https://phys.libretexts.org/@go/page/3723 (2022).
[34] Geballe et al., *Proceedings of the 12th Cambridge Workshop on Cool Stars, Stellar Systems, and the Sun*, eprint arXiv:astro-ph/0109331 (2001).
[35] A. Ackerman & M. Marley, *The Astrophysical Journal*, 556, pp. 872-884 (2001).
[36] C. Morley et al., *The Astrophysical Journal,* 756, pp. 172 (2012).
[37] M. Marley et al., *The Astrophysical Journal Letters*, 723, 1, pp. L117-L121 (2010).
[38] D. Saumon & M. Marley, *The Astrophysical Journal*, 689, Issue 2, pp. 1327-1344 (2008).
[39] D. Kirkpatrick et al., *The Astrophysical Journal Supplement Series,* 253, Issue 1, id.7, pp. 85 (2021).
[40] W. Best et al., *Astronomical Journal,* 161, 42 (2021).
[41] M. Marley et al., *The Astrophysical Journal*, 920, Issue 2, id.85, 20 pp. (2021).
[42] K. Cruz et al., *The Astrophysical Journal,* 137, pp. 3345 (2009).
[43] S. Mukherjee et al., *The Astrophysical Journal*, 938, 2 (2022).
[44] C. Morley et al., *The Astrophysical Journal Letters*, 789, Issue 1, article id. L14, 6 pp. (2014).
[45] A. Burgasser et al., *The Astrophysical Journal*, 710, pp. 1142-1169 (2010).
[46] D. Bardalez-Gagliuffi et al., *The Astrophysical Journal*, 794, Issue 2, pp. 143 (2014).
[47] M. Cushing et al., *The Astrophysical Journal*, 678, pp. 1372-1395 (2008).
[48] T. Esplin, *Brigham Young University Undergraduate Senior Thesis*, (2010).
[49] K. Wright, *Brigham Young University Undergraduate Senior Thesis*, (2015).
[50] L. Farnbach, *Brigham Young University Undergraduate Senior Thesis*, (2017).
[51] J. M. Eberhard, *Brigham Young University Undergraduate Senior Thesis*, (2020).
[52] S. Turner, *Brigham Young University Undergraduate Senior Thesis*, (2021).
[53] J. Filippazzo et al., The BDNYC Database (1.0), https://doi.org/10.5281/zenodo.45169 (2016).
[54] J. Rayner et al., *The Publications of the Astronomical Society of the Pacific*, Volume 115, Issue 805, pp. 362-382 (2003).
[55] C. Gellino & D. Kirkpatrick, DwarfsArchives.org.
[56] Wenger et al., *Astronomy and Astrophysics Supplement Series*, 143, 9 (2000).
[57] Gaia Collaboration et al., *The Gaia mission (provides a description of the Gaia mission including spacecraft, instruments, survey and measurement principles, and operations)* (2016).
[58] Gaia Collaboration et al., *Summary of the contents and survey properties* (2018).
[59] W. Best *et al*., *Astronomical Journal,* **159,** 257 (2020).
[60] J. Wilson et al., *Ground-based Instrumentation for Astronomy. Proceedings of the SPIE*, Volume 5492, pp. 1295-1305 (2004).
[61] C. Scoresby, *Brigham Young University Undergraduate Senior Thesis* (2023).
[62] D. Golimowski et al., *The Astronomical Journal*, Volume 127, Issue 6, pp. 3516-3536 (2004).

[63] D. Stephens et al., *The Astrophysical Journal*, Volume 702, Issue 1, pp. 154-170 (2009).
[64] G. Knapp et al., *The Astronomical Journal*, Volume 127, Issue 6, pp. 3553-3578 (2004).
[65] Whitworth & Stamatellos, *Astronomy and Astrophysics*, Volume 458, Issue 3, pp. 817-829 (2006).
[66] J. Faherty et al., *The Astrophysical Journal Supplement Series*, Volume 225, Issue 1, article id. 10, 57 pp. (2016).
[67] N. Batalha et al., *The Astrophysical Journal*, *878*(1), pp.70 (2019).
[68] S. Mukherjee et al., *The Astrophysical Journal*, *942*(2), pp. 71 (2023).
[69] Chiu et al., *The Astronomical Journal,* 131, 5, pp. 2722-2736 (2006).
[70] A. Burgasser, *The Astrophysical Journal*, 659, 655 (2007).
[71] K. Cruz et al., *The Astrophysical Journal*, 604, L61 (2004).
[72] D. Kirkpatrick et al., *The Astrophysical Journal*, 639, 1120 (2006).
[73] Reid et al., *The Astrophysical Journal*, 639, 1114 (2006).
[74] Siegler et al., *The Astronomical Journal*, 133, 2320 (2007).
[75] Burgasser & McElwain, *The Astronomical Journal*, 131, 1007 (2006).
[76] A. Burgasser et al., *The Astronomical Journal*, 127, 2856 (2004).
[77] McElwain & Burgasser, *The Astronomical Journal*, 132, 2074 (2006).
[78] Looper, Kirkpatrick, and Burgasser, *The Astronomical Journal*, 134, 1162 (2007).
[79] Sheppard & Cushing, *The Astronomical Journal*, 137, 304 (2009).
[80] Looper et al., *The Astrophysical Journal*, 686, 528 (2008).
[81] A. Burgasser et al., *The Astrophysical Journal*, 639, 1095 (2006).
[82] D. Kirkpatrick et al., *The Astrophysical Journal Supplement*, 190, 100 (2010).
[83] Burgasser, Bardalez Gagliuffi & Gizis, *The Astrophysical Journal*, in press (2010).
[84] Gelino & Burgasser, *The Astrophysical Journal*, 140, 110 (2010).
[85] Burgasser, Dhital & West, *The Astrophysical Journal*, 138, pp. 1563-1569 (2009).
[86] Schmidt et al., *The Astrophysical Journal*, 139, pp. 1045-1050 (2010).
[87] Luhman et al., *The Astrophysical Journal*, 654, 570 (2007).
[88] Liebert & Burgasser, *The Astrophysical Journal*, 655, 522 (2007).
[89] M. Cushing (unpublished).
[90] B. Miles et al., *The Astrophysical Journal Letters,* 946, 1, id.L6, 19 pp. (2023).

Appendix 1

Instructions for Running the Code

Introduction to the Code:

The purpose of this code is to match brown dwarf spectral data to best-fit brown dwarf atmospheric models.

The original intended application was to determine the likelihood that an object was an unresolved binary pair rather than a single object, and this feature remains in the code. However, fitting spectral data to single models (as opposed to the composite models used to model binary pairs) has also come to be an important application. Fitting data to single models will help us to establish a better understanding of the connection between spectral type and temperature and more easily note spectral features that might be missing from our models. There are four different types of fits that can be performed using this code:

1.SMSF, which stands for Saumon & Marley Single Fit.

2.SMBF, which stands for Saumon & Marley Binary Fit

3.RMSF, which stands for Real Model Single Fit.

4.RMBF, which stands for Real Model Binary Fit.

The Saumon & Marley fits use a compilation of brown dwarf atmospheric models created by Saumon & Marley and released in a few different papers. The real model fits use a collection of 166 real brown dwarf spectra taken from the SpeX Prism Archive. These real models have been anti-normalized and distance-corrected with their GAIA parallaxes.

The single fits compare your target object to each model and determine the best match using an adapted chi-squared algorithm presented in Cushing et al. [47].

The binary fits compare your target object to composite models using the same chi-squared algorithm. The composite models are generated by taking every possible combination of two models and adding the flux of each pair together at each wavelength. These composite models mimic the spectra of spectral binary pairs.

If you opt to perform both a single and a binary fit for the same model type, the code will perform a statistical analysis after fitting and give you a percent likelihood that your object is a binary pair rather than a single object. Note that the code will not perform the statistical analysis if you only run one type of fit or run the single and binary fit with separate commands.

Note that we opted for ease of use rather than speed, and therefore wrote this code in Python rather than C++. While the code can take anywhere from a few seconds to 2.5 hours (depending on the fits performed and the set of models used) to run on a single object, it has been designed so that even an individual with no coding experience can call the code with a single command and then walk away until the code has finished.

If you notice issues, bugs, or other areas for improvement, please contact Savanah Turner at savanahkayturner@gmail.com.

Downloading the Code:

All of the files needed to run the code can be found at this GitHub address: https://github.com/savanahkay/binary-fit.git.

The Python code files can also be found in the google drive folder Stephen-sResearchGroup/BinaryFitting/Code. This folder is only available to members of Dr. Stephen's research group and will not contain the model folders due to their large size, so for the initial download it would be best to pull everything from git. If changes are made after your download, you could then grab the most recent code files from the google drive folder without having to deal with git.

If using git, please download the code and then move the code to a separate folder so that you do not accidentally push changes to GitHub and overwrite the code.

Running the code requires Python 3 and the following packages: numpy, scipy, tqdm, os, pandas, itertools, and matplotlib. Ensure that the necessary packages have been installed on your machine.

Preparing to Run the Code:

In order to run the code, you need to do the following things:

- Generate a text file containing the spectrum of each target. Any non-data lines can be left in the file, but need to be commented out with a "#". The data in the text file should be in the order of wavelength, flux, then errors. Name the text file "0000Raw.txt", replacing the zeros with the first four numbers in the target name. Any lines containing flux values recorded as "nan" should be either commented out or deleted.
- Place all of the target text files together in a folder in the directory containing the code.
- Update the text file called "objects.txt" to include the 4 digit number codes (the same used to name the data text files) and 2MASS H- and K-magnitudes of each target. Note that you only need the magnitudes if your data is normalized and you want the code to perform anti-normalization. If your data is not normalized, you can just fill in zeroes for the magnitudes.
- Update the "params.txt" file to include the units of your wavelength and flux values. If your data is not given in any of the unit options given in the "params.txt" file, the code does not yet have functionality to accept these units. You can send an email to savanahkayturner@gmail.com requesting functionality be added for the desired units. Note that while the code can be run on multiple objects at once, because there is only one params file you can only batch-run objects with the same units.
- Update the "params.txt" file to indicate whether or not your data is already flux-normalized.
- Update the "params.txt" file to indicate which type(s) of fit you wish to perform.

- Update the “params.txt” file to indicate the folder names containing the FilterData, filters used to unnormalize the data, target object data files, Saumon & Marley model files, and real data model files.
- Update the “params.txt” file to indicate whether or not your target data contains error values.
- Update the “params.txt” file to indicate whether or not you wish all plots to be made on a log(wavelength) scale. (This feature is useful for data spanning both the near- and mid- infrared).
- Update the “params.txt” file to indicate any wavelength spans you wish to omit from the fitting routine, such as the usual gaps from 1.35 to 1.5 microns, 1.8 to 2.0 microns, and 2.5 to 5 microns. At this point the code will crash if you include gaps that extend beyond the wavelength range of your target data, so be sure to check this.

A note regarding choice of model folder: I have created sets of models that have been smoothed and regridded to match the wavelength range and resolution of various data sets. The git repository contains a folder called “modelFolders” that holds each model set. Before running the code, you will need to choose which model set you want to use and copy the folder containing this model set from “modelFolders” and paste it into the same directory as the code files.

Current model subsets are the Saumon & Marley 2008 models, models from Morley et al. (2012), models from Morley et al. (2014), the Sonora Bobcat models, and a set called “mixedModels” that includes the models from all of these subsets.

Within the folder for each model subset are folders containing the actual models, labeled for the data sets they have been regridded to match. For example, if I wish to perform fits to data obtained from the SpeX spectrograph and want to use the mixed model subset, I would need to use the folder of models called “mixedModelsForSpex”. After copying the desired folder of models into the same directory as the code, be sure to update the params file to give the correct model folder name.

Note that the Spitzer model set is for Spitzer data with wavelength ranges from 0.8 - 2.4 microns, while the SpitzerFull model set is for Spitzer data from 0.8 - 14.9 microns.

If you want to run fits on data taken from a telescope with range/resolution that does not match any of these four model sets, contact us to request a new model set.

Running the Code:

Once you have finished preparing to run the code, simply execute the main.py script and all of the fitting will be performed. You can either open the main.py script using some IDE such as Spyder and run the script using the IDE, or you can run the script from the terminal. To run from the terminal, navigate to the folder containing your code and then type “python3 main.py” and push “enter.”

Note that the run time varies drastically for the different fit types and different model sets. Progress bars will be displayed in the terminal to give an idea of how long the code will take. Single fits should generally take less than 15 seconds per object, while binary fits should take between 20 minutes and 2.5 hours per object.

The code will generate multiple files and place them in a folder for each target. Resultant files will include graphs of the the spectral fits, text files containing the best-fit spectra, and spreadsheets containing lists of all of the fits tried, sorted by chi-squared value.

Example params.txt File

#What are the units of your wavelength values? (angstroms or nm or um)
um
#What are the units of your flux values? (erg/cm^2/s/Hz or W/m^2/um or Jy or erg/cm^2/s/A)
W/m^2/um
#Is your data normalized? (Y/N)
Y
#Do you wish to perform a BF to the Saumon and Marley models? (Y/N):
Y
#Do you wish to perform a SF to the Saumon and Marley models? (Y/N):
Y
#Do you wish to perform a BF to the real data models? (Y/N):
Y
#Do you wish to perform a SF to the real data models? (Y/N):
Y
#Where is the FilterData folder located?
FilterData
#Where is the unnormalizeFilters folder located?
unnormalizeFilters
#Where are your object data txt files located?
LDwarfs
#Where are the saumon and marley model files located?
mixedForSpex
#Where are the real data model files located?
spexDistanceUnnormalized
#Do your target objects have error values? (Y/N):
Y
#Do you want to plot on a log(wavelength) scale? (Y/N):
N
#List any wavelength spans you wish to omit from the fitting routine
0.6,0.8
1.35,1.5
1.8,2.0

Example objects.txt File

#Format is: 4 digit object code tab Hmag tab Kmag
1435 16.15 16.906
2252 13.36 12.901
1171 14.09 15.01
0809 12.07 12.98
1423 13.17 14.91

main.py

```
# -*- coding: utf-8 -*-
"""
Created on Wed Feb 23 09:22:28 2022

@author: savan
"""
import numpy as np
import savvySpectrum
from savvyFitter import fitter, binaryFitter
from scipy.integrate import simps
from regridTheSpectrum import regridModels, regridModelsWithErrors
from tqdm import tqdm
import os
import pandas as pd
import matplotlib.pyplot as plt
from scipy.stats import f

#initialize global variables used to store parameter information
fluxUnits = wavelengthUnits = filterFolder = None
unnormalizeFilterFolder = dataFolder = None
SMmodelFolder = RMmodelFolder = None
normalized = SMBF = SMSF = RMBF = RMSF = areThereErrors = logPlot = False
gapList = []

#Parse through the params file to get information regarding
#type of fit and location of files. Update global variables.
def parse_params(paramsFile):
    file = open(paramsFile,"r")
    contents = file.readlines()
    contents = [line.rstrip('\n') for line in contents]
    global fluxUnits,wavelengthUnits,filterFolder,dataFolder
    global unnormalizeFilterFolder, SMmodelFolder, RMmodelFolder
    global normalized, SMBF, SMSF, RMBF, RMSF
    global gapList, areThereErrors, logPlot
    wavelengthUnits = contents[1]
    fluxUnits = contents[3]
    filterFolder = contents[15]
    unnormalizeFilterFolder = contents[17]
    dataFolder = contents[19]
    SMmodelFolder = contents[21]
    RMmodelFolder = contents[23]
    if contents[5] == "Y":
        normalized = True
```

```
    if contents[7] == "Y":
        SMBF = True
    if contents[9] == 'Y':
        SMSF = True
    if contents[11] == 'Y':
        RMBF= True
    if contents[13] == 'Y':
        RMSF = True
    if contents[25] == 'Y':
        areThereErrors = True
    if contents[27] == 'Y':
        logPlot = True
    if len(contents) > 27:
        numberOfGaps = len(contents) - 29
        gapList = [None]*numberOfGaps
        for i in range(0,numberOfGaps):
            gapList[i] = contents[29+i]
        gapList = readGapList(gapList)
    file.close()

#Parse through objects text file to get names of all
#targets to be fit as well as their magnitudes to use
#for unnormalization if necessary
def parse_objects(objectsFile):
    objects,Hmags,Kmags = np.loadtxt(objectsFile,dtype=str,unpack = True);
    if hasattr(objects, '__len__') and (not isinstance(objects, str)):
        Hmags = [float(Hmag) for Hmag in Hmags]
        Kmags = [float(Kmag) for Kmag in Kmags]
    #else statement is for dealing with single-object input
    else:
        tempH = float(Hmags)
        Hmags = []
        Hmags.append(tempH)
        tempK = float(Kmags)
        Kmags = []
        Kmags.append(tempK)
        tempO = objects
        objects = []
        objects.append(tempO)
    return objects,Hmags,Kmags

#TODO: might need to add more functionality here if normalized data does not
#always come in erg/cm^2/s/A

#Choose needed flux conversion function based on
#input data inuts
def choose_flux_conversion_func(inputUnit):
    conversionFunction = None
    if inputUnit == 'W/m^2/um'and normalized == True:
        print("Your data is already in W/m^2/um and antinormalization will complete the
conversion to Jy, so no conversion is needed here.")
    elif inputUnit == 'erg/cm^2/s/A'and normalized == False:
        conversionFunction = 'ergLam2Jy'
    elif inputUnit == 'W/m^2/um' and normalized == False:
        conversionFunction = 'W2Jy'
    elif inputUnit == 'Jy' and normalized == False:
        print("Your data is already in Jy, so no conversion is needed")
    elif inputUnit == 'erg/cm^2/s/Hz' and normalized == False:
        conversionFunction = 'ergNu2Jy'
    else:
        print ("The flux unit you entered is not recognized. Please try again")
    return conversionFunction

#Choose needed wavelength conversion function based on
#input wavelength units
```

```
108. def choose_wavelength_conversion(inputUnit):
109.     if inputUnit == "um":
110.         conversionFactor = 1
111.     elif inputUnit == "angstroms":
112.         conversionFactor = 0.0001
113.     elif inputUnit == "nm":
114.         conversionFactor = 0.001
115.     else:
116.         print ("The wavelength unit you entered is not recognized. Please try again")
117.         conversionFactor = 0
118.     return conversionFactor
119. 
120. #Convert from watts to janskys
121. def W2Jy(wavelengths,fluxes,errors):
122.     fluxes = fluxes*wavelengths*wavelengths*1e26/2.99792458e14
123.     errors = errors*wavelengths*wavelengths*1e26/2.99792458e14
124.     return (fluxes,errors)
125. 
126. #Convert from Flambda in erg to janskys
127. def ergLam2Jy(wavelengths,fluxes,errors = None):
128.      fluxes = fluxes*wavelengths*wavelengths*(10**8)*(2.99792458*10**4)
129.      if errors != None:
130.          errors = errors*wavelengths*wavelengths*(10**8)*(2.99792458*10**4)
131.      return (fluxes,errors)
132. 
133. #Convert from Fnu in erg to janskys
134. def ergNu2Jy(wavelengths,fluxes,errors):
135.     fluxes = fluxes * (10**23)
136.     errors = errors * (10**23)
137.     return(fluxes,errors)
138. 
139. #use known magnitudes and filter profiles to un-Normalize
140. #flux-normalized data to allow for better fits.
141. #This function was written by John-Michael Eberhard.
142. def unNormalize(name,wavs,fluxes,errors,Hmag,Kmag):
143.     fluxVegaH=11.38e-11;#erg cm-2 s-1 A-1
144.     fluxVegaK=3.961e-11; #erg cm-2 s-1 A-1
145.     wavsFilter,filterData =
np.loadtxt(f'{unnormalizeFilterFolder}/MASSallFilters.txt',unpack=True,comments='#');
146.     wavsFilterH,filterDataH =
np.loadtxt(f'{unnormalizeFilterFolder}/MASSHFilter.txt',unpack=True,comments='#');
147.     filterDataH_newGrid  = np.interp(wavs,wavsFilterH,filterDataH);
148.     I1H= simps(filterDataH_newGrid*fluxes*wavs,wavs)
149.     I2H= simps(filterDataH_newGrid*wavs,wavs)
150.     FlambdaH = I1H/I2H
151.     myFluxH= 10**((Hmag)/-2.5) * fluxVegaH
152.     myFluxH = myFluxH/(1e-10)*(1e-6)/(1e-4)/(1e7)
153.     myRatioH = myFluxH/FlambdaH;
154.     wavsFilterK,filterDataK =
np.loadtxt(f'{unnormalizeFilterFolder}/MASSKFilter.txt',unpack=True,comments='#');
155.     filterDataK_newGrid  = np.interp(wavs,wavsFilterK,filterDataK);
156.     I1K= simps(filterDataK_newGrid*fluxes*wavs,wavs)
157.     I2K= simps(filterDataK_newGrid*wavs,wavs)
158.     FlambdaK = I1K/I2K
159.     myFluxK= 10**((Kmag)/-2.5) * fluxVegaK
160.     myFluxK = myFluxK/(1e-10)*(1e-6)/(1e-4)/(1e7)
161.     myRatioK = myFluxK/FlambdaK;
162.     avgRatio= (myRatioK+myRatioH)/2;
163.     unNormalFlux = fluxes*avgRatio;
164.     fluxesInJy= unNormalFlux*1e26/2.99792458e14*wavs*wavs;
165.     unNormalError = errors*avgRatio;
166.     errInJy = unNormalError*1e26/2.99792458e14*wavs*wavs;
167.     unnormalizedData=np.column_stack((wavs,fluxesInJy,errInJy))
168.     np.savetxt(f'{name}/{name}unnormalized.txt',unnormalizedData)
169.     return (wavs,fluxesInJy,errInJy)
```

```
170.
171. #TODO: check this with stats professor
172. #Function written by John-Michael Eberhard. Performs an fTest after fitting to
173. #determine likelyhood that target is binary. Generates a statistical curve
174. #giving the eta value needed for each percent confidence level.
175. def fTest(eta,dof,name,code,bestSingleName,singleScale,bestBinaryName,binaryScale):
176.     rv1 = f(dfn=dof, dfd=dof, loc=0, scale=1)
177.     x = np.linspace(rv1.ppf(0.0001), rv1.ppf(0.9999), 100)
178.     y = rv1.pdf(x)
179.     per99=rv1.ppf(0.99)
180.     per95=rv1.ppf(0.95)
181.     per90=rv1.ppf(0.90)
182.     confLevel=100
183.     counter=1
184.     while eta<confLevel:
185.         confLevel=rv1.ppf(counter)
186.         counter=counter-.01
187.     if eta > per99:
188.         conf="above 99% confidence"
189.     else:
190.         if eta > per95:
191.             conf= "between 95-99% confidence"
192.         else:
193.             if eta >per90:
194.                 conf="between 95-99% confidence"
195.             else:
196.                 conf="below 90% confidence"
197.     #create statistics plot
198.     plt.figure()
199.     plt.xlim(0.5,per99+.5)
200.     plt.plot(x,y, 'b-')
201.     plt.ylabel('Probability Distribution',fontsize=12)
202.     plt.xlabel('η value',fontsize=12)
203.     plt.plot(x,y, 'y')
204.     plt.axvline(x=per99,c='g')
205.     plt.axvline(x=per95,c='y')
206.     plt.axvline(x=per90,c='r')
207.     plt.axvline(x=eta,c='k')
208.     plt.text(per99, max(y)-.5,'99%',rotation=90)
209.     plt.text(per95, max(y)-.5,'95%',rotation=90)
210.     plt.text(per90, max(y)-.5,'90%',rotation=90)
211.     plt.text(eta, max(y)-1.5,'ηsb')
212.     plt.savefig(f'{name}/{code}{name}StatsPDF.pdf')
213.     #Save stats to file
214.     file= open(f'{name}/{code}{name}stats.txt',"w+")
215.     file.write(f'The best single fit was with the model {bestSingleName} and a scale factor of
{singleScale}.')
216.     file.write(f'\nThe best binary fit was with the composite model {bestBinaryName} and a
scale factor of {binaryScale}.')
217.     file.write(f'\n99%: {per99}')
218.     file.write(f'\n95%: {per95}')
219.     file.write(f'\n90%: {per90}')
220.     file.write(f'\nmy eta value: {eta}\n')
221.     file.write(conf)
222.     file.close()
223.
224. #Generate plots for a list of spectrum objects
225. def plotSpectra(spectrumObjects,objectsNames,name,file,logPlot = False):
226.     plt.figure(figsize=(8,6))
227.     i = 0
228.     for spectrum in spectrumObjects:
229.         plt.plot(spectrum.wavs, spectrum.fluxes,label = f'{objectsNames[i]}')
230.         if logPlot:
231.             plt.semilogx()
232.         i = i + 1
```

```
    plt.legend()
    plt.title(name)
    plt.ylabel('Flux (Jy)',fontsize=13)
    plt.xlabel('Wavelength (microns)',fontsize=13)
    plt.savefig(f'{file}/{name}.png')
    plt.close()
```

```
#Function used to calculate an eta value. The equation for eta
#in John-Michael Eberhard's senior thesis included degrees of freedom,
#but in his own code he determines the degree of freedom to be one minus
#the number of data points used in each fit, and since I use the same number
#of data points for single and binary fitting, this value cancels out. He
#made the same assumption in his own code.
def calculateEta(bestSingleChi,bestBinaryChi):
    return bestSingleChi/bestBinaryChi

#TODO: Works well for temp and gravity, but needs refining for f and kzz values and bobcats
def breakModelNameIntoCharacteristics(objectName):
    tempIndex = objectName.find('sp_')
    gravityIndex = objectName.find('g')
    temp = objectName[tempIndex+4:gravityIndex]

    isNCpresent = objectName.find('nc')
    isKZZpresent = objectName.find('kzz')
    isFpresent=objectName.find('f')

    if isNCpresent != -1:
        gravity=objectName[gravityIndex+1:-6]
        clouds = "nc"
        mixing = "none"

    if isFpresent != -1:
        gravity=objectName[gravityIndex+1:isFpresent]
        if isKZZpresent != -1:
            clouds = objectName[isFpresent+1:isKZZpresent-1]
            mixing = objectName[isKZZpresent+3:-4]
        else:
            clouds = objectName[isFpresent+1:-4]
            mixing = "none"
    return (temp,gravity,clouds,mixing)

#Take the top 100 S&M single fits and print characteristics to csv
def printTop100FitCharacteristics(fitList,top100FileName):
    df = pd.read_csv(fitList)
    matrix2 = df[df.columns[1]]
    list2 = matrix2.tolist()
    names=[None]*100
    temps = [None]*100
    gravities = [None]*100
    clouds = [None]*100
    mixings = [None]*100
    for i in range(0,100):
        names[i]=list2[i]
        props = breakModelNameIntoCharacteristics(list2[i])
        temps[i]=props[0]
        gravities[i]=props[1]
        clouds[i]=props[2]
        mixings[i]=props[3]
    dict = {'name':names,'temp':temps,'gravity':gravities,'clouds':clouds,'mixing':mixings}
    df = pd.DataFrame(dict)
```

```
298.     df.to_csv(top100FileName)
299. 
300. #Take the top 100 S&M binary fits and print characteristics to csv
301. def printTop100FitCharacteristicsForBinaries(fitList,top100FileName):
302.     df = pd.read_csv(fitList)
303.     matrix2 = df[df.columns[1]]
304.     list2 = matrix2.tolist()
305.     names1 = [None]*100
306.     names2=[None]*100
307.     temps1 = [None]*100
308.     temps2 = [None]*100
309.     gravities1=[None]*100
310.     gravities2=[None]*100
311.     clouds1=[None]*100
312.     clouds2=[None]*100
313.     mixings1=[None]*100
314.     mixings2=[None]*100
315.     for i in range(0,100):
316.         SMBF1,SMBF2,empty = list2[i].split(".txt")
317.         names1[i] = SMBF1 + '.txt'
318.         names2[i] = SMBF2 + '.txt'
319.         props1 = breakModelNameIntoCharacteristics(names1[i])
320.         props2=breakModelNameIntoCharacteristics(names2[i])
321.         temps1[i]=props1[0]
322.         gravities1[i]=props1[1]
323.         clouds1[i]=props1[2]
324.         mixings1[i]=props1[3]
325.         temps2[i]=props2[0]
326.         gravities2[i]=props2[1]
327.         clouds2[i]=props2[2]
328.         mixings2[i]=props2[3]
329.     dict =
{'name1':names1,'name2':names2,'temp1':temps1,'temp2':temps2,'gravity1':gravities1,'gravity2':gravit
ies2,'clouds1':clouds1,'clouds2':clouds2,'mixing1':mixings1,'mixing2':mixings2}
330.     df = pd.DataFrame(dict)
331.     df.to_csv(top100FileName)
332. 
333. #TODO: write this function
334. #Generate errors in the S&M fits using the Excel Sheet
335. def calculateErrors():
336.     pass
337. 
338. #turn gapList (currently a list where each element is a string containing the whole gap)
339. #into a list of tuples giving range of gaps as floats
340. def readGapList(gapList):
341.     i = 0
342.     newGapList = [None]*len(gapList)
343.     for gap in gapList:
344.         values = gap.split(",")
345.         first = float(values[0])
346.         second = float(values[1])
347.         newGapList[i] = (first,second)
348.         i = i+1
349.     return newGapList
350. 
351. #TODO: Fix in case gaps are outside of the range of the data
352. #mask over wavelength ranges given in params file that
353. #user does not want to include in the fit
354. def maskOverGaps(wavs,fluxs,gapList,errors=None):
355.     for gap in gapList:
356.         endpt1 = gap[0]
357.         endpt2 = gap[1]
358.         startIndex = next(x for x, val in enumerate(wavs) if val > endpt1)
359.         endIndex = next(x for x, val in enumerate(wavs) if val > endpt2)
360.         wavs = np.delete(wavs,np.arange(startIndex, endIndex, 1))
```

```
361.         fluxs = np.delete(fluxs,np.arange(startIndex, endIndex, 1))
362.         if type(errors) is np.ndarray:
363.             errors = np.delete(errors,np.arange(startIndex, endIndex, 1))
364.     if type(errors) is np.ndarray:
365.         return (wavs,fluxs,errors)
366.     else:
367.         return(wavs,fluxs)
368. 
369. if __name__ == '__main__':
370.     myList='objects.txt'
371.     myParams='params.txt'
372. 
373.     #parse the params file
374.     parse_params(myParams)
375.     print("Params have been read in and recorded as follows:")
376.     print (f'\nThe units of the input data are {wavelengthUnits},{fluxUnits}')
377.     print (f'Normalized = {normalized}')
378.     print (f'Saumon and Marley Binary Fit = {SMBF}')
379.     print (f'Saumon and Marley Single Fit = {SMSF}')
380.     print (f'Real Models Binary Fit = {RMBF}')
381.     print (f'Real Models Single Fit = {RMSF}')
382.     print (f'Targets have errors = {areThereErrors}')
383.     if len(gapList)!= 0:
384.         print(f'The wavelength ranges omitted from fit are {gapList}')
385.     else:
386.         print("The entire wavelength range will be used in the fit.")
387.     print("\n")
388. 
389.     #parse list of objects
390.     objectsList,HmagsList,KmagsList = parse_objects(myList)
391.     print(f'The objects to be fit are {objectsList}')
392.     print(f'The data files can be found in the folder {dataFolder}\n')
393. 
394.     #decide if/which unit conversion is needed
395.     fluxFunctionName = choose_flux_conversion_func(fluxUnits)
396.     wavelengthConversionFactor = choose_wavelength_conversion(wavelengthUnits)
397.     print('\n')
398. 
399.     #create Spectrum objects for each of the Saumon & Marley models
400.     if SMSF or SMBF:
401.         SMmodelNames = np.loadtxt(f'{SMmodelFolder}/Models.txt',dtype = str)
402.         SMmodels = [None] * len(SMmodelNames)
403.         for i in tqdm (range (len(SMmodelNames)), desc="Preparing SM models..."):
404.             model = SMmodelNames[i]
405.             (wavelengths,fluxes)=np.loadtxt(model,unpack=True,comments = '#')
406.             (wavelengths,fluxes)=maskOverGaps(wavelengths, fluxes, gapList)
407.             SMmodels[i] = savvySpectrum.SavvySpectrum(model,wavelengths,fluxes)
408. 
409.     #create Spectrum objects for each of the real data models
410.     if RMSF or RMBF:
411.         RMmodelNames = np.loadtxt(f'{RMmodelFolder}/Models.txt',dtype = str)
412.         RMmodels = [None] * len(RMmodelNames)
413.         for i in tqdm (range (len(RMmodelNames)), desc="Preparing RM models..."):
414.             model = RMmodelNames[i]
415.             (wavelengths,fluxes,errors)=np.loadtxt(model,unpack=True,comments = '#')
416.             (wavelengths,fluxes,errors)=maskOverGaps(wavelengths, fluxes, gapList,errors)
417.             RMmodels[i] = savvySpectrum.SavvySpectrum(model,wavelengths,fluxes, errors)
418. 
419.     #create Spectrum objects for each target object
420.     #convert to um and Jy and/or unnormalize if needed
421.     spectrumObjects = [None] * len(objectsList)
422.     degreesOfFreedom = [None]*len(objectsList)
423.     for i in tqdm (range (len(objectsList)), desc="Preparing target objects..."):
424.         friend = objectsList[i]
425.         if os.path.isdir(objectsList[i])==False:
```

```
426.             os.mkdir(objectsList[i])
427.         if areThereErrors == False:
428.             (wavelengths,fluxes) =
np.loadtxt(f'{dataFolder}/{friend}Raw.txt',unpack=True,comments = '#')
429.             errors = None
430.         else:
431.             (wavelengths,fluxes,errors) =
np.loadtxt(f'{dataFolder}/{friend}Raw.txt',unpack=True,comments = '#')
432.         wavelengths = wavelengths * wavelengthConversionFactor
433.         if fluxFunctionName != None:
434.             fluxes,errors=eval(f'{fluxFunctionName}(wavelengths,fluxes,errors)')
435.         if normalized == True:
436.            wavelengths,fluxes,errors = unNormalize(friend, wavelengths, fluxes, errors,
HmagsList[i], KmagsList[i])
437.         if areThereErrors == False:
438.             (wavelengths,fluxes)=maskOverGaps(wavelengths, fluxes, gapList)
439.         else:
440.             (wavelengths,fluxes,errors)=maskOverGaps(wavelengths, fluxes, gapList,errors)
441.         spectrumObjects[i] = savvySpectrum.SavvySpectrum(friend,wavelengths,fluxes,errors)
442.         degreesOfFreedom[i] = len(wavelengths) - 1
443.
444. #TODO: make starting guess adaptable to flux of object
445. #theoretical models
446.     #single fit
447.     if SMSF:
448.         bestSMSFchi2s = [None]*len(spectrumObjects)
449.         bestSMSFnames = [None]*len(spectrumObjects)
450.         bestSMSFscales = [None]*len(spectrumObjects)
451.         for i in tqdm (range (len(spectrumObjects)), desc="Performing SMSF..."):
452.             target = spectrumObjects[i]
453.             currentSMmodels = regridModels(target,SMmodels)
454.             SMSFresults=fitter(target,currentSMmodels,10**-19,10**-22,gapList)
455.             SMSFnames, SMSFchi2s,SMSFscales = zip(*SMSFresults)
456.             bestSMSFchi2s[i] = SMSFchi2s[0]
457.             bestSMSFnames[i] = SMSFnames[0]
458.             bestSMSFscales[i] = SMSFscales[0]
459.             dict = {'name':SMSFnames,'chi2':SMSFchi2s,'scale':SMSFscales}
460.             df = pd.DataFrame(dict)
461.             df.to_csv(f'{objectsList[i]}/AllSMSFresults.csv')
462.             #create spectrum objects for results
463.             (SMSFwav,SMSFflux) = np.loadtxt(SMSFnames[0],unpack=True,comments = '#')
464.             SMSFflux = SMSFflux * SMSFscales[0]
465.             SMSFbest = savvySpectrum.SavvySpectrum(SMSFnames[0],SMSFwav,SMSFflux)
466.             plotSpectra([SMSFbest,target],['Best Single Fit','Target'],f'{target.path} SM
Single Best Fit',target.path,logPlot)
467.             bestSingleSMData=np.column_stack((SMSFwav,SMSFflux))
468.             np.savetxt(f'{target.path}/{target.path}BestSMSingleFit.txt',bestSingleSMData)
469.             #create detailed Excel sheet for top 100 objects
470.
printTop100FitCharacteristics(f'{objectsList[i]}/AllSMSFresults.csv',f'{objectsList[i]}/SMSFtop100.c
sv')
471.             #calculate errors in the fit (function not implemented yet)
472.             calculateErrors()
473.
474.     #binary fit
475.     if SMBF:
476.         bestSMBFchi2s = [None]*len(spectrumObjects)
477.         bestSMBFnames = [None]*len(spectrumObjects)
478.         bestSMBFscales = [None]*len(spectrumObjects)
479.         for i in tqdm (range (len(spectrumObjects)), desc="Performing SMBF..."):
480.             target = spectrumObjects[i]
481.             currentSMmodels = regridModels(target,SMmodels)
482.             SMBFresults=binaryFitter(target,currentSMmodels,10**-19,10**-22,gapList)
483.             SMBFnames, SMBFchi2s,SMBFscales = zip(*SMBFresults)
484.             bestSMBFchi2s[i] = SMBFchi2s[0]
```

```
485.             bestSMBFnames[i] = SMBFnames[0]
486.             bestSMBFscales[i] = SMBFscales[0]
487.             dict = {'name':SMBFnames,'chi2':SMBFchi2s,'scale':SMBFscales}
488.             df = pd.DataFrame(dict)
489.             df.to_csv(f'{objectsList[i]}/AllSMBFresults.csv')
490.             #split name into two objects
491.             SMBF1,SMBF2,empty = SMBFnames[0].split(".txt")
492.             SMBF1 = SMBF1 + '.txt'
493.             SMBF2 = SMBF2 + '.txt'
494.             #create spectrum objects for results
495.             (SMBFwav1,SMBFflux1) = np.loadtxt(SMBF1,unpack=True,comments = '#')
496.             (SMBFwav2,SMBFflux2) = np.loadtxt(SMBF2,unpack=True,comments = '#')
497.             SMBFflux1 = SMBFflux1 * SMBFscales[0]
498.             SMBFflux2 = SMBFflux2 * SMBFscales[0]
499.             SMBFbest1 = savvySpectrum.SavvySpectrum(SMBF1,SMBFwav1,SMBFflux1)
500.             SMBFbest2 = savvySpectrum.SavvySpectrum(SMBF2,SMBFwav2,SMBFflux2)
501.             (SMBFbest1reg,SMBFbest2reg) = regridModels(target,[SMBFbest1,SMBFbest2])
502.             SMBFcomposite = savvySpectrum.SavvySpectrum(SMBFnames[0], SMBFbest1reg.wavs,
SMBFbest1reg.fluxes + SMBFbest2reg.fluxes)
503.             plotSpectra([SMBFbest1,SMBFbest2,SMBFcomposite,target],['Binary Component
1','Binary Component 2','Composite','Target'],f'{target.path} SM Binary Best Fit
Components',target.path,logPlot)
504.             plotSpectra([SMBFcomposite,target],['Best Binary Fit','Target'],f'{target.path} SM
Binary Best Fit',target.path,logPlot)
505.             bestBinarySMData1=np.column_stack((SMBFwav1,SMBFflux1))
506.
np.savetxt(f'{target.path}/{target.path}BestSMBinaryComponent1.txt',bestBinarySMData1)
507.             bestBinarySMData2=np.column_stack((SMBFwav2,SMBFflux2))
508.
np.savetxt(f'{target.path}/{target.path}BestSMBinaryComponent2.txt',bestBinarySMData2)
509.             bestBinarySMCompositeData = np.column_stack((SMBFbest1reg.wavs,SMBFbest1reg.fluxes
+ SMBFbest2reg.fluxes))
510.
np.savetxt(f'{target.path}/{target.path}BestSMBinaryComposite.txt',bestBinarySMCompositeData)
511.             #create detailed Excel sheet for top 100 objects
512.
printTop100FitCharacteristicsForBinaries(f'{objectsList[i]}/AllSMBFresults.csv',f'{objectsList[i]}/S
MBFtop100.csv')
513.
514. #real data models
515. #TODO: regrid target in case target has higher grid than models?
516. #TODO: what to do if your gaps are outside RM model range? EX: Spitzer long
517.     #single fit
518.     if RMSF:
519.         bestRMSFchi2s = [None]*len(spectrumObjects)
520.         bestRMSFnames = [None]*len(spectrumObjects)
521.         bestRMSFscales = [None]*len(spectrumObjects)
522.         for i in tqdm (range (len(spectrumObjects)), desc="Performing RMSF..."):
523.             target = spectrumObjects[i]
527.             currentRMmodels = regridModelsWithErrors(target,RMmodels)
528.             RMSFresults = fitter(target,currentRMmodels,1,10**-10,gapList)
529.             RMSFnames,RMSFchi2s,RMSFscales = zip(*RMSFresults)
530.             bestRMSFchi2s[i] = RMSFchi2s[0]
531.             bestRMSFnames[i] = RMSFnames[0]
532.             bestRMSFscales[i] = RMSFscales[0]
533.             dict = {'name':RMSFnames,'chi2':RMSFchi2s,'scale':RMSFscales}
534.             df = pd.DataFrame(dict)
535.             df.to_csv(f'{objectsList[i]}/RMSFresults.csv')
536.             #create spectrum objects for results
537.             (RMSFwav,RMSFflux,RMSFerrors) = np.loadtxt(RMSFnames[0],unpack=True,comments = '#')
538.             RMSFflux = RMSFflux * RMSFscales[0]
539.             RMSFbest = savvySpectrum.SavvySpectrum(RMSFnames[0],RMSFwav,RMSFflux)
540.             plotSpectra([RMSFbest,target],['Best Single Fit','Target'],f'{target.path} RM
Single Best Fit',target.path)
541.             bestSingleRMData=np.column_stack((RMSFwav,RMSFflux))
```

```
542.             np.savetxt(f'{target.path}/{target.path}BestRMSingleFit.txt',bestSingleRMData)
543.
544.
545.     #binary fit
546.     if RMBF:
547.         bestRMBFchi2s = [None]*len(spectrumObjects)
548.         bestRMBFnames = [None]*len(spectrumObjects)
549.         bestRMBFscales = [None]*len(spectrumObjects)
550.         for i in tqdm (range (len(spectrumObjects)), desc="Performing RMBF..."):
551.             target = spectrumObjects[i]
552.             currentRMmodels = regridModelsWithErrors(target,RMmodels)
553.             RMBFresults = binaryFitter(target,currentRMmodels,1,10**-10,gapList)
554.             RMBFnames,RMBFchi2s,RMBFscales = zip(*RMBFresults)
555.             bestRMBFchi2s[i] = RMBFchi2s[0]
556.             bestRMBFnames[i] = RMBFnames[0]
557.             bestRMBFscales[i] = RMBFscales[0]
558.             dict = {'name':RMBFnames,'chi2':RMBFchi2s,'scale':RMBFscales}
559.             df = pd.DataFrame(dict)
560.             df.to_csv(f'{objectsList[i]}/RMBFresults.csv')
561.             #split name into two objects
562.             RMBF1,RMBF2,empty = RMBFnames[0].split(".txt")
563.             RMBF1 = RMBF1 + '.txt'
564.             RMBF2 = RMBF2 + '.txt'
565.             #create spectrum objects for results
566.             (RMBFwav1,RMBFflux1, RMBFerror1) = np.loadtxt(RMBF1,unpack=True,comments = '#')
567.             (RMBFwav2,RMBFflux2,RMBFerror2) = np.loadtxt(RMBF2,unpack=True,comments = '#')
568.             RMBFflux1 = RMBFflux1 * RMBFscales[0]
569.             RMBFflux2 = RMBFflux2 * RMBFscales[0]
570.             RMBFbest1 = savvySpectrum.SavvySpectrum(RMBF1,RMBFwav1,RMBFflux1,RMBFerror1)
571.             RMBFbest2 = savvySpectrum.SavvySpectrum(RMBF2,RMBFwav2,RMBFflux2,RMBFerror2)
572.             (RMBFbest1reg,RMBFbest2reg) = regridModels(target,[RMBFbest1,RMBFbest2])
573.             RMBFcomposite = savvySpectrum.SavvySpectrum(RMBFnames[0], RMBFbest1reg.wavs,
RMBFbest1reg.fluxes + RMBFbest2reg.fluxes)
574.             plotSpectra([RMBFbest1,RMBFbest2,RMBFcomposite,target],['Binary Component
1','Binary Component 2','Composite','Target'],f'{target.path} RM Binary Best Fit
Components',target.path)
575.             plotSpectra([RMBFcomposite,target],['Best Binary Fit','Target'],f'{target.path} RM
Binary Best Fit',target.path)
576.             bestBinaryRMData1=np.column_stack((RMBFwav1,RMBFflux1))
577.
np.savetxt(f'{target.path}/{target.path}BestRMBinaryComponent1.txt',bestBinaryRMData1)
578.             bestBinaryRMData2=np.column_stack((RMBFwav2,RMBFflux2))
579.
np.savetxt(f'{target.path}/{target.path}BestRMBinaryComponent2.txt',bestBinaryRMData2)
580.             bestBinaryRMCompositeData = np.column_stack((RMBFbest1reg.wavs,RMBFbest1reg.fluxes
+ RMBFbest2reg.fluxes))
581.
np.savetxt(f'{target.path}/{target.path}BestRMBinaryComposite.txt',bestBinaryRMCompositeData)
582.
583.     #analyze results
584.     for i in range(0,len(spectrumObjects)):
585.         if SMSF and SMBF:
586.             etaSM = calculateEta(bestSMSFchi2s[i], bestSMBFchi2s[i])
587.
fTest(etaSM,degreesOfFreedom[i],spectrumObjects[i].path,'SM',bestSMSFnames[i],bestSMSFscales[i],best
SMBFnames[i],bestSMBFscales[i])
588.         if RMSF and RMBF:
589.             etaRM = calculateEta(bestRMSFchi2s[i], bestRMBFchi2s[i])
590.
fTest(etaRM,degreesOfFreedom[i],spectrumObjects[i].path,'RM',bestRMSFnames[i],bestRMSFscales[i],best
RMBFnames[i],bestRMBFscales[i])
591.
```

regridTheSpectrum.py

```
from scipy import interpolate

#TODO: add smoothing back in?
#smoothsize=40

def regrid(wavs,fluxs,templateWavs,name,hasErrors = False,errs = None):

    tck = interpolate.splrep(wavs, fluxs)
    newFluxes = interpolate.splev(templateWavs, tck)
    if hasErrors:
        tck2 = interpolate.splrep(wavs,errs)
        newErrs = interpolate.splev(templateWavs,tck2,der=0)
    else:
        newErrs = None
    for n in range(0,len(newFluxes)):
        if newFluxes[n]<0:
            newFluxes[n]=0
    return(templateWavs,newFluxes,newErrs)


def regridModels(target,models):
    for model in models:

(model.wavs,model.fluxes,emptyError)=regrid(model.wavs,model.fluxes,target.wavs,model.path)
    return models

def regridModelsWithErrors(target,models):
    for model in models:

(model.wavs,model.fluxes,model.errors)=regrid(model.wavs,model.fluxes,target.wavs,model.path,True,mo
del.errors)
    return models

```

savvyFitter.py

```
# -*- coding: utf-8 -*-
"""
Created on Tue May 31 14:23:56 2022

@author: savan
"""

import numpy as np
import scipy.optimize as optimize
from itertools import combinations
import savvySpectrum

targetObject = None
template = None

def chai_squared(scale):
```

```
    #What to do when the error is 0?
    #TODO: If including errors, the binary fitter needs an option to generate composite models including errors
    C = targetObject.fluxes
    T = template.fluxes
    #sigma = targetObject.errors
    #chaiSquared = np.sum(((C - scale*T)/sigma)**2)
    chaiSquared = np.sum((C - scale*T)**2)
    return chaiSquared

def makeNameList(templateList):
    names = [None]*len(templateList)
    for i in range(0,len(templateList)):
        names[i] = templateList[i].path
    return names

def fitter(targetObjectin,templateList,initialGuess,tolerance,gapList):
    chaiSquaredList = [None]*len(templateList)
    totalFailed = 0
    scaleList = [None]*len(templateList)
    global targetObject
    global template
    targetObject = targetObjectin
    nameList = makeNameList(templateList)
    fitResultsList = [None]*len(templateList)
    for i in range(0,len(templateList)):
        template = templateList[i]
        results = optimize.minimize(chai_squared, tol = tolerance, x0=[initialGuess], method = "Nelder-Mead")
        if results.success == False:
            totalFailed += 1
        scaleList[i] = results.x
        chaiSquaredList[i] = results.fun
        fitResultsList[i]= (nameList[i],results.fun,results.x[0])
    fitResultsList.sort(key = lambda x: x[1])
    percent = (totalFailed / len(templateList))*100
    if percent >= 10:
        print(f'\nThe total number of failed fits for {targetObjectin.path} was {totalFailed} out of {len(templateList)}.')
    return fitResultsList

def binaryFitter(targetObjectin,templateList,initialGuess,tolerance,gapList):
    pairs = list(combinations(templateList,2))
    chaiSquaredList = [None]*len(pairs)
    totalFailed = 0
    scaleList = [None]*len(pairs)
    global targetObject
    global template
    targetObject = targetObjectin
    nameList = [None]*len(pairs)
    fitResultsList = [None]*len(pairs)
    for i in range(0,len(pairs)):
        currentPair = pairs[i]
        first = currentPair[0]
        second = currentPair[1]
        nameList[i] = f'{first.path}{second.path}'
        compositeFluxes = first.fluxes + second.fluxes
        compositeModel = savvySpectrum.SavvySpectrum(nameList[i],first.wavs,compositeFluxes)
        template = compositeModel
        results = optimize.minimize(chai_squared, tol = tolerance, x0=[initialGuess], method = "Nelder-Mead")
        if results.success == False:
            totalFailed += 1
        scaleList[i] = results.x
        chaiSquaredList[i] = results.fun
```

```
78.         fitResultsList[i]= (nameList[i],results.fun,results.x[0])
79.     fitResultsList.sort(key = lambda x: x[1])
80.     percent = (totalFailed / len(pairs))*100
81.     if percent >= 10:
82.         print(f'\nThe total number of failed fits for {targetObjectin.path} was {totalFailed}
out of {len(templateList)}.')
83.     return fitResultsList
84.
```

savvySpectrum.py

```
 1. # -*- coding: utf-8 -*-
 2. """
 3. Created on Tue May 31 14:06:07 2022
 4.
 5. @author: savan
 6. """
 7. from scipy import interpolate
 8.
 9. class SavvySpectrum:
10.     def __init__(self, path, wavs, fluxes, errors = None):
11.         self.path = path
12.         self.wavs = wavs
13.         self.fluxes = fluxes
14.         self.errors = errors
```

Appendix 2

Object Name	Optical Type	IR Type	2MASS J	2MASS H	2MASS K	Ref
SDSS J000013.54+255418.6	----	T4.5	15.063	14.731	14.836	[81]
SDSS J000250.98+245413.8	----	L5.5	17.165	16.06	15.656	[69]
LHS 102B (J00043484-4044058)	L5	L4.5	13.109	12.055	11.396	[70]
2MASS J00150206+2959323	L7	L7.5pec	16.158	15.226	14.482	[82]
2MASS J00165953-4056541	L3.5	----	15.316	14.206	13.432	[45]
2MASS J00193927-3724392	L3:	----	15.519	14.47	13.689	[45]
2MASS J0028208+224905	----	L7:	15.607	14.468	13.781	[45]
2MASSW J0030300-145033	L7	----	16.278	15.273	14.481	[45]
SDSSp J003259.36+141036.6	----	L8	16.83	15.648	14.946	[45]
2MASS J00345157+0523050	----	T6.5	15.535	15.443	16.243	[76]
2MASSW J0036159+182110	L3.5	L4+/-1	12.466	11.588	11.058	[31]
SDSS J003609.26+241343.3	----	L5.5	17.033	16.108	15.657	[69]
HD 3651B (J0039191+211516)	----	T7.5	16.16	16.68	16.87	[70]
2MASS J00501994-3322402	----	T7	15.928	15.838	15.241	[81]
2MASSW J0051107-154417	L3.5	----	15.277	14.164	13.466	[45]
2MASS J00531899-3631102	L3.5	----	14.445	13.48	12.937	[45]
2MASSI J0103320+193536	L6	----	16.288	14.897	14.149	[71]
SDSSp J010752.33+004156.1	L8	L5.5	15.824	14.512	13.709	[45]
2MASSI J0117474-340325	L2	----	15.178	14.209	13.489	[31]
SDSS J011912.22+240331.6	----	T2	17.017	15.953	17.042	[69]
2MASS J01311838+3801554	L4:	----	14.679	13.696	13.054	[45]
2MASS J01340281+0508125	----	L1	16.024	15.376	14.459	[82]
IPMS J013656.57+093347.3	----	T2.5	13.455	12.771	12.562	[31]
2MASS J01414839-1601196	----	L7:	16.209	15.161	14.344	[82]
2MASS J01415823-4633574	L0 lg	L0pec	14.832	13.875	13.097	[72]
2MASS J01443536-0716142	L5	----	14.191	13.008	12.268	[31]
2MASS J01472702+4731142	----	L1.5	15.843	14.847	14.282	[82]
SDSS J015141.69+124429.6	----	T1	16.566	15.603	15.183	[76]
2MASS J01550354+0950003	----	L5:	14.825	13.763	13.139	[45]

SDSS J020735.60+135556.3	L3	L3+/-1.5	15.462	14.474	13.808	
2MASSW J0205034+125142	L5	----	15.679	14.449	13.671	[73]
DENIS-P J0205.4-1159 (J02052940-1159296)	L7	L5.5+/-2	14.587	13.568	12.998	[45]
2MASS J02055138-0759253	----	L2	16.031	15.169	14.358	[82]
SDSS J020608.97+223559.2	----	L5.5	16.556	15.538	15.162	[69]
SDSS J020742.48+000056.2	----	T4.5	16.799	16.396	15.412	[81]
2MASSW J0208236+273740	L5	----	15.714	14.56	13.872	[45]
2MASSW J0208183+254253	L1	----	13.989	13.107	12.588	[31]
2MASS J02271036-1624479	L1	----	13.573	12.63	12.143	[31]
2MASSW J0228110+253738	L0	L0	13.839	12.993	12.471	[31]
2MASS J02304442-3027275	----	L1	15.822	15.21	14.886	[82]
GJ 1048B (J02355993-2331205)	L1	L1	12.69	12.725	12.186	[31]
2MASSI J0241536-124106	L2	----	15.605	14.646	13.931	[31]
SDSS J024256.98+212319.6	----	L4	16.977	15.938	15.474	[69]
2MASSI J0243137-245329	----	T6	15.381	15.137	15.216	[76]
SDSS J024749.90-163112.6	----	T2+/-1.5	17.186	16.17	15.616	[69]
DENIS-P J0255-4700 (J02550357-4700509)	L8	L9	13.246	12.204	11.558	[81]
2MASS J02572581-3105523	L8	----	14.672	13.518	12.876	[74]
2MASS J03001631+2130205	----	L6 pec	15.921	14.885	14.258	[82]
2MASSW J0310599+164816	L8	L9	16.025	14.932	14.312	[70]
2MASS J03185403-3421292	L7	----	15.569	14.346	13.507	[45]
2MASSW J0320284-044636	----	L0.5	13.259	12.535	12.134	[31]
SDSS J032553.17+042540.1	----	T5.5	16.25	16.08	16.525	[69]
2MASSI J0328426+230205	L8	L9.5	16.693	15.547	14.916	[31]
2MASP J0345432+254023	L0	L1+/-1	13.997	13.211	12.672	[75]
SDSS J035104.37+481046.8	----	T1+/-1.5	16.466	15.566	14.996	[69]
2MASS J04070752+1546457	----	L3.5	15.478	14.354	13.559	[31]
2MASS J04070885+1514565	----	T5	16.055	16.017	15.922	[76]
2MASS J04062677-3812102	L0gamma	L1pec	16.756	15.624	15.111	[82]
2MASSI J0415195-093506	T8	T8	15.695	15.537	15.429	[76]
SDSSp J042348.57-041403.5	L7.5	T0	14.465	13.463	12.929	[76]
2MASSI J0439010-235308	L6.5	----	14.408	13.409	12.816	[70]
2MASS J0447430-193604	L5:	----	15.969	14.785	14.012	[45]
2MASS J05103520-4208140	----	T5	16.222	16.237	15.996	[78]
2MASS J05160945-0445499	----	T5.5	15.984	15.721	15.486	[31]
2MASS J05161597-3332046	L3:	----	15.879	14.801	13.987	[45]
2MASS J05185995-2828372	L7.5pec	T1p	15.978	14.83	14.162	[71]
SDSSp J053951.99-005902.0	L5	L5	14.033	13.104	12.527	[89]

2MASS J05591914-1404488	T5	T4.5	13.802	13.679	13.577	[81]
2MASS J06020638+4043588	----	T4.5	15.544	15.592	15.166	[78]
2MASS J06244595-4521548	L5:	----	14.48	13.335	12.595	[74]
2MASSI J0652307+471034	L4.5	----	13.511	12.384	11.694	[45]
SDSS J065405.63+652805.4	----	L6+/-1	16.138	15.196	14.603	[45]
2MASSW J0717163+570543	----	L6.5	14.636	13.593	12.945	[45]
2MASSI J0727182+171001	T8	T7	15.6	15.756	15.556	[81]
2MASS J07290002-3954043	----	T8pec	15.92	15.979	15.29	[78]
SDSS J073922.26+661503.5	----	T1.5+/-1	16.823	15.998	15.831	[45]
SDSS J074149.15+235127.5	----	T5	16.158	15.838	15.847	[45]
2MASS J07415784+0531568	----	L1.5	14.379	13.563	13.062	[82]
SDSS J074201.41+205520.5	----	T5	16.193	15.911	15.225	[45]
2MASSI J0755480+221218	T6	T5	15.728	15.669	15.753	[81]
SDSS J075840.33+324723.4	----	T2	14.947	14.111	13.879	[31]
2MASSW J0801405+462850	L6.5	----	16.275	15.452	14.536	[45]
SDSS J080531.84+481233.0	L4	L9+/-1.5	14.734	13.917	13.444	[70]
2MASSW J0820299+450031	L5	----	16.279	15	14.218	[45]
SDSS J082030.12+103737.0	----	L9.5+/-2	16.98	16.079	15.538	[69]
2MASS J08234818+2428577	L3	----	14.986	14.06	13.377	[45]
2MASSI J0825196+211552	L7.5	L6	15.1	13.792	13.028	[45]
SSSPM 0829-1309	L2	----	12.803	11.851	11.297	[70]
SDSSp J083008.12+482847.4	L8	L9+/-1	15.444	14.343	13.676	[31]
SDSS J083048.80+012831.1	----	T4.5	16.289	16.14	16.358	[45]
SDSS J083506.16+195304.4	----	L4.5	16.094	14.889	14.319	[69]
2MASSI J0835425-081923	L5	----	13.169	11.938	11.136	[45]
SDSSp J083717.22-000018.3	T0+/-2	T1	17.101	15.988	15.674	[81]
2MASSI J0847287-153237	L2	----	13.513	12.629	12.061	[77]
2MASSs J0850359+105716	L6	----	16.465	15.221	14.473	[83]
SDSS J085116.20+181730.0	----	L4.5+/-1.5	16.567	15.948	14.968	[69]
SDSS J085234.90+472035.0	----	L9.5+/-1	16.182	15.419	14.718	[45]
2MASSI J0856479+223518	L3:	----	15.679	14.58	13.951	[45]
SDSSp J085758.45+570851.4	L8	L8+/-1	15.038	13.79	12.962	[45]
SDSS J085834.42+325627.7	----	T1	16.453	15.382	14.756	[45]
2MASS J09054654+5623117	----	L5	15.395	14.284	13.73	[45]
2MASSI J0908380+503208	L5	L9+/-1	14.549	13.477	12.945	[74]
SDSS J090900.73+652527.2	----	T1.5	16.034	15.214	15.171	[69]
Gl 337CD (J09121469+1459396	L8	T0	15.512	14.621	14.043	[45]
2MASS J09153413+0422045	L7	----	14.548	13.531	13.011	[70]
2MASSW J0920122+351742	L6.5	T0p	15.625	14.673	13.979	[45]

2MASS J09211410-2104446	L2	pec	12.779	12.152	11.69	[70]
SDSSp J092615.38+584720.9	----	T4.5	15.897	15.307	15.45	[45]
2MASSW J0929336+342952	L8	L7.5	16.601	15.44	14.644	[45]
2MASSI J0937347+293142	T7	T6p	14.648	14.703	15.267	[81]
2MASS J09393548-2448279		T8	15.98	15.797	16.556	[81]
2MASS J09490860-1545485	----	T2	16.149	15.262	15.227	[81]
SDSS J100711.74+193056.2	----	L8+/-1.5	16.871	15.755	14.997	[45]
2MASS J10073369-4555147	----	T5	15.653	15.686	15.56	[78]
2MASSI J1010148-040649	L6	----	15.508	14.385	13.619	[73]
SDSS J102109.69-030420.1	T4+/-2	T3	16.253	15.346	15.126	[81]
HD 89744B (J10221489+4114266)	L0	L (early)	14.901	14.022	13.608	[31]
SDSS J102552.43+321234.0	----	L7.5+/-2.5	15.913	15.593	15.072	[69]
SDSS J103026.78+021306.4	----	L9.5+/-1	16.889	16.175	15.079	[45]
2MASS J10315064+3349595	----	L2	15.923	14.838	14.364	[82]
SDSS J103321.92+400549.5	----	L6	16.644	15.874	15.408	[69]
2MASSW J1036530-344138	L6	----	15.622	14.446	13.798	[45]
SDSS J103931.35+325625.5	----	T1	16.405	15.335	15.151	[45]
2MASS J10430758+2225236	L8	----	15.965	14.725	13.991	[74]
SDSS J104335.08+121314.1	----	L7+/-1	15.997	14.969	14.258	[45]
SDSS J104335.08+121314.1	----	L9	15.997	14.969	14.258	[82]
SDSS J104409.43+042937.6	----	L7	15.881	14.95	14.259	[45]
2MASSI J1047538+212423	T7	T6.5	15.819	15.797	16.408	[31]
SDSS J104842.84+011158.5	L1	L4	12.924	12.14	11.623	[31]
2MASS J10461875+4441149	----	L5 pec	15.622	14.656	14.13	[82]
SDSS J104829.21+091937.8	----	T2.5	16.594	15.898	16.365	[45]
SDSS J105213.51+442255.7	----	T0.5+/-1	15.958	15.161	14.568	[31]
DENIS-P J1058.7-1548 (J10584787-1548172)	L3	L3	14.155	13.226	12.532	[45]
2MASS J10595219+3041498	----	T4	16.195	15.766	15.56	[79]
2MASS J10595185+3042059	----	T4	16.195	15.766	15.56	[79]
2MASS J11000965+4957470	----	L3.5	15.282	14.192	13.474	[74]
2MASSI J1104012+195921	L4	----	14.38	13.476	12.95	[76]
SDSSp J111010.01+011613.1	----	T5.5	16.343	15.924	15.129	[81]
Gliese 417BC (J11122567+3548131)	----	L4.5	14.584	13.499	12.721	[45]
SDSS J111320.16+343057.9	----	L3	16.767	15.803	15.51	[69]
2MASS J11145133-2618235	----	T7.5	15.858	15.734	16.109	[81]
2MASS J11181292-0856106	L6	L6 pec	15.784	14.731	14.296	[82]
SDSS J112118.57+433246.5	----	L7.5	17.006	16.231	15.572	[69]
2MASS J11220826-3512363	----	T2	15.019	14.358	14.383	[81]

2MASS J11263991-5003550	L4.5	T0+/-1.5 (pec)	13.997	13.284	12.829	[31]
2MASSW J1146345+223053	L3	----	14.165	13.182	12.59	[45]
SDSS J115553.86+055957.5	----	L7.5	15.66	14.703	14.118	[45]
2MASS J11582077+0435014	sdL7	sdL7	15.611	14.684	14.439	[82]
2MASS J12070374-3151298	----	L3:	15.85	14.719	13.997	[74]
SDSS J120602.51+281328.7	----	T3	16.541	15.815	15.817	[69]
SDSS J120747.17+024424.8	L8	T0	15.58	14.561	13.986	[78]
2MASS J12095613-1004008	----	T3	15.914	15.329	15.062	[76]
2MASS J12154432-3420591	----	T4.5	16.236	15.809	16.317	[78]
SDSS J121440.95+631643.4	----	T3.5+/-1	16.586	15.779	15.877	[69]
SDSS J121659.17+300306.3	----	L3.5+/-1	17.072	15.739	15.813	[69]
2MASSI J1217110-031113	T7	T7.5	15.86	15.748	15.887	[81]
SDSS J121951.45+312849.4	----	L8	15.913	14.907	14.305	[45]
2MASS J12212770+0257198	L0	----	13.169	12.41	11.953	[31]
2MASS J12255432-2739466	T6	T6	15.26	15.098	15.073	[76]
DENIS-P J1228.2-1547 (J12281523-1547342)	L5	L6+/-2	14.378	13.347	12.767	[45]
2MASS J12304562+2827583	----	L4:	16.073	15.005	14.434	[79]
2MASS J12314753+0847331	----	T5.5	15.57	15.309	15.22	[76]
2MASS J12373919+6526148	T7	T6.5	16.053	15.739	16.058	[88]
2MASSW J1239272+551537	L5	----	14.711	13.568	12.792	[45]
2MASS J12474944-1117551	----	L0:	15.991	15.104	14.725	[82]
SDSSp J125453.90-012247.4	T2	T2	14.891	14.09	13.837	[76]
2MASS J13023811+5650212	L2	L3pec	16.36	15.469	14.972	[82]
Kelu-1 (J13054019-2541059)	L2	L3+/-1	13.414	12.392	11.747	[70]
2MASS J13184794+1736117	----	L5.5	16.341	15.227	14.533	[82]
2MASS J13243553+6358281	----	T2:pec	15.596	14.576	14.058	[78]
SDSSp J132629.82-003831.5	L8:	L5.5	16.103	15.05	14.208	[45]
2MASS J13313310+3407583	L0	L1pec	14.168	13.333	12.868	[82]
SDSS J133148.92-011651.4	L6	L8+/-2.5	15.459	14.475	14.073	[45]
SDSS J134203.11+134022.2	----	L5.5	16.756	15.708	15.109	[69]
SDSS J134525.57+521634.0	----	L3.5	16.945	16.257	15.348	[69]
SDSSp J134646.45-003150.4	T7	T6.5	16	15.459	15.772	[81]
2MASS J13571237+1428398	L4:	----	15.584	14.647	13.88	[45]
SDSS J135852.68+374711.9	----	T4.5+/-1	16.46	16.142	16.099	[69]
SDSS J140023.12+433822.3	----	L7+/-1	16.301	15.094	14.487	[45]
2MASS J14044941-3159329	----	T2.5	15.577	14.955	14.538	[78]
2MASS J14075361+1241099	L5	----	15.378	14.344	13.598	[45]
2MASS J14162409+1348267	L6	----	13.148	12.456	12.114	[86]

SDSS J141530.05+572428.7	----	T3+/-1	16.734	15.821	15.544	[45]
SDSS J141659.78+500626.4	----	L5.5+/-2	16.95	15.955	15.597	[69]
2MASS J14182962-3538060	----	L1.5	15.165	14.253	13.691	[82]
2MASS J14192618+5919047	----	L1:	16.411	15.757	15.024	[82]
SDSS J142227.25+221557.1	----	L6.5+/-2	17.064	16.032	15.642	[69]
2MASS J14283132+5923354	----	L4	14.781	13.875	13.265	[45]
2MASS J14313029+1436599	----	L2 (pec)	15.151	14.501	14.125	[79]
2MASS J14313097+1436539	L2	L3.5+/-1.5	15.151	14.501	14.125	[79]
2MASS J14343616+2202463	----	L2.5+/-1.5	14.519	13.833	13.545	[79]
SDSS J143553.25+112948.6	----	T2+/-1	17.137	16.15	16.906	[69]
SDSS J143945.86+304220.6	----	T2.5	17.223	16.28	15.881	[69]
2MASS J14403186-1303263	L1	L1pec	15.38	14.747	14.243	[82]
2MASSW J1439284+192915	L1	----	12.759	12.041	11.546	[76]
2MASSW J1448256+103159	----	L3.5	14.556	13.433	12.683	[45]
Gliese 570D (J14571496-2121477)	T7	T7.5	15.324	15.268	15.242	[76]
2MASS J15031961+2525196	T6	T5	13.937	13.856	13.963	[76]
2MASSW J1506544+132106	L3	----	13.365	12.38	11.741	[70]
2MASSW J1507476-162738	L5	L5.5	12.83	11.895	11.312	[70]
SDSS J151114.66+060742.9	----	T0+/-2	16.016	14.955	14.544	[45]
2MASSW J1515008+484742	L6	L6	14.111	13.099	12.5	[45]
SDSS J151506.11+443648.3	----	L7.5+/-1.5	16.583	15.636	14.757	[45]
SDSS J151643.01+305344.4	----	T0.5+/-1	16.848	15.868	15.081	[45]
SDSS J151603.03+025928.9	----	T0	17.23	15.997	15.433	[45]
2MASS J15200224-4422419A	----	L1.5	13.55	12.73	12.27	[70]
SDSS J152039.82+354619.8	----	T0+/-1	15.54	14.579	14	[45]
SDSS J152103.24+013142.7	----	T2	16.399	15.576	15.347	[45]
2MASS J15200224-4422419B	----	L4.5	14.7	13.7	13.22	[70]
Gl 584C (J15232263+3014562)	L8	L8	16.056	14.928	14.348	[45]
2MASSI J1526140+204341	L7	----	15.586	14.497	13.922	[76]
2MASS J15293306+6730215	----	L0:	16.159	15.385	14.753	[82]
SDSS J153417.05+161546.1AB	----	T3.5	16.753	16.078	16.411	[69]
2MASSI J1534498-295227	T6	T5.5	14.9	14.866	14.843	[45]

SDSS J153453.33+121949.2	----	L4+/-1.5	15.332	14.303	13.827	[69]
SDSS J154009.36+374230.3	----	L9+/-1.5	16.558	15.348	14.739	[45]
2MASS J15461461+4932114	----	T2.5+/-1	15.902	15.135	14.9	[45]
2MASS J15462718-3325111	----	T5.5	15.631	15.446	15.485	[31]
2MASSI J1546291-332511	----	T5.5	15.631	15.446	15.485	[31]
SDSS J154849.02+172235.4	----	L5	16.104	15.142	14.456	[69]
2MASS J15500845+1455180A	L2:	----	14.776	13.795	13.261	[85]
2MASSI J1553022+153236	----	T7	15.825	15.939	15.507	[45]
2MASS J16150413+1340079	----	T6	16.35	16.489	15.859	[78]
SDSS J161731.65+401859.7	----	L4	16.741	15.605	14.754	[69]
SDSS J162255.27+115924.1	----	L6+/-1.5	16.879	16.149	15.548	[69]
SDSSp J162414.37+002915.6	----	T6	15.494	15.524	15.518	[76]
SDSS J163030.53+434404.0	----	L7+/-1.5	16.634	15.438	14.652	[45]
2MASSW J1632291+190441	L8	L8	15.867	14.612	14.003	[70]
SDSS J163239.34+415004.3	----	T1	17.078	16.114	15.748	[45]
SDSS J163359.23-064056.5	----	L6	16.138	15.165	14.544	[69]
2MASS J16382073+1327354	----	L2	16.452	15.447	14.961	[82]
2MASS J16452207+3004071	L3	----	15.19	14.213	13.587	[45]
2MASSW J1645221-131951	L1.5	----	12.451	11.685	11.145	[31]
SDSS J164916.89+464340.0	----	L5	18.265	16.311	16.177	[69]
SDSS J165329.69+623136.5	L3	----	15.089	14.442	14.069	[45]
DENIS-P J170548.38-051645.7 (J17054834-0516462)	----	L4	13.309	12.552	12.032	[45]
2MASS J17072343-0558249B	----	L3	13.96	12.72	12.2	[77]
2MASS J17111353+2326333	L0:	----	14.499	13.668	13.056	[69]
2MASSI J1711457+223204	L6.5	pec	17.089	15.797	14.727	[45]
2MASSW J1728114+394859	L7	----	15.988	14.756	13.909	[83]
SDSS J173101.41+531047.9	----	L6+/-1.5	16.374	15.484	14.854	[69]
2MASS J17320014+2656228	----	L1	15.931	15.018	14.461	[82]
2MASS J17392515+2454421	----	L4	15.802	14.647	13.946	[82]
2MASS J17461199+5034036	----	L5	15.096	14.047	13.529	[45]
2MASS J17502484-0016151	----	L5.5	13.294	12.411	11.849	[45]
SDSSp J175032.96+175903.9	----	T3.5	16.34	15.952	15.478	[76]
2MASS J1754544+164920	----	T5	15.762	15.531	14.788	[31]
2MASS J17561080+2815238	sdL1	L1pec	14.712	14.135	13.813	[82]
SDSS J175805.46+463311.9	----	T6.5	16.152	16.254	15.465	[81]

2MASSI J1807159+501531	L1.5	L1	12.934	12.127	11.602	[31]
2MASS J18131803+5101246	----	L5	15.884	14.835	14.393	[82]
2MASS J18212815+1414010	----	L5 pec	13.431	12.396	11.65	[78]
2MASS J18283572-4849046	----	T5.5	15.175	14.908	15.181	[76]
2MASS J19010601+4718136	----	T5	15.856	15.468	15.641	[76]
2MASS J19163888-3700026	----	L1	15.669	14.878	14.381	[82]
2MASS J19285196-4356256	L5	----	15.199	14.127	13.457	[45]
2MASS J19415458+6826021	----	L2	15.99	15.2	14.711	[82]
2MASS J19495702+6222440	L2 pec	L2 pec	16.359	15.47	14.75	[82]
2MASS J20025073-0521524	L6	----	15.316	14.278	13.417	[31]
2MASS J20261584-2943124	L1:	----	14.802	13.946	13.36	[84]
SDSS J202820.32+005226.5	L3	----	14.298	13.377	12.793	[76]
2MASS J20343769+0827009	L3	----	14.464	13.593	13.08	[45]
2MASS J20360316+1051295	L3	----	13.95	13.018	12.447	[45]
SDSS J204317.69-155103.4	----	L9	16.625	16.054	15.402	[45]
SDSS J204749.61-071818.3	----	T0	16.946	15.909	14.99	[45]
SDSS J205235.31-160929.8	----	T1+/-1	16.334	15.414	15.123	[45]
2MASSI J2057540-025230	L1.5	L1.5	13.121	12.268	11.724	[31]
2MASSW J2101154+175658	L7.5	----	16.853	15.861	14.892	[45]
2MASSI J2104149-103736	L3	----	13.841	12.975	12.369	[45]
2MASSI J2107316-030733	L0	----	14.2	13.443	12.878	[76]
SDSS J212413.89+010000.3	----	T5	16.031	16.183	16.144	[69]
2MASS J21321145+1341584	L6	----	15.795	14.604	13.839	[74]
2MASSW J2130446-084520	L1.5	L1	14.137	13.334	12.815	[82]
SDSS J213154.43-011939.3	----	L9	17.396	15.781	15.559	[69]
SDSS J213240.36+102949.4	----	L4.5+/-1	16.594	15.366	14.634	[69]
SDSS J213352.72+101841.0	----	L5+/-1	16.878	15.833	15.236	[69]
2MASS J21392676+0220226	----	T1.5	15.264	14.165	13.582	[81]
2MASS J21420580-3101162	L3	----	15.844	14.767	13.965	[45]
HN Peg B (J21442847+1446077)	----	T2.5	15.86	15.4	15.12	[87]
2MASS J21481628+4003593	L6	L6 pec	14.147	12.783	11.765	[80]
2MASS J21512543-2441000	L3	----	15.752	14.571	13.649	[31]
2MASS J21513979+3402444	----	L7 pec	16.704	15.796	14.983	[82]
2MASS J21513839-4853542	----	T4	15.73	15.168	15.431	[81]
2MASS J21542494-1023022	----	T4.5	16.425	16.454	17.045	[78]
2MASS J21543318+5942187	----	T5	15.661	15.765	15.338	[78]
2MASS J21555848+2345307	----	L2	15.833	15.05	14.268	[82]
2MASS J21580457-1550098	L4:	----	15.04	13.867	13.185	[45]
DENIS-P J220002.05-303832.9B (J22000201-3038327)	----	L0	14.36	13.57	13.09	[75]
2MASS J22114470+6856262	----	L2	15.668	14.761	14.023	[82]
2MASS J22120703+3430351	L5:	L6	16.316	15.182	14.37	[45]

2MASSW J2224438-015852	L4.5	L3.4	14.073	12.818	12.022	[45]
2MASS J22282889-4310262	----	T6	15.662	15.363	15.296	[76]
2MASS J22425317+2542573	L3	L	14.812	13.744	13.048	[45]
2MASSW J2244316+204343	L6.5	L7.5+/-2 (pec)	16.476	14.999	14.022	[80]
SDSSp J224953.45+004404.2	L3	L5+/-1.5 (pec)	16.587	15.421	14.358	[31]
DENIS-P J225210.73-173013.4 (J22521073-1730134)	----	L7.5	14.313	13.36	12.901	[73]
2MASSI J2254188+312349	----	T4	15.262	15.018	14.902	[76]
2MASS J23174712-4838501	L4 pec	L6.5 pec	15.15	13.925	13.181	[82]
2MASS J23254530+4251488	L8	----	15.493	14.452	13.764	[45]
2MASS J2325560-025950	L3:	----	15.961	14.935	14.115	[45]
SDSS J232804.58-103845.7	----	L3.5	17.005	15.841	15.083	[69]
2MASS J23312378-4718274	----	T5	15.659	15.51	15.389	[76]
2MASS J23392527+3507165	----	L3.5	15.362	14.351	13.588	[45]
2MASSI J2339101+135230	----	T5	16.239	15.822	16.147	[81]
2MASS J23512200+3010540	L5.5	L5 pec	15.781	14.838	14.017	[82]
2MASSI J2356547-155310	----	T5.5	15.824	15.63	15.771	[81]

Table 1: Archival data obtained from the SpeX Prism Library and BDNYC database. The name of the object, optical and infrared spectral types, 2MASS J, H, and K magnitudes, and reference are given for each of the 306 brown dwarfs. The spectral types and magnitudes provided are those listed in the headers of each archival data file. See Chapter 6 for a more detailed description of the data.

Appendix 3

Object Name	Obs Date	Spectral Type	2MASS J	2MASS H	2MASS K
WISE J203042.79+074934.7	9/16/2021	T1.5	14.227	13.435	13.319
WISE J165842.56+510335.0	10/10/2021	L6 pec	15.062	14.175	13.655
WISE J185101.83+593508.6	10/10/2021	L9 pec	14.939	13.966	13.459
SIMP J013656.57+093347.3	10/10/2021	T2	13.455	12.771	12.562
SDSSp J053951.99-005902.0	10/22/2021	L5/L5	14.033	13.104	12.527
SDSS J075840.33+324723.4	10/22/2021	T2.5	14.947	14.111	13.879
WISE J092055.40+453856.3	10/22/2021	L9	15.223	14.164	13.728
2MASSI J0908380+503208	5/11/2022	L5/L6	14.549	13.477	12.945
2MASS J11061197+2754225	5/11/2022	T2.5	14.824	14.15	13.801
SDSS J080531.84+481233.0AB	5/11/2022	L4/L9	14.734	13.917	13.444
WISE J003110.04+574936.3	6/14/2022	L8	14.954	13.779	13.215
DENIS-P J153941.96-052042.4	6/14/2022	L4/L4.2	13.922	13.06	12.575
2MASS J17114559+4028578	6/14/2022	L5	15.004	14.304	13.799
2MASSW J1515008+484742	8/24/2022	L6/L5.5	14.111	13.099	12.5
WISE J180952.53-044812.5AB	8/24/2022	T0.5	15.136	14.276	13.959
2MASS J21265916+7617440	8/24/2022	L7/T0 pec	14.336	13.586	13.16

Table 2: A list of the new spectral observations performed with the TRIPLESPEC [60] instrument on the 3.5-meter APO telescope. The second column gives the date of each observation. When two spectral types are given, the first is an optical type and the second is an infrared type. When only one type is given, it is an infrared type. Spectral types and 2MASS magnitudes were obtained from the brown dwarf database previously maintained by Chris Gellino [55]. These spectra were reduced by Conner Scoresby using methods described in [61].